Track Reconstruction In The Forward Muon Subdetector And Investigations Concerning The Photon Remnant In The H1 Detector At HERA.

by

Hywel Thorburn Phillips

A thesis submitted to the
Faculty of Science of the
University of Birmingham
for the degree of
Doctor of Philosophy

School of Physics and Space Research
University of Birmingham
B15 2TT
United Kingdom

10th December 1993

Synopsis

A brief overview of some of the physics possibilities at HERA is presented followed by an overview of the H1 detector. The forward muon spectrometer is described in detail. Simulated events are used to test the performance of the forward muon reconstruction code with and without the new phi chambers. The code is found to perform well except for a systematic shift in the value of the reconstructed momentum for low momentum tracks.

Photoproduction candidates from the 1992 data taking run are examined in the region $Q^2<0.01$, $0.2<y<0.7$ using tagged electrons as a trigger signal. 4345 candidates remain after cuts, in line with predictions from the PYTHIA 5.6 Monte Carlo using the GRV and LACIII photon structure function parameterisations. 467 events with two or more jets are found using the LUCELL cone algorithm and the distributions of jets and charged tracks in the two-jet sample examined. Good agreement is found except in the forward region, $\eta>1.0$, where more jets and tracks were observed than predicted.

The presence of a photon remnant in principle provides a clear discrimination between direct and resolved photoproduction events. Two algorithms for finding this remnant are considered and compared. Photon remnants are found in a substantial fraction of events with both algorithms, confirming that the events observed are mostly resolved. The properties of the remnant are examined and found to be in good agreement with Monte Carlo.

Acknowledgements

First and foremost, I would like to thank Heather, my wife, for her patience and forceful encouragement during the last few years. I would like to thank Professor John Dowell and the rest of the group for welcoming me into the Particle Physics group at Birmingham. I must also thank the U.K. taxpayers who, via the Science and Engineering Research Council, have funded my three years of research.

I would also like to thank Nick Ellis and Ian Kenyon, the original co-authors of the MTREC code, for their help in the initial stages of my Ph.D.. I also owe a debt of thanks to Ian Fensome, Tan Ahmed, Lawrie Lowe and Pete Faulkner for their aid in the two year battle trying to install H1 software on anything that wasn't the DESY IBM, plus numerous other hints and tips. I'd also like to thank the forward muon guys, both Manchester and Birmingham, for their help and advice through the years. In particular, Phill Biddulph and Chris Hilton never failed to know what was what with the detector and made the job of writing MTREC a lot easier. Many thanks also to Lee West, firstly for taking over the code just in time for me to do some real physics analysis and secondly for invaluable assistance whilst writing up.

In the course of my analysis, I encountered many people in the photoproduction working group at DESY. I am grateful to everyone who made suggestions on how I could improve the analysis, but Martin Erdmann and Gerhard Knies in particular never failed to have a useful idea or ten. Stuart Robertson was also very helpful when I was getting to grips with H1PHAN. (I initially stole his jet code until I found that it probably had a bug or two in it at which point I offloaded it on him again. Cheers, Stuart.)

The last three years have been fun and several people have helped to keep it so. I'd like to thank the inhabitants of 572 Pershore Road, Pershore Road in Exile and Exile's alley for multitudinous good times and many other things. I also owe thanks to the cats, Freyja, Silent Paws and Widget for being cute and providing distraction.

Last, I would like to thank my supervisor, Ian Kenyon.

Contents

Table Of Figures

Chapter 1: Introduction

The Standard Model

In the past thirty years, a theory of particle interactions called the Standard Model has emerged which describes electro-magnetic, strong and weak nuclear interactions. This model is composed of a unified description of electro-magnetic and weak nuclear interactions called Electro-weak theory (which subsumes Quantum Electrodynamics, QED) and Quantum Chromodynamics (QCD), a theory describing the strong nuclear interaction.

Note: In this work, the units used will generally be natural units, that is, $c = \hbar = 1$. Electric charges will be quoted in units of e, the magnitude of the electron's charge.

In the Standard Model, all matter is made of fundamental spin-1/2 fermions and all forces are mediated by the exchange of gauge bosons with spin-1. The fermions are divided into two types: quarks, which carry colour charge and therefore can interact via the strong force, and leptons, which do not carry colour charge. The fundamental fermions are tabulated in figure 1.1. Each fermion also has an anti-particle, denoted by placing a bar over the particle symbol. Thus, anti-up is denoted by $\bar{u}$. Although listed in the table, the existence of top quark has yet to be experimentally confirmed.

In the Standard model, matter is composed of leptons and colourless combinations of quarks called hadrons, either mesons (quark/anti-quark combinations) or baryons (three quark combinations). Three anti-quarks may form an anti-baryon. This is the quark model of hadron structure. Free quarks are not observable in this model because of the phenomenon called confinement. If an attempt is made to separate a quark from a hadron, the colour forces do not drop off with distance; instead they tend to a constant. This means that the energy in that colour field increases with the distance, so that eventually there is enough energy to liberate a quark/anti-quark pair from the vacuum. This quark/anti-quark pair now aligns with the colour field to create two combinations with the existing quarks, so there are now two hadrons instead of a free

quark and some coloured hadron remains.

It is thought that the total number of baryons in a given interaction is conserved, giving rise to the concept of baryon number (a baryon having baryon number 1 and an anti-baryon -1). It is also thought that the total number of leptons is conserved, giving rise to the lepton quantum number. It is thought that electron, muon and tau lepton numbers are separately conserved.

The gauge bosons that carry the forces are listed in figure 1.2. The photon mediates electro-magnetic interactions, the W and Z bosons mediate weak interactions and the gluons mediate strong interactions. There are eight different varieties of gluon, each carrying a different combination of the three colour and three anti-colour charges.

Quarks:

Name	Symbol	Electric Charge	Baryon Number	Lepton Number
Up quark	u	+2/3	1/3	0
Down quark	d	-1/3	1/3	0
Charm quark	c	+2/3	1/3	0
Strange quark	s	-1/3	1/3	0
Top quark (?)	t	+2/3	1/3	0
Bottom quark	b	-1/3	1/3	0

Leptons:

Name	Symbol	Electric Charge	Baryon Number	Lepton Number
Electron	e	-1	0	1
e neutrino	ν_e	0	0	1
Muon	μ	-1	0	1
μ neutrino	ν_μ	0	0	1
Tau	τ	-1	0	1
τ neutrino	ν_τ	0	0	1

Figure 1.1: The fundamental fermions. There is a question mark by the top quark as its existence has not yet been experimentally confirmed. Anti-particles have opposite signed electric charge, baryon number and lepton number.

Name	Symbol	Electric Charge	Baryon Number	Lepton Number
Photon	γ	0	0	0
W boson	W	+/- 1	0	0
Z boson	Z	0	0	0
Gluon	g_j (j=1-8)	0	0	0

Figure 1.2: The gauge bosons. There are eight gluons, each carrying a different combination of colour charges.

In the standard model, the fundamental fermions are grouped into three generations, as shown in figure 1.3. It is not clear why there should be three generations as the normal matter of the universe (protons, neutrons and electrons) only requires the first. The properties of particles in the same position within a generation are similar except for the mass (which increases with increasing generation) and the lepton number or quark flavour. Thus, the muon and tau resemble heavy electrons. All three neutrinos are believed to be massless, but carry distinct electron, muon and tau lepton numbers.

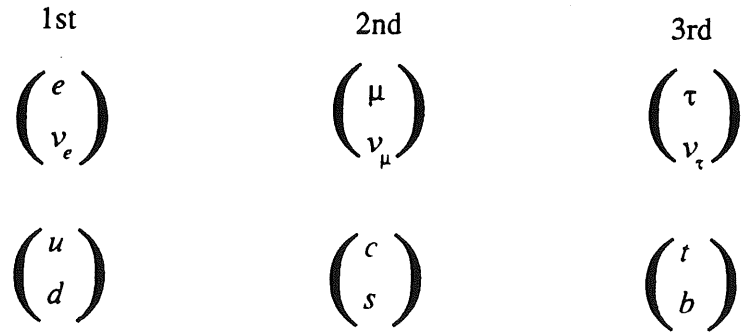

Figure 1.3: The three generations of fundamental fermions.

Open Questions In The Standard Model

The Standard Model, while comprehensive, is not yet complete. The top quark has not yet been experimentally confirmed. Searches at Fermilab have placed a lower limit on the mass of the top quark of 91 GeV at the 95% confidence level [1]. In addition, the mechanism by which the fermions acquire mass is not yet known. The favoured explanation is the Higgs mechanism [2] and the next generation of accelerators will search for the predicted Higgs bosons. It is not clear whether there is some unification of the strong and electro-weak forces at some high energy scale: this is the province of Grand Unified Theories. Finally, gravity is not included at all in the framework of the Standard Model: this is the realm of Theories of Everything. Grand Unified Theories and Theories of everything are outside the scope of this work and will not be discussed further.

More prosaic is a simple technical difficulty in calculating QCD. In QED, a perturbative expansion in the electro-magnetic coupling constant, α_{em}, is performed, with the first order diagrams containing a single factor of α_{em}, the second order diagrams containing two factors, etc. As α_{em} is small ($\approx 1/137$ at low four-momentum transfers), each succeeding order is of less significance and thus only the simpler diagrams containing a relatively small number of vertices need be considered. As the energy of the interaction increases, α_{em} also increases (e.g. to $\approx 1/128$ at LEP energies), meaning that higher order diagrams become more significant at higher energies.

In QCD, however, the strong coupling constant α_s is of order unity at low four-momentum transfers. This means that the perturbation theory approach cannot be used successfully as all possible orders of diagrams must be calculated. As the energy scale of the interaction increases, α_s decreases, meaning that perturbation theory becomes applicable. This leads to a distinction between the perturbative (or hard) region and the non-perturbative (or soft) region. In the high energy limit, α_s becomes small and the quarks appear to be unbound. This effect is known as asymptotic freedom.

The impossibility of applying perturbation theory at low energy means that the structure of hadrons, at an energy scale equal to their mass, cannot be predicted by QCD. Thus, the

formation of hadrons from asymptotically free quarks cannot be calculated in QCD and so the behaviour of hadrons at other energy scales is uncertain.

There are two approaches to this fundamental problem. One is to use lattice QCD calculations performed on computer to calculate the formation of hadrons. The other is to measure the structure at some reference scale where perturbative QCD is valid and then use perturbative QCD to evolve this behaviour to all higher scales. Lattice QCD calculations, although approaching a stage where they can be compared with some experimental features, will not be discussed further.

One of the most revealing processes to study in order to understand the composition of hadrons is lepton-hadron scattering. The lepton, believed to be point-like with no substructure, acts as a probe of the structure of the hadron. Previous experiments of this nature, for example, electron-proton scattering at SLAC [3], confirmed asymptotic freedom and the quark model of hadron structure and lead to the formulation of QCD. It has long been a goal of experimental physicists to extend the measurements of the structure of hadrons into higher energy realms where perturbative QCD can be used reliably. This also means examining the structure of the hadrons at smaller distance scale, so if new sub-structure exists, it will be seen at higher probing energies.

Previous experiments of this type have been fixed target, the lepton beam being incident upon a stationary target containing the hadrons (typically hydrogen for protons and deuterium for protons and neutrons). However, the fixed target arrangement is not an efficient way of reaching high energies in the centre-of-mass frame. For this reason, HERA (Hadron Electron Ring Anlage) has been constructed at DESY in Hamburg, Germany. This accelerator is designed to collide 30 GeV electrons (or positrons) with 820 GeV protons, giving an available energy in the centre-of-mass frame of 314 GeV, equivalent to an electron beam of 51 TeV on a stationary proton target.

Chapter 2: Physics at HERA

Introduction And General Kinematics

The basic interaction at HERA is that of electron-proton (or positron-proton) scattering. This may proceed via elastic scattering, in which both the electron and proton survive intact as shown in figure 2.1. Elastic scattering proceeds by interacting with the proton as a whole, giving information about the shape and density of the proton. Inelastic reactions, as shown in figure 2.2, are more revealing, as they break up the proton and give information about its constituents.

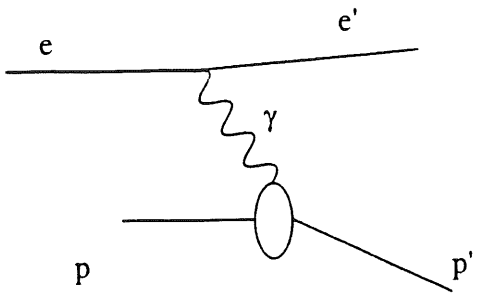

Figure 2.1: Elastic electron-proton scattering.

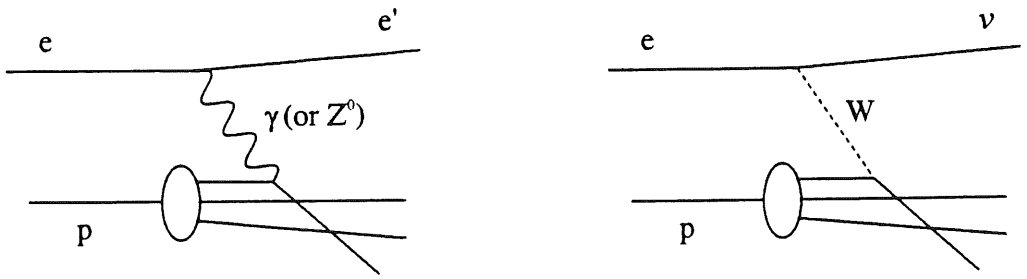

a) Neutral Current b) Charged Current

Figure 2.2: Lowest order diagrams for electron-proton inelastic scattering. a) Neutral current, mediated by photon (or Z^0), b) charged current, mediated by W.

In these reactions the virtual boson (photon, W or Z^0) emitted by the electron scatters not from the proton as a whole but from some constituent part, called a parton. Let **k** be the four-momentum of the incoming electron, **k'** the four momentum of the outgoing electron (or neutrino in the case of charged-current interactions), **p** the four momentum of the incoming proton, **p'** the four momentum of the outgoing proton and M the mass of the proton. The four-

momentum transfer, $\mathbf{q}$, may then be defined as

$$\mathbf{q} = \mathbf{k} - \mathbf{k}'$$

The square of the four-momentum transfer, Q^2, (with a conventional minus sign) is then

$$Q^2 = -\mathbf{q}^2 = -(\mathbf{k} - \mathbf{k}')^2$$

The energy transferred by the exchanged particle in the rest frame of the proton, ν, is then defined as

$$\nu = \frac{\mathbf{p} \cdot \mathbf{q}}{M}$$

The variable x (also called Bjorken x) is the fraction of the proton's four-momentum taken by the interacting parton and is given by

$$x = \frac{Q^2}{2M\nu}$$

and Bjorken y, a useful variable related to x and Q^2, is defined as

$$y = \frac{\mathbf{p} \cdot \mathbf{q}}{\mathbf{p} \cdot \mathbf{k}}$$

Deep Inelastic Scattering

One of the great successes of the quark-parton model and its generalisation, QCD, is an explanation of the phenomenon now known as Bjorken scaling [4]. It was observed that electron-proton scattering in the deep inelastic region, Q^2>10 GeV^2, could be explained by considering the process as an elastic scatter from a point-like parton with four-momentum fraction x within the proton. This meant that the cross-section as a function of Q^2 behaved in the same way as scattering from a point charge for fixed x. In fact, scaling is only exact for the

$x \approx 0.25$ region. Outside this region the simple picture of figure 2.2 begins to break down. The reasons for this will discussed in the section entitled 'Parton Distributions And Scaling Violations'.

Form Factors And Structure Functions

QED gives the differential cross section for elastic electron-muon scattering as [5]

$$\frac{d\sigma}{d\Omega}(pointlike) = \frac{\alpha_{em}^2}{4E^2 \sin^4\left(\frac{\theta}{2}\right)} \frac{E'}{E} \left[\cos^2\left(\frac{\theta}{2}\right) - \frac{q^2}{2M^2} \sin^2\left(\frac{\theta}{2}\right) \right]$$

where Ω is solid angle, α_{em} is the electro-magnetic coupling constant, E and E' are the energy of the incoming and outgoing electron respectively and θ is the angle of the scattered electron relative to its incoming direction in the rest frame of the muon as shown in figure 2.3. M is the mass of the target and q^2 is the squared four-momentum of the exchanged photon as before. This formula is called the Mott cross-section and applies to the elastic electro-magnetic scattering of any two point-like spin 1/2 particles, one of which is massive and the other light.

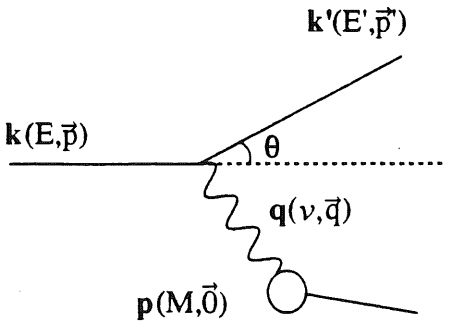

Figure 2.3: Scattering of point-like spin 1/2 particles. The upper particle is assumed light, the lower particle massive.

The proton is a spin 1/2 object but it is not point-like, having some diffuse structure in space. However, the Mott cross-section formula above may be used as the basis for the electron-proton calculation by replacing the muon current by the proton current. The muon current J_α is defined as

$$J_\alpha = \bar{u}_{\mu 2}\gamma_\alpha u_{\mu 1}$$

where γ_α are the Dirac gamma matrices. The current for the proton can be expressed in a similar way, but the gamma matrices must be replaced with a more general function that leaves the current as a Lorentz invariant. The most general form is given by

$$J_\alpha = \bar{u}_{p2}\left[f_1(Q^2)\gamma_\alpha + \frac{\kappa}{2M} f_2(Q^2) i\sigma_{\alpha\beta}\gamma^\beta + f_3(Q^2) q_\alpha\right] u_{p1}$$

where f_1, f_2 and f_3 are unknown proton elastic form factors, κ is the anomalous magnetic moment of the proton, $\sigma_{\alpha\beta}$ is related to the commutator for the gamma matrices ($\sigma_{\alpha\beta}=[\gamma_\alpha,\gamma_\beta]/2i$) and q_α are the components of the four-momentum of the exchanged photon.

The f_1 term has the same form as for a point-like charge (such as the muon) but is multiplied by a form factor that is a function of Q^2. This describes the distribution of charge within the proton. The f_2 term represents the anomalous magnetic moment of the proton, the normal magnetic moment being included in the f_1 term. The f_3 term violates parity conservation and does not enter in electromagnetic electron-proton scattering. At low Q^2, the scattering formula reduces to that for a particle with charge $+e$ and with magnetic moment $1+\kappa$. Hence, $f_1(0)=1$ and $f_2(0)=1$. If the proton were a point-like particle, f_1 would be unity for all Q^2 and κ would be zero.

Two combinations of the form factors are made to simplify experimental extraction. These are the electric and magnetic elastic form-factors, G_E and G_M, defined as

$$G_E(Q^2) = f_1(Q^2) + \frac{\kappa q^2}{4M^2} f_2(Q^2)$$

$$G_M(Q^2) = f_1(Q^2) + \kappa f_2(Q^2)$$

This gives the scattering cross-section as

$$\frac{d\sigma}{d\Omega} = \frac{\alpha_{em}^2}{4E^2 \sin^4\left(\frac{\theta}{2}\right)} \frac{E'}{E} \left[\frac{G_E^2 + \tau G_M^2}{1+\tau} \cos^2\left(\frac{\theta}{2}\right) + 2\tau G_M^2 \sin^2\left(\frac{\theta}{2}\right) \right]$$

where τ is defined as $Q^2/4M^2$. This is known as the Rosenbluth formula.

For elastic scattering, $Q^2=2M\nu$ (i.e. $x=1$). This is not the case for inelastic scattering, as the proton breaks up and so the form factors become functions of ν as well as Q^2. Hence,

$$\frac{d\sigma}{d\Omega} = \frac{\alpha_{em}^2}{4E^2 \sin^4\left(\frac{\theta}{2}\right)} \frac{E'}{E} \left[W_2(\nu, Q^2) \cos^2\left(\frac{\theta}{2}\right) + 2W_1(\nu, Q^2) \sin^2\left(\frac{\theta}{2}\right) \right]$$

where W_1 and W_2 are the inelastic structure functions.

Bjorken's Scaling Hypothesis And The Parton Model

At $Q^2>3$ GeV^2, the proton stops looking like a diffuse object and instead looks like a collection of point-like objects, called partons. This is known as Bjorken's scaling hypothesis. These partons have now been identified with the quarks and gluons of QCD. Hence the structure functions can be reduced to

$$2W_1 = \frac{Q^2}{2m^2} \delta\left(\nu - \frac{Q^2}{2m}\right)$$

$$W_2 = \delta\left(\nu - \frac{Q^2}{2m}\right)$$

as the photon is assumed to be scattering from a point-like particle of mass m. The point-like structure functions do not depend upon Q^2 and ν independently, but on the ratio $Q^2/2m\nu$.

If the interaction is between an electron and a quark with momentum fraction x (i.e. mass fraction $m=xM$), the two dimensionless structure functions F_1 and F_2 are functions of x only and are given by

$$F_1(x) = MW_1(\nu, Q^2)$$

$$F_2(x) = \nu W_2(\nu, Q^2)$$

where $x=Q^2/2M\nu$ as before. Hence

$$F_1(x) = \frac{1}{2x} F_2(x)$$

(generally true if the components of the target have spin 1/2). This is known as the Callan-Gross relation.

Parton Distributions And Scaling Violations

The dimensionless structure functions F_1 and F_2 can be related to the parton (quark and gluon) distributions in the proton. As the gluon carries no electromagnetic charge and the photon carries no colour charge, photons and gluons cannot interact directly. Hence the structure function F_2 may be expressed as a sum over the quark distributions in the proton, giving

$$F_2(x) = \sum_i e_i^2 x q_i(x)$$

where the sum i is over the quark and anti-quark flavours, e_i are the quark charges and $q_i(x)$ are the quark distributions (the chance of finding a quark of flavour i with a momentum fraction x).

However, in QCD, the situation is more complicated as instead of seeing a quark with momentum fraction x, the quark can radiate a gluon and therefore have a lower momentum fraction. The chance of resolving this gluon from the parent quark depends upon the distance scale with which the proton is probed (i.e. $1/Q^2$). This is illustrated in figure 2.4.

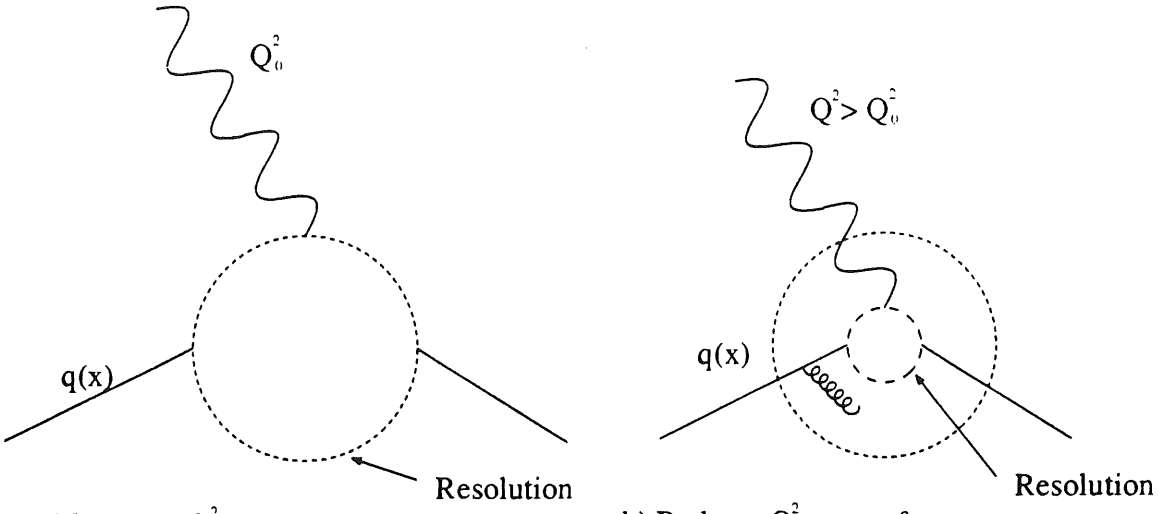

a) Probe at Q_0^2 sees q(x)

b) Probe at Q^2 sees softer q

Figure 2.4: The quark structure of the proton as seen by a virtual photon as Q^2 increases. From [5].

This effect leads to scaling violations which are predicted by QCD and have been confirmed by experiment. Thus, $F_2(x)$ is replaced by $F_2(x,Q^2)$. The quark distributions are also functions of both x and Q^2. Using QCD, the variation is found to be logarithmic with Q^2. Given the quark distributions at some reference scale, $q_i(x,Q^2_0)$, the Altarelli-Parisi equation [6] may be used to evolve the distributions to a different scale, $Q^2 > Q^2_0$. Hence,

$$\frac{dq(x, Q^2)}{d \log Q^2} = \frac{\alpha_s(Q^2)}{2\pi} \int_x^1 \frac{dz}{z} q(z, Q^2) P_{qq}\left(\frac{x}{z}\right)$$

where $\alpha_s(Q^2)$ is the strong coupling constant and $P_{qq}(x/z)$ represents the probability of a quark emitting a gluon. The expression predicts that the chance of finding a quark with momentum fraction x also has to include the chance of finding a quark, originally with momentum fraction z, that has radiated a gluon. P_{qq} is calculable in QCD. Figure 2.5 shows the deviations from scaling for F_2 compared with calculations by Gluck, Reya and Vogt [7].

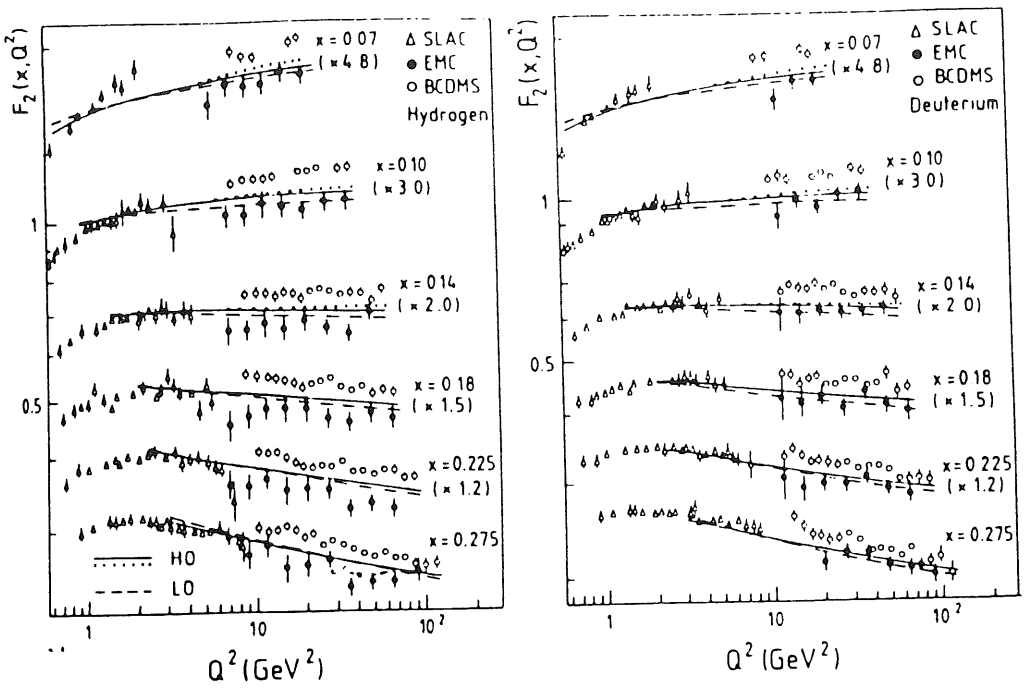

Figure 2.5: Comparison between structure function data from SLAC, EMC and BCDMS with leading order and higher order predictions of Gluck, Reya and Vogt. The dotted higher order curves are an alternative calculation of the charm quark contribution. From [7].

The neutral-current cross-section for electron proton scattering in leading-order electro-weak theory is given by

$$\frac{d^2\sigma^{nc}}{dxdQ^2} = \frac{4\pi\alpha_{em}^2}{xQ^4}\left[y^2xF_1^{nc}(x,Q^2) + (1-y)F_2^{nc}(x,Q^2) - \left(y-\frac{y^2}{2}\right)xF_3^{nc}(x,Q^2)\right]$$

and the charged current cross section by

$$\frac{d^2\sigma^{cc}}{dxdQ^2} = \frac{G_f^2 M_W^4}{\pi x\left(M_W^2+Q^2\right)^2}\left[y^2xF_1^{cc}(x,Q^2) + (1-y)F_2^{cc} + \left(y-\frac{y^2}{2}\right)xF_3^{cc}(x,Q^2)\right]$$

where G_f is the Fermi constant and M_W is the mass of the W boson.

The Callan-Gross relation, which is exact in the parton model, is now only approximately true and the longitudinal structure function F_L (defined as F_2-$2xF_1$) is non-zero at low x.

Gluons In The Proton And The Momentum Sum Rule

The structure function F_2 discussed above does not describe the full structure of the proton as, from QCD, the presence of quarks implies a cloud of virtual gluons. The presence of the gluons has been neglected except when considering the effect they have on the spectrum of the quark distributions in x. The gluons can be neglected because the virtual photon probe does not couple to the gluonic content of the proton directly. However, for hadron-hadron interactions, the gluons of one hadron must be considered as partons in their own right because they can interact strongly with partons from the other hadron. Therefore, each of the gluon colour combinations has its own gluon density $g_j(x,Q^2)$ where the subscript j represents the gluon colour and runs from 1 to 8.

It is difficult to measure the gluon distributions experimentally for the same reason that the gluon contribution could be neglected in the earlier description of deep inelastic scattering. However, an inference from the measured quark distributions is

$$\sum_{flavours} \sum_{colours} \int_0^1 dx\, xq(x, Q^2) + \sum_{colours} \int_0^1 dx\, xg(x, Q^2) = 1$$

for all values of Q^2, where q represents the quark and anti-quark distributions and g represents the gluon distributions. This expression states that the sum over all momentum fractions must be unity because the whole momentum of the proton must be carried by its constituents. This is known as the momentum sum rule.

Initially, the proton was believed to consist of three valence quarks and a sea of virtual gluons and virtual quark/anti-quark pairs with most of the proton momentum carried by the valence quarks. However, experimental measurements showed that about half of the momentum is actually by the quarks, the rest being carried by the gluons [9].

The Spin Of The Proton

In the simple parton model, the spin of the proton is the vector sum of the spins of the three valence quarks. Measurements in neutron and hyperon decays [10] show that the up and down quarks alone do not carry all of the nucleon spin, which suggests that the sea quarks may also contribute to the spin of the nucleon. Measurements by the E.M.C. collaboration [11] disproved this hypothesis by finding that the net contribution of the quarks to the nucleon spin was zero within errors. Hence, the sea quark contribution must in fact be large and negative to cancel out the valence quark contributions.

The zero net contribution of the quark spins to the spin of the nucleon may be explained using QCD [12]. Since the quarks do not carry the spin of the nucleon as predicted by the simple parton model, QCD must be used to explain which of the constituent parts of the nucleon carry the spin. This is done using the sum rule

$$\frac{1}{2}\Delta q + \Delta g + L_z = \frac{1}{2}$$

where Δq is the contribution from the quarks, Δg is the contribution from the gluons and L_z is the contribution from the orbital angular momenta of the nucleon's constituents. The net contribution from the gluons, Δg, is also found to be zero and therefore the spin must be carried by the angular momentum of the constituents. In this model the gluons carry 50% of the nucleon's linear momentum and 40% of the orbital angular momentum.

Photoproduction At HERA

Introduction

Photoproduction experiments were originally performed at fixed-target experiments using a beam of real photons incident on a stationary target (typically hydrogen or deuterium). At HERA, electron-proton scattering proceeds by the electron emitting a virtual photon which then interacts with the proton. Therefore the electrons are effectively a source of virtual photons. The regime where the photon is almost real, $Q^2 \approx 0$, is called the photoproduction region. There is a continuous transition between the photoproduction region and the deep inelastic scattering region at $Q^2 \approx 3-5$ Gev^2.

Using the electron as a source of virtual photons, the electron-proton cross section may be expressed as

$$\frac{d\sigma_{ep}}{dz dQ^2} = \frac{df_{\gamma/e}}{dz dQ^2}\,\sigma_{\gamma p}(E_\gamma)$$

where z is the fraction of the electron's energy taken by the emitted photon, E_γ is the energy of the virtual photon (given by $E_\gamma = zE_e$), $\sigma_{\gamma p}$ is the real photon-proton cross section and $f_{\gamma/\varepsilon}$ is the flux distribution of virtual photons. Assuming that the photons are almost real (i.e. that the photons are transversely polarised), the differential flux distribution may be written as

$$\frac{df_{\gamma/e}}{dz dQ^2} = \frac{\alpha_{em}}{2\pi}\,\frac{1 + (1 - z)^2}{zQ^2}$$

by using the Weizsacker-Williams formula for $f_{\gamma/e}$ [13]. The virtual photons are emitted predominantly with low values of z and Q^2. When integrating over Q^2, the limits must be specified (i.e. Q^2_{min} to Q^2_{max}) to avoid the singularity at $Q^2=0$. The differential cross section ep$\rightarrow$e'X is then

$$\frac{d\sigma}{dz}(ep \rightarrow e'X) = d\sigma_{\gamma p}\,\frac{\alpha_{em}}{2\pi}\,\frac{1 + (1 - z)^2}{z}\,\ln\frac{Q^2_{max}}{Q^2_{min}}$$

The limitations of the Weizsacker-Williams approach and a more general discussion of photon flux calculations may be found in [14], [15] and [16].

As there is a significant contribution from almost real photons, the way in which these photons interact with the proton must be considered. The interactions can be split into two classes. The first class, known as direct (figure 2.6), is where the photon interacts with one of the partons from the proton. The second class, known as resolved (figure 2.7), is where the photon fluctuates into a hadronic system and then interacts with the proton.

The resolved processes may be further divided into anomalous interactions (figure 2.7), where the photon becomes a quark/anti-quark pair, and vector meson interactions (figure 2.8), where the photon fluctuates into a system resembling a vector meson (ρ^0,ω,ϕ,J/ψ, etc.) with the same spin-parity as the photon ($J^{PC}=1^{--}$). This system contains a quark/anti-quark pair and an associated cloud of gluons. The division of the events into direct and resolved is distinct and physical, whereas the division of resolved interactions into anomalous and VMD is a continuous one, motivated by theoretical constraints.

The nomenclature of photoproduction processes described in this thesis is based on the agreed nomenclature of the photoproduction working group at the 1993 Durham QCD workshop [17]. It differs slightly from some previously published papers, for example [18], and removes the confusion arising from different uses of the term "point-like", which was used to describe direct interactions by some authors and the anomalous contribution to resolved interactions by others.

Even though the cross-section for resolved processes is reduced by a factor of α_{em} compared with direct processes, the cross section for the parton-level interactions is significantly higher when the partons can interact by the strong force. Therefore both direct and resolved interactions must be considered.

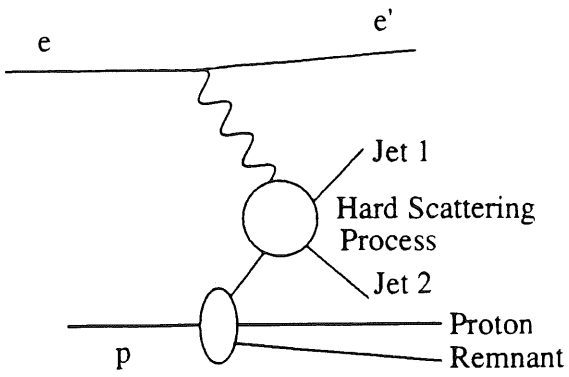

Figure 2.6: A direct interaction, in which the photon interacts directly with partons from the proton.

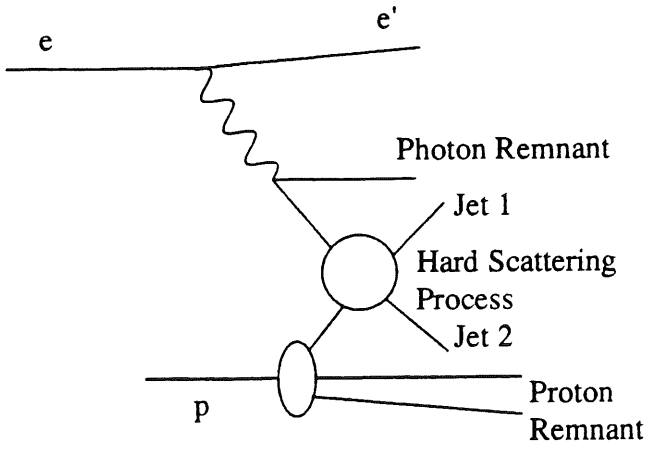

Figure 2.7: An anomalous interaction, in which the photon fluctuates to a quark-anti-quark pair.

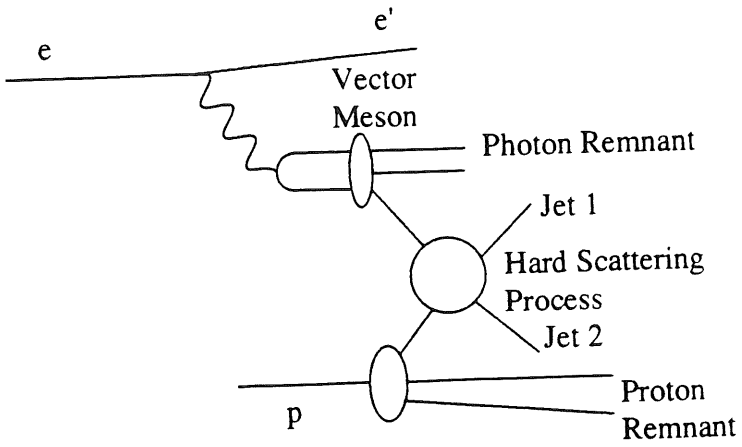

Figure 2.8: A vector meson interaction, in which the photon fluctuates to a vector meson with the same quantum numbers as the photon.

In previous experiments ([19] and the references contained therein), it was found that the data could be described very well by considering only vector meson interactions. This lead to the Vector Meson Dominance (VMD) model, where the photon is considered to be a mixture of ρ^0,ω,ϕ vector mesons [19]. The proportion of each vector meson in the mixture is given by the ratio of the couplings of the photon to the vector meson as predicted by the effective charge of the quark content of the meson. This gives the ratio $\rho^0:\omega:\phi$ as 9:1:2. This may be extended to include contributions from all other know vector mesons, which is known as the Extended Vector Meson Dominance model (EVMD) [20]. Another refinement of the basic VMD model includes a complete Veneziano spectrum of vector mesons: this is General Vector Meson Dominance (GVMD) [21].

The power of the VMD model in explaining the fixed target data may be illustrated by the Σp_T^2 spectrum of single charged particles produced by photoproduction in WA69 [18], shown in figure 2.9. The data for photon-proton scattering are scaled up by a factor of approximately 200 and compared with the data for pion-proton scattering. Only at values of Σp_T^2 above 3 GeV^2 does the photon begins to look different from a hadron.

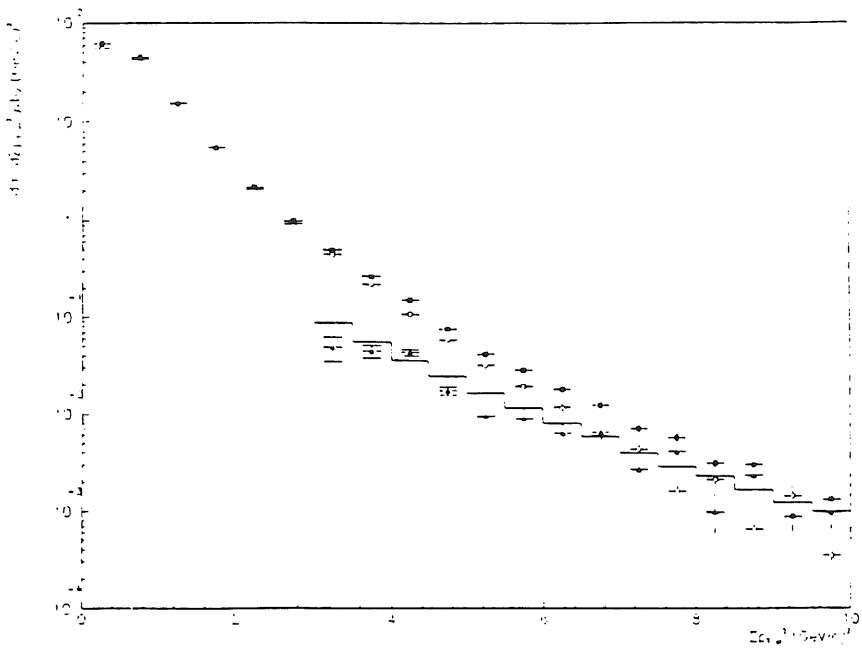

Figure 2.9: Σp_T^2 of charged particles produced in photon-proton collisions (points) compared with those produced in pion proton collisions (open points). The histogram is a Monte Carlo prediction and the triangular points are the direct contribution. From [18].

Direct Photon Interactions

There are only two different Feynman diagrams for direct photon interactions in lowest order. These are QCD Compton scattering and Boson-Gluon Fusion, shown in figure 2.10a and figure 2.10b respectively. In these interactions there is no visible structure to the photon as it always interacts with its full energy and no photon remnant is produced. Calculations of the cross-sections for direct processes appear in [22].

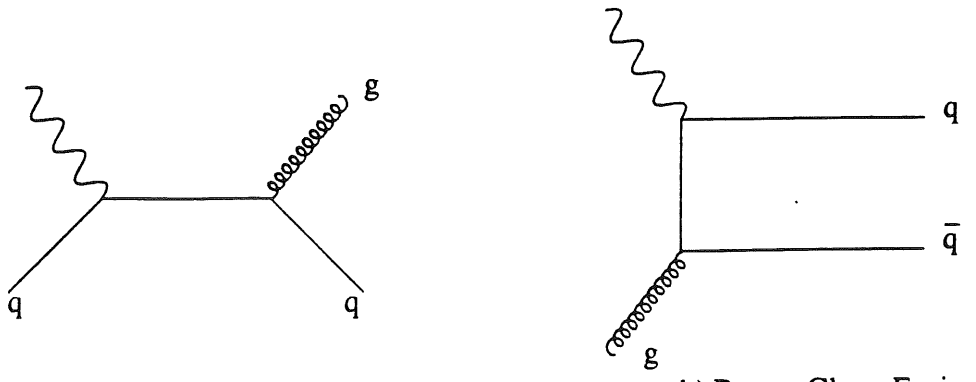

a) QCD Compton b) Boson-Gluon Fusion

Figure 2.10: Feynman graphs for hard scattering sub-processes in direct photoproduction. a) QCD Compton b) Boson-Gluon Fusion.

Resolved Photon Interactions And Parton Distributions In The Photon

In resolved interactions, the photon fluctuates into a quark/anti-quark pair (anomalous) or a vector meson (VMD). Anomalous interactions can be calculated using perturbative QCD although there is a question of how low in scale perturbation theory may be applied as the strong coupling constant, α_s, becomes large. The VMD component cannot be calculated in perturbation theory and so parameterisations must be made based on experimental measurements. This has been done using Regge theory [23] to produce fits to the fixed-target data, for example in [24].

Resolved processes can be considered to be due to quark distributions $q^{\gamma}_i(x)$ and gluon distributions $g^{\gamma}_j(x)$ inside (i.e. the photon having fluctuated to a state containing a quark or gluon) the photon with x being the fraction of the photon's four-momentum taken by the parton. This is necessary to perform perturbative QCD calculations to determine the chance of finding a quark or a gluon in the photon.

However, the momentum sum rule does not apply in the same way for the photon as it does for the proton because the photon is not composed of quarks and gluons and must fluctuate to a quark/anti-quark state before interacting via the strong force. Thus, although the sum rule must apply when the photon has fluctuated, it is possible that the photon will not fluctuate at all and therefore none of the momentum will be carried by partons. It is possible to represent the chance of the photon interacting directly by including a spike in the photon structure functions at x=1.

The structure functions F^{γ}_1, F^{γ}_2 for electron-photon scattering (where the structure of a real photon is probed by a virtual photon radiated from an electron) are defined in exact analogy with the electron-proton case. This gives the differential cross-section as

$$\frac{d^2\sigma}{dxdQ^2}(e\gamma \rightarrow eX) = \frac{4\pi\alpha^2_{em}}{xQ^4}\left[y^2 x F^{\gamma}_1(x, Q^2) + (1 - y)F^{\gamma}_2(x, Q^2)\right]$$

where x,y are Bjorken x and y for the real photon and Q^2 is the four-momentum transfer. F_1 may be found using the Callan-Gross relation

$$2xF_1^\gamma = F_2^\gamma$$

and F^γ_2 is given by

$$F_2^\gamma(x, Q^2) = \sum_i x e_i^2 q_i^\gamma(x, Q^2)$$

where e_i are the quark charges, $q_i^\gamma(x, Q^2)$ are the quark distributions in the photon and the sum i is over quark and anti-quark flavours.

The parton distributions may be parameterised by making some theoretical assumptions (for example, that the up, down, anti-up and anti-down distributions are the same). Several sets of parameterisations are available, including the three by Levy, Abramowicz and Charchula (LAC)[25], the one by Gordon and Storrow [26] and the one by Gluck, Reya and Vogt (GRV) [27].

The LAC sets are leading order and follow the approach of the earlier work by Drees and Grassie [28]. The parton distributions are obtained by taking the distributions measured at a reference value of $Q^2=Q^2_0$ and evolving them to higher values of Q^2 using the Altarelli-Parisi equation. The anti-quark distributions are assumed to be the same as the quark distributions and a division between VMD and anomalous contributions is made inside the parton distributions. The reference scale Q^2_0 is taken to be 1 GeV^2 and 4 GeV^2 for sets III and I respectively. Set II is also produced with reference scale 4 GeV^2 but using one less free parameter. The results of the parameterisation for F^γ_2 are shown in figure 2.11. The sharp discontinuities are due to the inclusion of the charm quark distribution when the mass of the photon-photon system exceeds 3 GeV.

Gordon and Storrow also take a mixture of hadronic and quark-parton model pieces in the quark and gluon distributions. The calculations are in next-to-leading order as well as leading order. Q^2_0 is taken to be 5.3 GeV^2 because for lower values the contributions from higher order terms may become significant.

GRV use the very low value of Q^2_0=0.25 GeV^2 in an attempt to generate the behaviour of the parton distributions dynamically from input distributions that are VMD motivated. Figure 2.12 shows a comparison of the GRV predictions with measurements from TPC/2γ and PLUTO.

Care must be taken to avoid double counting of diagrams when calculating VMD and anomalous contributions separately. The parameterisations of LAC and Gordon-Storrow avoid this by having the parton distributions as a sum of VMD and anomalous parts and then fitting them to data. This is essentially a phenomenological approach. GRV avoid the problem by starting with VMD and evolving all parton distributions from this dynamically.

Schuler and Sjostrand outline an alternative approach to the other structure function parameterisations in [29]. In this approach, the total cross section is decomposed into direct, anomalous and resolved components, giving the total cross section as

$$\sigma^{\gamma p}_{tot}(s) = \sigma^{\gamma p}_{direct}(s) + \sigma^{\gamma p}_{VMD}(s) + \sigma^{\gamma p}_{anom}(s)$$

A sharp cutoff is then imposed at transverse momentum, p_T=p_0, below which all interactions are assumed to be VMD and above which all interactions are considered to be the sum of direct and anomalous. Therefore, the parton distributions for anomalous and VMD processes are considered separately and double counting is avoided. However, such a sharp cutoff is somewhat unphysical as a gradual change from VMD to perturbative QCD is expected.

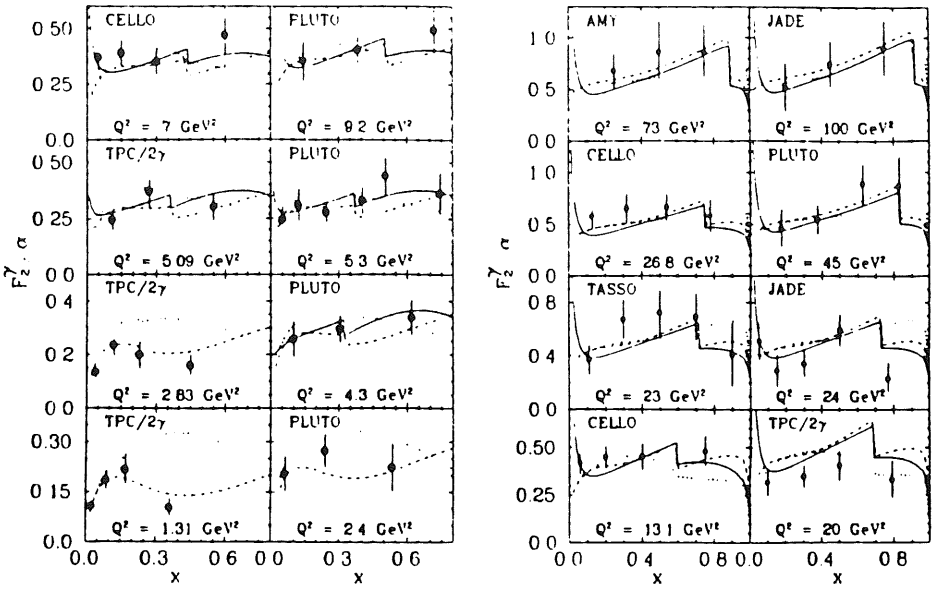

Figure 2.11: Comparison of the predictions of the LAC parameterisations for Q^2_0=1 GeV^2 (dashed line), Q^2_0=4 GeV^2 (full line) and the Drees and Grassie parameterisation (dotted line) with the measurements of F^γ_2 as a function of x in bins of Q^2. From [25].

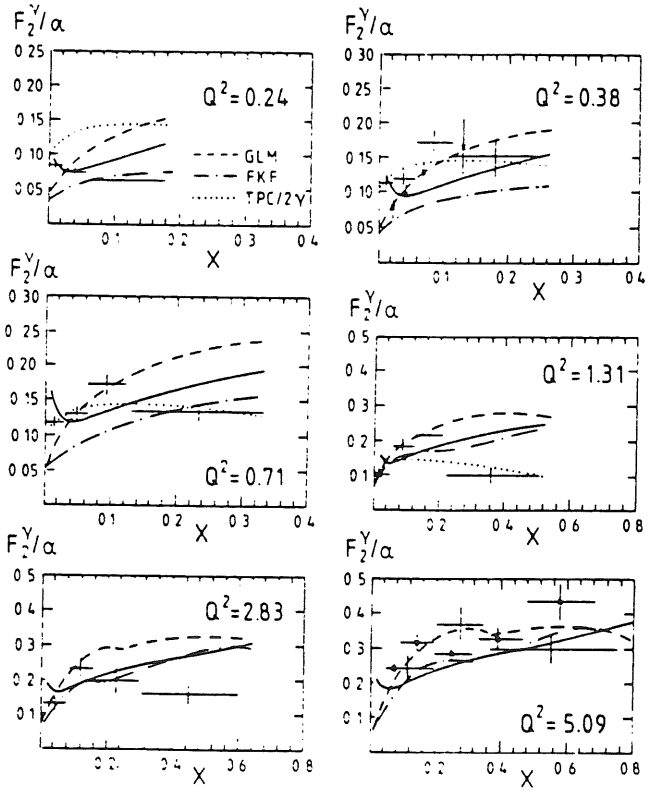

Figure 2.12: GRV predictions (solid curves) for F_2^γ compared with VMD-inspired parameterisations (dashed and dashed-dotted curves). The data from PLUTO (x) and TPC/2γ (+) are also shown The values of Q^2 are in GeV^2. From [27].

Chapter 3: HERA And H1

The HERA Accelerator

The Hadron Electron Ring Anlage (HERA) machine at Deutsches Elektronen-Synchrotron (DESY) in Hamburg is the first electron-proton (ep) colliding beam accelerator to be constructed. In previous experiments, electron-proton scattering has been performed using fixed targets. By going to a colliding beam arrangement, higher centre-of-mass energies can be achieved with the same beam energy. With HERA's design values of 30 GeV electrons on 820 GeV protons, the centre-of-mass energy is 314 GeV, equivalent to a 51 TeV electron beam in a fixed target experiment.

The rings that accelerate the two types of particle have approximately the same radius but have different designs. The electron ring uses normal magnets operating at room temperature whereas the proton ring uses superconducting magnets. This is because the designs of the two rings are driven by different limiting factors. For the electrons, the limiting factor is the rate at which they lose energy by synchrotron radiation as they traverse the curved sections of the ring. The rate of energy loss due to synchrotron radiation in a circular ring is given by

$$\Delta E = \frac{4\pi e^2}{3\rho} \beta^3 \gamma^4$$

where ΔE is the energy lost per revolution, e is the charge of the particle, ρ is the radius of the ring in metres, β is given by $\beta=v/c$ where v is the particle's velocity and c is the speed of light in a vacuum and γ is given by $\gamma=(1-\beta^2)^{-1/2}$. For relativistic electrons, $\beta\approx1$ and only the γ dependence need be considered.

For a particle with momentum p,

$$\gamma = \frac{p}{mc\beta}$$

where m is the rest mass of the particle. Therefore, γ for an electron (rest mass 511 keV) will be about 2000 times larger than for a proton (rest mass 1 GeV) of the same momentum. As the

energy loss varies with γ^4, this effect is 13 orders of magnitude larger for electrons than for protons.

The limiting factor in building an electron ring accelerator is the ability of the radio-frequency cavities to pump energy into the beam to compensate for the energy loss in the curved sections. As there is an inverse dependence on the radius of curvature, it is advantageous to build a large ring to minimize this energy loss.

For the protons, the driving factor is how much bending field can be provided by the magnets. For a particle with charge 1, the radius of curvature ρ is related to the momentum of the particle p by

$$p = 0.3B\rho$$

where B is the field in Tesla, ρ is in metres and p is in GeV. For protons, which are not limited by energy loss, the maximum momentum achievable for a ring of fixed radius is therefore determined by the magnetic field that can be supplied by the magnets.

A summary of the HERA parameters is shown in figure 3.1. Both the design parameters and the parameters as achieved in the Autumn 1992 run are shown. Unfortunately, the 1992 run only produced 32 nb^{-1} of integrated luminosity compared with a design goal of 10^5 nb^{-1} per year. This has seriously limited the physics studies possible to date.

The accelerator chain for HERA is shown in figure 3.2. Protons are produced by stripping electrons from hydrogen ions produced by an H^- source. These ions are then accelerated up to 50 MeV in a linear accelerator (LINAC) and injected into DESY III, a new synchrotron. In this ring, protons are accelerated up to 7.5 GeV, then injected into PETRA. Here, they are accelerated up to 40 GeV before final injection into the HERA proton ring. Electrons (or in the future positrons) are accelerated to 400 MeV by another LINAC, then to 7 GeV in DESY II, then to 14 GeV in PETRA and finally injected into the electron ring of HERA.

The main purpose of HERA was to extend the range of deep inelastic scattering measurements to new regions of x and Q^2. Figure 3.3 shows the region which HERA will be able

to explore by running with 820 GeV protons on 30 GeV electrons (the electron energy for the 1992 run was 26.7 GeV rather than 30 GeV). There is no overlap between the region previously measured in fixed target experiments and the region measurable at HERA. This gap may be bridged by running with lower proton beam energies.

As shown in figure 3.2, the HERA ring itself is a flattened circle with a circumference of 6.3 km, consisting of four curved sections and four straight sections. The electron and proton beams may be brought into collision at four areas. Two of these areas contain large general purpose detectors: H1 in the North Hall and ZEUS in the South Hall.

	Design		Autumn 1992		unit
	p−ring	e−ring	p−ring	e−ring	
Energy	820	30	820	26.7	GeV
Luminosity	1.5×10^{31}		3.0×10^{29}		$cm^{-2}s^{-1}$
Integrated luminosity per year	10^5		32		nb^{-1}
Interaction points (crossing angle)	4 (0)		2 (0)		(mr)
Magnetic field	4.68	0.165	4.68	0.149	T
Number of particles	210	80	2.6	3.7	10^{11}
Current per bunch	760	290	200	280	μA
Number of bunches	210	210	10	10	
Bunch separation	96	96	96	96	ns
Injection energy	40	14	40	12	GeV
Filling time	20	15	120	30	min
σ_x/σ_y at interaction point	0.29/0.07	0.26/0.02	0.36/0.10	0.30/0.07	mm
σ_z at interaction point	110	8	≈ 200	≈ 10	mm
Energy loss per turn	6.2×10^{-6}	127			MeV
RF-frequency	52.03/208.1	499.8	52.03	499.8	MHz

Figure 3.1: Summary of HERA parameters. From [30].

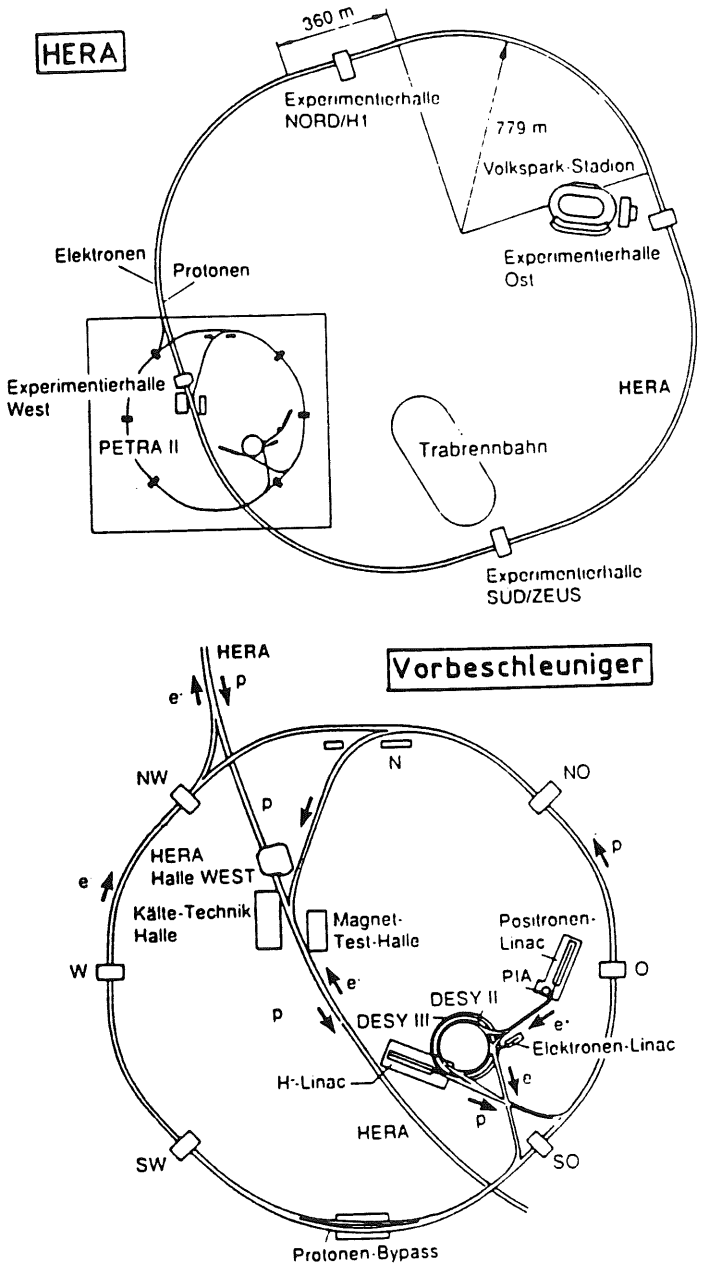

Figure 3.2: The HERA accelerator chain.

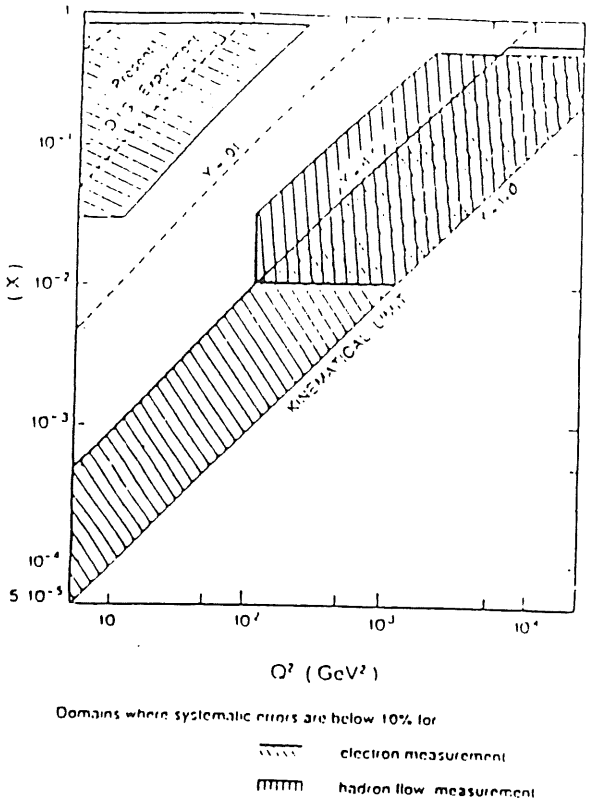

Figure 3.3: The kinematic region accessible by HERA.

The H1 Detector

As outlined in the H1 technical proposal [31], a detector for HERA has to fulfil the following general requirements:

1) It must have a high degree of hermeticity in order to investigate phenomena involving energetic neutrinos or other non-interacting secondary particles.
2) It must permit good energy flow measurements for the inclusive measurement of neutral and charge current interactions. It must have good energy resolution, fine granularity and good absolute energy calibration for both electromagnetic and hadronic calorimetry.
3) Muon identification and measurement must be present for new particle searches, for heavy flavour studies and to preserve hermeticity when high-energy muons are present.
4) Electron identification and energy resolution must be good in order to use final-state electrons to reconstruct deep inelastic scattering event kinematics.
5) It must provide tagging of electrons which have emitted a photon in the detector and are therefore scattered through low angles in order to study photoproduction processes.

The H1 detector is described fully in [30]. The detector is shown in cut-away view in figure 3.4 and in longitudinal view in figure 3.5. The detector design is highly asymmetric as most of the final state particles are forced towards the incoming proton direction to conserve momentum. The centre of mass for HERA collisions is boosted with γ=2.86 along the proton direction with respect to the laboratory frame. This leads to a difference in the required instrumentation between the forward (incoming proton beam) and backward (incoming electron beam) directions.

In the following description of the H1 detector, the standard H1 co-ordinate system will be used. This is a right-handed Cartesian co-ordinate system with the origin at the centre of the detector, which is the nominal interaction point. The positive z direction is taken to be the proton direction. The positive x direction points to the centre of HERA and the positive y direction points upwards. This is shown in figure 3.6. The polar angle, θ, is then the angle relative to the beam axis and the azimuthal angle, ϕ, is measured from the x-axis.

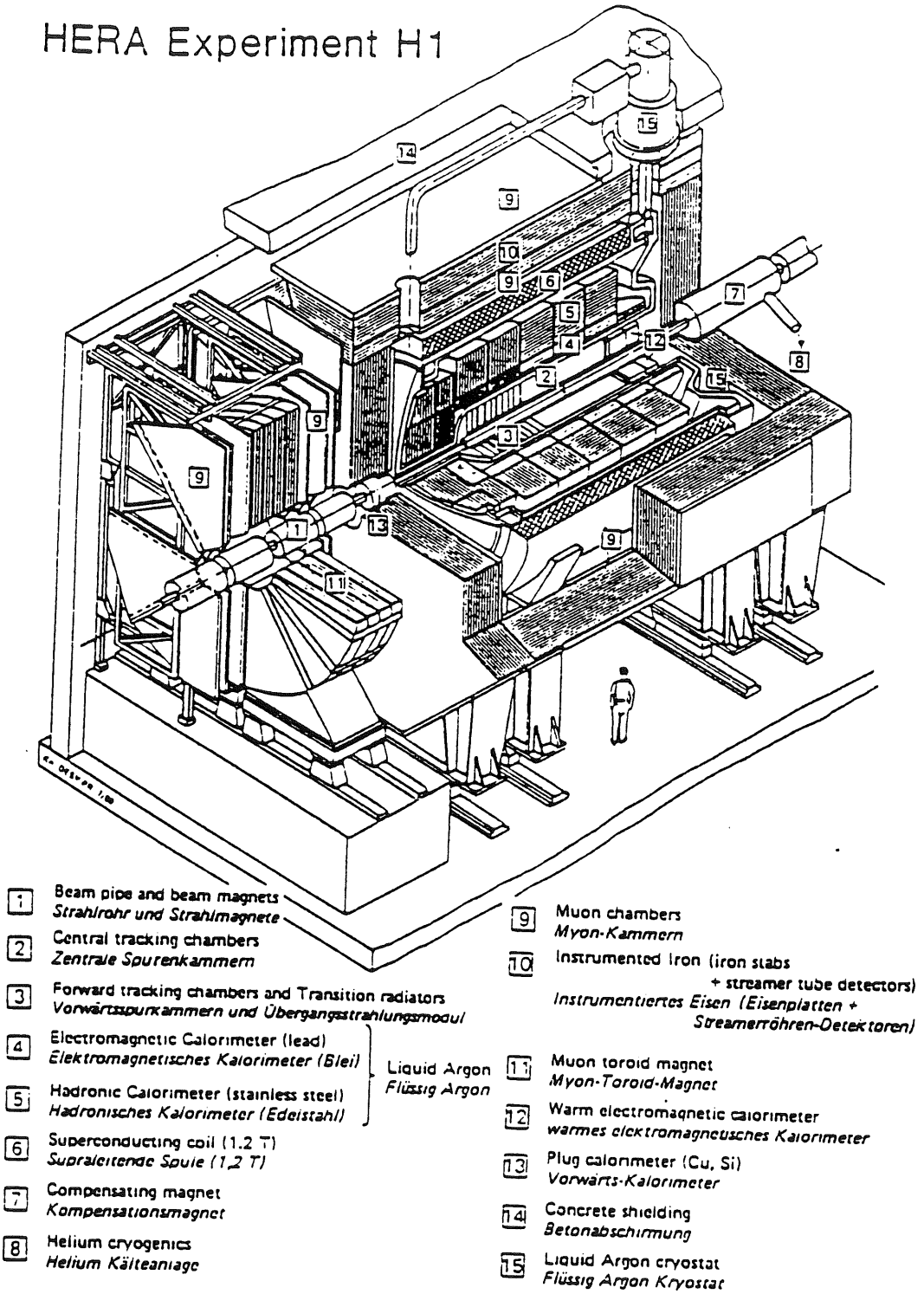

Figure 3.4: The H1 detector, cut-away view.

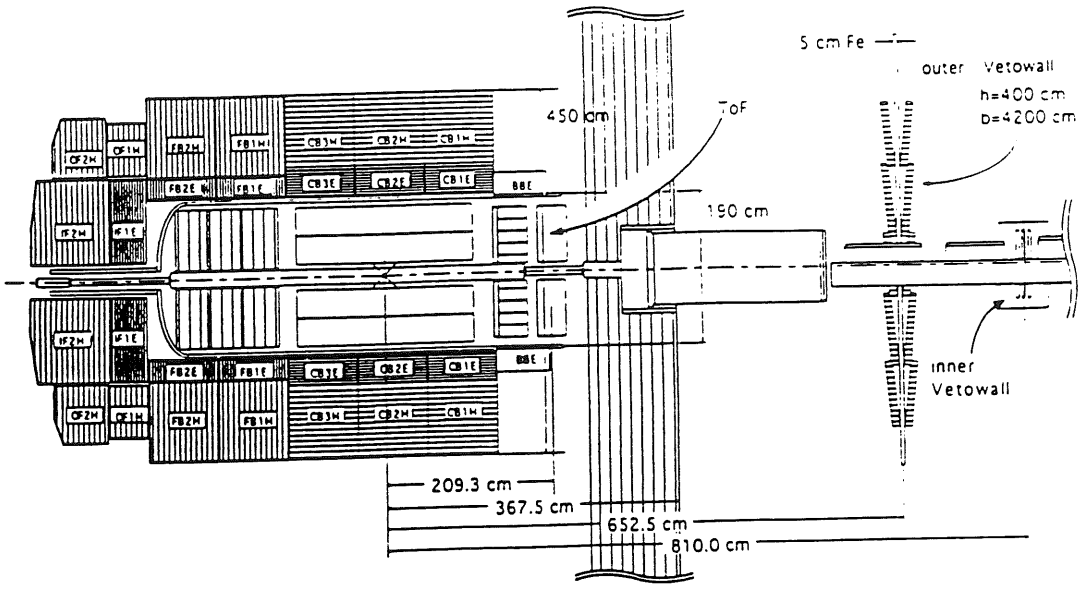

Figure 3.5: The H1 detector, longitudinal view, showing the scintillator walls.

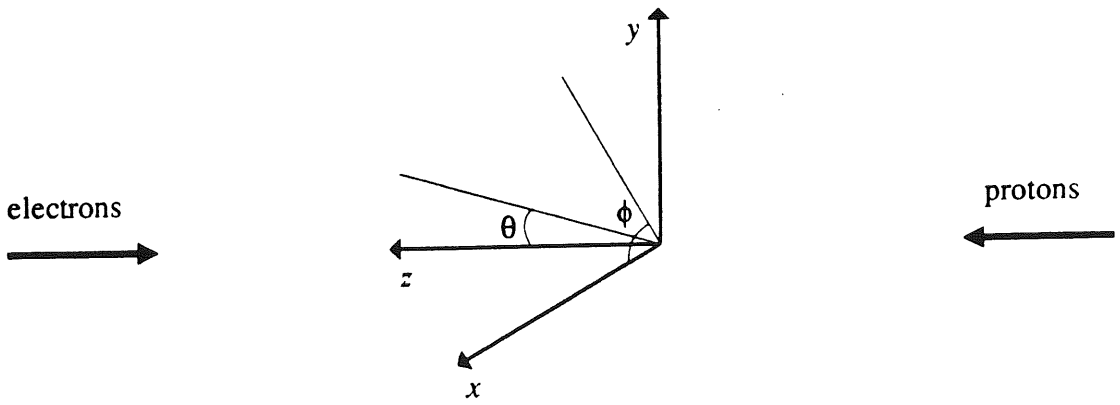

Figure 3.6: The H1 co-ordinate system.

The H1 detector consists of the following elements, proceeding outwards from the interaction point.

1) The beam pipe, having an inner diameter of 190 mm, with an aluminium wall 150 μm thick backed by 2 mm thick carbon-fibre reinforced plastic. A planned upgrade to H1 includes a vertex detector, for which a 45 mm inner diameter beam pipe will be used.

2) Tracking detectors, consisting of the central tracker (made of two jet chambers, two proportional chambers and two z chambers) and the forward tracker (made of three supermodules, each containing a radial chamber, a planar chamber, a multi-wire proportional chamber for triggering and a passive transition radiation layer).

3) Electro-magnetic calorimetry, consisting of a liquid argon-lead calorimeter in forward and barrel regions and the backwards electro-magnetic calorimeter, a lead-scintillator calorimeter, in the backwards region. A copper-silicon pad calorimeter (the Plug) closes the gap between the liquid argon calorimeter and the beam pipe in the forward region. The backwards proportional chamber is situated in front of the backwards electro-magnetic calorimeter and a scintillator wall for time-of-flight measurements is situated immediately behind.

4) Hadronic calorimetry, consisting of a liquid argon-stainless steel calorimeter in the forward and barrel regions.

5) The superconducting coil, which provides a 1.2T solenoidal field in the enclosed volume. For beam stability, a compensating magnet (with maximum field 6 T) is situated around the beam pipe to produce zero integrated field along the beam axis.

6) The warm iron return yoke for the solenoid, which is instrumented with limited streamer tubes to provide a tail-catcher for the hadronic calorimetry. The iron provides the only hadronic calorimetry in the backwards area as the liquid argon calorimeter extends only to θ=153°. The iron is also used as a muon filter and tracker, the field in the iron allowing a measurement of muon momentum to be made.

7) The forward muon spectrometer, consisting of drift chambers and an iron toroid, which is used to supplement the muon detection and momentum measurement in the forward direction.

8) Two scintillator walls (the large and small veto walls) situated at z=-6.5 m and z=-8.1 m from the H1 interaction point. These counters are used to aid in rejecting events caused by beam-wall or beam-gas interactions upstream of H1.

9) The electron and photon taggers, situated at z=-33.4 and z=-102.9 m respectively, which

are used to measure luminosity by measuring the rate of bremsstrahlung events. They are also used to tag photoproduction events with an electron in the electron tagger and no photon in the photon tagger.

The Central Tracking Detectors

The H1 tracking system is shown in figure 3.7. An end-on view of the central tracker is shown in figure 3.8. The central tracker is made from six individual detectors which were fabricated separately and then locked together to form the tracker unit.

Proceeding radially outwards from the beam, the first chamber is the Central Inner Proportional chamber (CIP). This is a multi-wire proportional chamber which provides space points for the Level 1 trigger and is read out using a pad segmented cathode with sixty pads in z and 8 in ϕ. The CIP has a double layer of chambers, formed by three concentric cylinders which are rotated by $\pi/16$ in ϕ with respect to each other. The wires run parallel to the beam with 480 wires in each layer. The chamber was operated with a 49.9% argon, 49.9% C_2H_6, 0.2% freon gas mixture in Autumn 1992. A time resolution of 21 ns was measured with test beams, and a similar performance was measured when the chamber was installed into H1. This resulted in a 2% chance of registering a given pad with the wrong (i.e. adjacent) beam crossing, giving a good signal for triggering.

The second chamber out from the beam is the Central Inner Z-chamber (CIZ). This drift chamber is designed to provide an accurate measurement of the z co-ordinate of tracks passing through the chamber as this co-ordinate is not well measured by the central jet chambers. The wires in the chamber are strung around the beam in sixteen sectors and the detector is subdivided into 15 rings in z. Each ring contains four sense wires and three potential wires. The precision of the z co-ordinate determination has been measured as 300 μm and the precision of the ϕ co-ordinate measurement performed by examining the pulses at both wire ends has been measured as 2.4% of the wire length (average wire length is 1120 mm). The maximum drift distance is 61.25 mm. The chamber was operated with an 80% argon, 20% methane gas mixture in 1992.

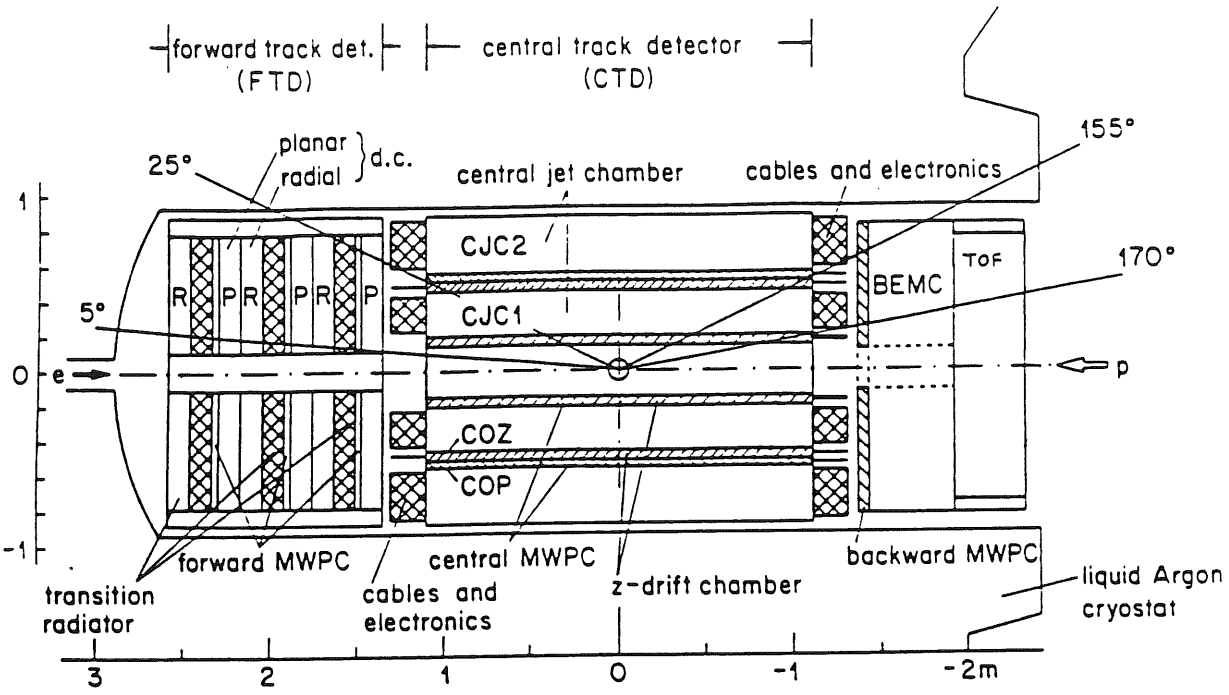

Figure 3.7: The H1 tracking system (*r-z* view).

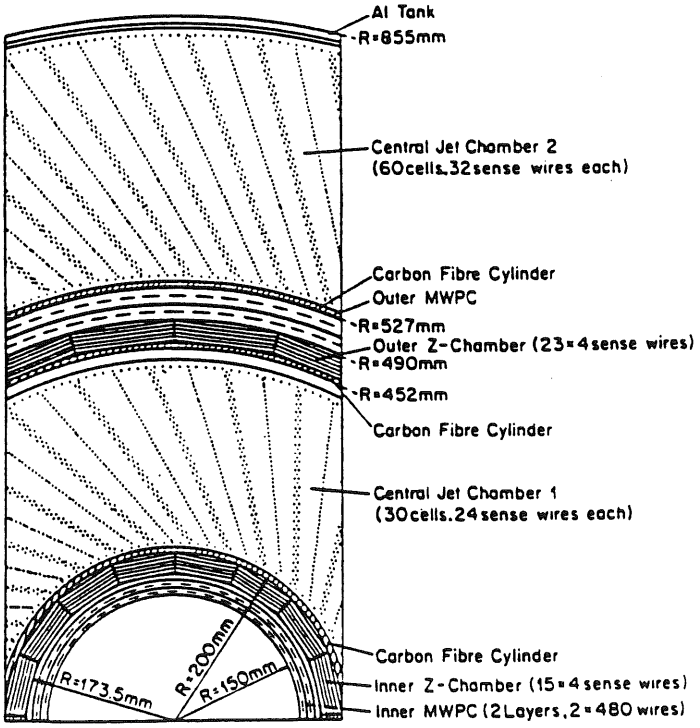

Figure 3.8: The H1 central tracker, section perpendicular to the beam.

The third chamber is the inner Central Jet Chamber (CJC1). This chamber provides a good measurement of the position of tracks in the r-ϕ co-ordinates and a moderate measurement in z using charge division. The chamber is a jet chamber of the JADE type [32] with wires strung parallel to the beam axis but staggered at an angle of 30° with respect to the radial direction. Using this design optimises the track momentum resolution by ensuring that the ionisation electrons drift approximately perpendicular to the radial direction inside the H1 solenoidal field. It also allows resolution of drift ambiguities by connecting track segments of different cells. Each high-momentum track crosses the sense wire plane at least once in CJC1, allowing a determination of the passing time of the particle to 0.5 ns and giving a good trigger separation between beam crossings. Each plane of anode sense wires is surrounded by two adjacent cathode planes of wires shaping the drift field. An individual cell extends azimuthally from the sense wire plane to both cathode wire planes and radially over the whole of CJC1. CJC1 has 30 cells each with 24 sense wires. The resolution of CJC1 has been measured as 170 μm in r-ϕ and 2.2 cm in z. The chamber was operated with 89.5% argon, 9.5% CO_2 and 1.0% methane in 1992. The design of the chamber also allows a measurement of dE/dx, the specific energy loss, which is useful for particle identification. The resolution of the dE/dx measurement was measured as 10% for the Autumn 1992 run.

The fourth chamber is the Central Outer Z-chamber (COZ). This is similar to CIZ except that it is made up of 24 segments and 24 rings in z, with four sense wires and six potential wires per ring. The resolution in z has been measured as 200 μm and the resolution in ϕ was measured as 2% of the wire length (average wire length 2970mm). The maximum drift distance is 45 mm. The chambers were operated with a 50% argon, 50% C_2H_6 gas mixture in 1992.

The fifth chamber is the Central Outer Proportional chamber (COP) which is similar to CIP. The COP inner layer has 1574 wires and COP outer layer has 1615. COP has 16 pads in ϕ and 18 in z. The time resolution of COP was measured as 40 ns.

The sixth chamber is the outer Central Jet Chamber (CJC2). This is similar to CJC1 with 60 cells, each containing 32 sense wires. The chamber was run with the same gas mixture as CJC1 and was measured to have a similar resolution in r-ϕ, z and dE/dx.

The Forward Tracker

The forward tracker, shown in figures 3.7 and 3.9, is designed to measure tracks in the forward region, $5° < \theta < 30°$. It consists of three supermodules, each of which contains a planar chamber, a multi-wire proportional chamber (MWPC), a transition radiator and a radial chamber.

The planar chambers are constructed from three layers of drift chambers with parallel wires (perpendicular to the beam direction) each rotated by 60° from the previous layer in azimuthal angle. Each module contains 32 drift cells of identical rectangular cross section and wire lengths varying between 460mm and 1410mm. Each cell contains four sense wires, each surrounded by four grid wires on a 6 mm square matrix. The planars were operated with a gas mixture of 89% argon, 10% C_3H_8, 1% C_2H_5OH in Autumn 1992 and were measured to have a spatial resolution of 150 μm.

The radial chambers, which consist of wires strung radially, is split into 48 sectors in ϕ. Each sector is a drift cell having 12 sense wires, staggered alternately 287 μm either side of a plane which bisects the sector. Between adjacent sense wires, placed on the plane which bisects the sector, are field wires parallel to the sense wires. The sense wires of one sector are connected at the inner radius to the sense wires of the sector 105° away in ϕ. The reason for connecting two wires together is because it is not physically possible to site preamplifiers and electronics at the inner radius. A determination of the radial co-ordinate is still possible by using charge division, with a decision on which wire was stuck being based upon the charge division algorithm. The chambers were run with a 50% argon, 50% C_2H_6 mixture in 1992 although the design gas mixture is 40% helium, 40% C_2H_6, 20% xenon. The resolution achieved in 1992 was 180-200 μm in the drift co-ordinate and 3 cm in the charge division co-ordinate but it is expected that this will be improved in later runs.

In the 1992 run, the pattern recognition and reconstruction of tracks in the forward tracker was poor and therefore the forward tracker was not used in analysis of the early data. This situation has been remedied for the 1993 run.

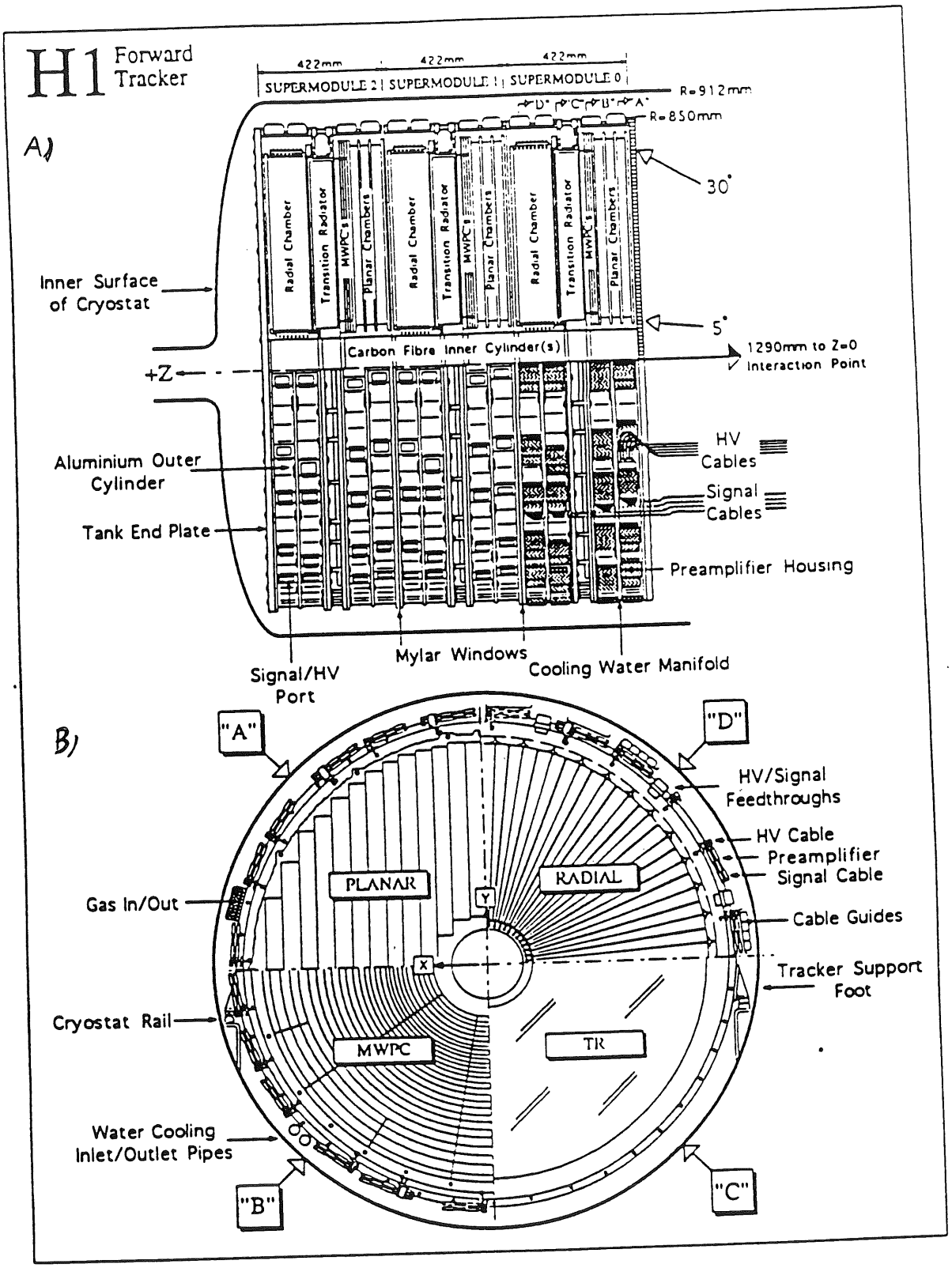

Figure 3.9: The H1 forward tracker. a) Cross section in the r-z plane showing the three supermodules. b) Cross section in the r-ϕ plane showing the cell structure of each supermodule component in one quadrant.

The forward MWPCs are present to give fast signals for triggering purposes. They consist of two planes of wires interleaved with three cathode planes. The cathode pads are radially segmented into twenty rings and azimuthally segmented into sections covering $\pi/8$ except for the four outer rings which are segmented to cover $\pi/16$. Two consecutive cathode pads are offset by half a ring which effectively doubles the resolution in polar angle. The gas mixture used was 89.4% argon, 9.9% C_3H_8, 0.7% C_2H_5OH in 1992. For tracks crossing all three supermodules, the time resolution was measured to be 20 ns.

The last component of a supermodule is a transition radiator. This passive unit consists of an array of 400 polypropylene layers and is designed to aid electron-pion discrimination in the forward direction. Transition radiation occurs when a charge particle traverses an interface between media whose magnetic or dielectric properties differ [33]. If layers of radiating foils are arranged correctly, it is possible for interference to give rise to a threshold effect and for a given energy, electrons may be made to radiate while pions will not radiate.

The photons emitted by electrons traversing the foils are detected in the radial chambers, which are separated from the transition radiators by a thin window. The design goal is to achieve a 90% electron acceptance with less than 10% pion contamination for particles up to 80 GeV which pass through all three supermodules. Tests in a beam at CERN have shown that this is possible with the design 40% helium, 40% C_2H_6, 20% xenon gas mixture.

Liquid Argon Calorimeter

The liquid argon (LAr) calorimetry covers the forward ($4° < \theta < 20°$) and barrel ($20° < \theta < 152°$) regions. Both the electro-magnetic (EM) and hadronic liquid argon calorimeters consist of plates of metal (lead for the EM and steel for the hadronic) immersed in liquid argon. Both calorimeters are enclosed in a single liquid argon cryostat to avoid cracks and to minimise dead material.

Liquid argon calorimeters function by producing showers in the metal which then produce ionisation in the liquid argon gaps. The plates have electrodes attached to either side maintaining a potential difference in the gap. Thus, the electrons produced by the shower drift towards the positive plate and are amplified to produce an output signal proportional to the energy deposited in the gap. The plates are arranged in segments which are orientated to ensure that a particle coming from the interaction vertex is as near to normal incidence as practical (never more than 45° from normal incidence).

The segmentation of the calorimeter is shown in figures 3.10 and 3.11. The LAr is segmented along the beam axis into eight self-supporting wheels named IF, OF, FB2, FB1, CB3, CB2, CB1 and BBE for the EM calorimeter, which has no counterpart in the hadronic calorimeter. Each wheel is segmented into eight octants or stacks. The cracks between octants in the EM calorimeter point to the vertex in ϕ, but the cracks in hadronic calorimeters are designed not to point to the vertex in ϕ, as shown in figure 3.11.

Each electromagnetic stack consists of a pile of G10 (epoxy and fibreglass)-lead-G10 sandwiches separated by spacers to define the liquid argon gaps. The lead plates are 2.4 mm thick with 2.35 mm liquid argon gaps. Each gap has one readout plane and one high voltage plane. The total thickness of the EM calorimeter varies between 20 and 30 radiation lengths (X_0), as shown in figure 3.12.

Each hadronic stack consists of a pile of 19 mm stainless steel plates and 4.8 mm active gaps. In the middle of each active gap is a G10 board with pads on both sides. The high voltage planes are glued to the inner surfaces of the stainless steel plates. The hadronic calorimeter consists of between five and eight interaction lengths (λ) as shown in figure 3.12.

The energy resolution of the liquid argon calorimeter has been measured in electron and pion test beams and using data taken in place by H1. Figure 3.13 shows the energy resolution versus energy for electrons, figure 3.14 for pions. The parameterised form of the energy resolution, $\sigma(E)/E$, is

$$\frac{\sigma(E)}{E} = \sqrt{\frac{A^2}{E} + \frac{B^2}{E^2} + C^2}$$

where $A=11\%/\sqrt{E}$ $GeV^{0.5}$, B=154 MeV and C=0.6% for electrons and $A=(50.7\pm0.1)\%/\sqrt{E}$ $GeV^{0.5}$, B=0.9 GeV, $C=1.6\pm0.1\%$ for pions.

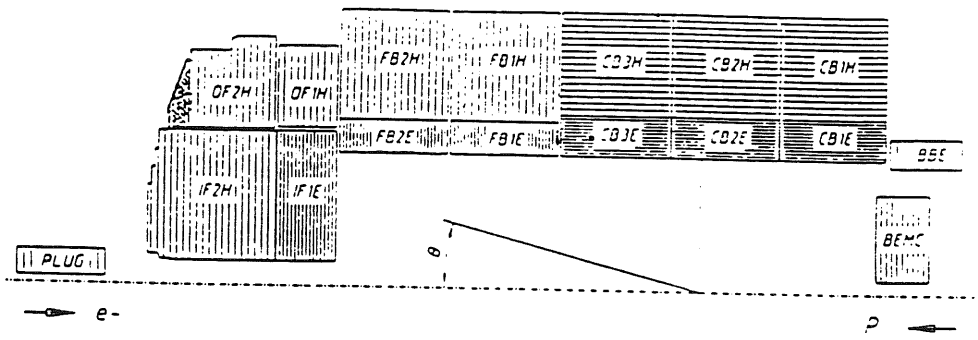

Figure 3.10: Longitudinal view of the H1 liquid argon calorimetry.

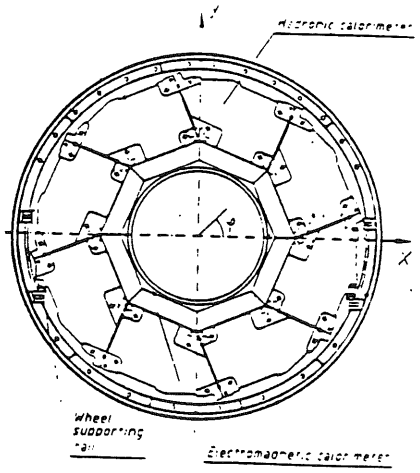

Figure3.11: A radial view of a single liquid argon calorimeter wheel.

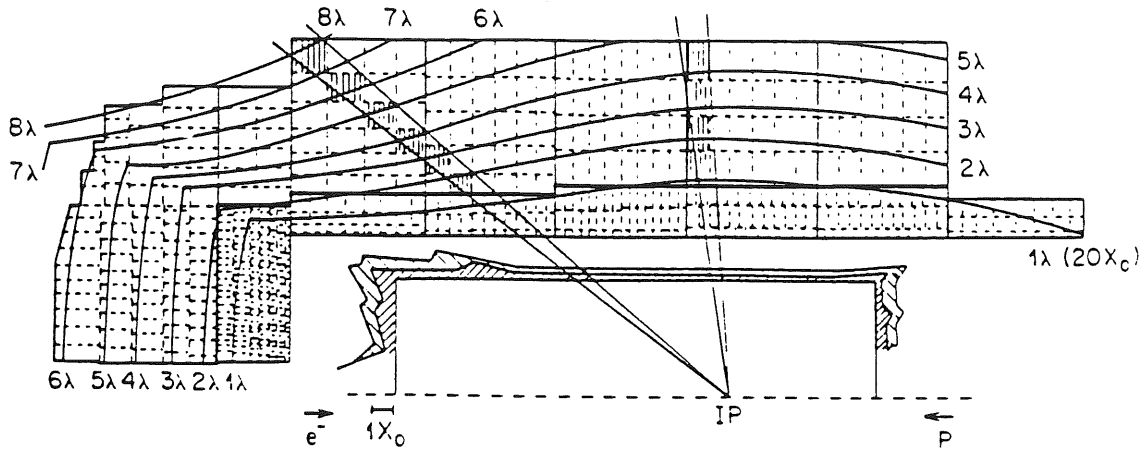

Figure 3.12: Longitudinal view of the liquid argon calorimeter showing lines of iso-X_0 and iso-λ. The hatched areas in front of the calorimeters correspond to the material of the trackers and cryostat. All amounts of material are for a particle from the interaction point (IP). The dashed lines show the segmentation.

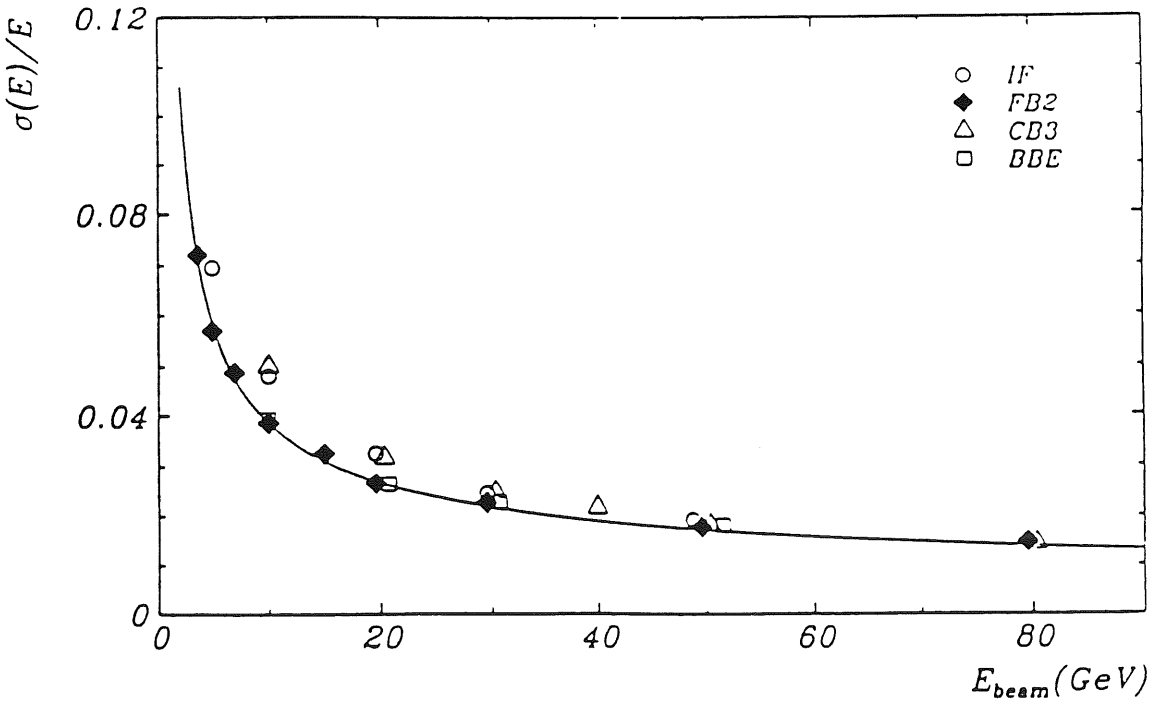

Figure 3.13: Energy resolution as a function of energy for electrons for wheels BBE, CB3, FB2 and IF. The solid line is the parameterisation of the energy resolution for FB2.

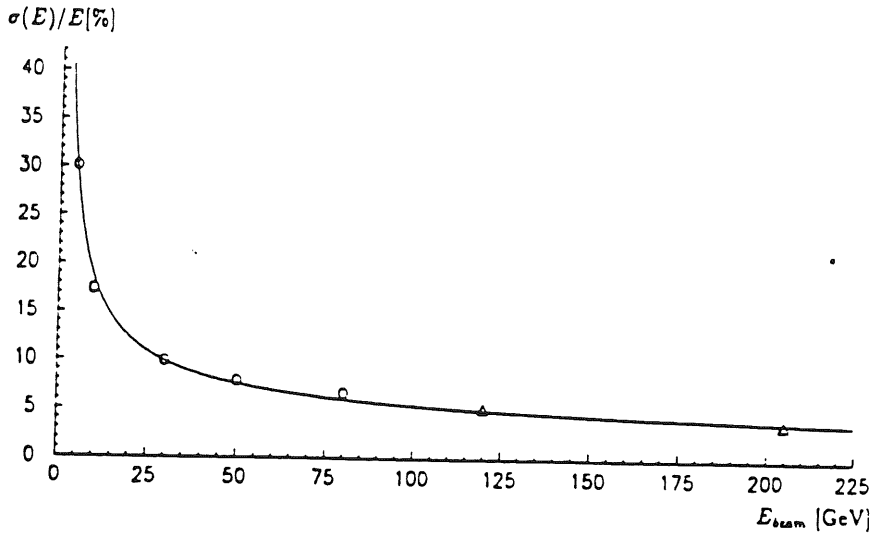

Figure3.14: Energy resolution as a function of energy for pions. The circles are for wheel IF only, the triangles are for wheel IF with the iron tailcatcher included. The solid line is a parameterisation of the resolution.

The Backwards Electro-magnetic Calorimeter And The Backwards Proportional Chamber

The Backwards Electro-magnetic calorimeter (BEMC), shown in figure 3.15, is designed primarily to measure electrons scattered at small angles in deep inelastic scattering. The BEMC covers the angular range $151° < \theta < 177°$. The BEMC is a lead-scintillator calorimeter in which the showers produced in lead plates cause ionisation of atoms in the scintillating material, resulting in the production of light as the ions and electrons recombine.

The BEMC contains 88 calorimeter stacks aligned parallel to the beam line. There are 56 stacks with a square cross-section, the others being trapezoidal or triangular in order to fill the circular barrel. The basic layer consists of 2.5 mm of lead followed by 4 mm of plastic scintillator. Each stack contains 50 layers, corresponding to 22.5 radiation lengths.

The BEMC is read out via a 0.3 mm air gap to wavelength shifter bars. Two pairs of 8 cm bars cover two opposite sides of a square stack and extend over the full active length. The remaining two sides are covered by 16 cm wide bars which cover only the last 15 sampling layers in the stack, giving access to the tails of showers (the last 6.8 radiation lengths). The light emitted in the wavelength shifters is then read out by photo-diodes (one per bar).

The BEMC resolution has been determined in test beams to be $10\%/\sqrt{E}\oplus 1\%$. The average noise per calorimeter stack has been measured as 150 MeV. The uncertainty in calibration between stacks has been estimated as 3%. The position resolution for electrons has been measured to be 1.3 cm.

As the H1 hadronic liquid argon calorimeter does not cover the backward area, the BEMC must be used in conjunction with the iron tailcatcher to provide a measurement of hadronic energy flow. However, as the BEMC only corresponds to 0.97 hadronic interaction lengths, using the BEMC for hadronic calorimetry is problematic. About 30% of all hadrons do not produce any showers in the BEMC and their minimum-ionising signal is not detectable above the noise. When a hadron does produce a shower in the BEMC, only about 30% of the energy of the shower is contained within the BEMC. A hadronic energy resolution of $80\%/\sqrt{E}$

has been determined from simulation but a full study of the real detector's hadronic response is still in progress.

The Backwards Proportional Chamber (BPC) consists of five graphite cathode planes on Mylar foil and four anode wire planes. The BPC sits on the front face of the BEMC to improve the position resolution for scattered electrons and to provide trigger signals. Unlike the other H1 MWPCs, the BPC cathode is not segmented and the anode wires are read out. The wires are strung every 2.5 mm, perpendicular to the beam, and are horizontal, vertical, +45° and -45° for the four planes. The chamber was operated with a gas mixture of 49.9% argon, 49.9% C_2H_6, 0.2% in 1992. The points given by the BPC lead to an angular resolution of 0.5 mr, the same order of magnitude as the deviation of a particle's trajectory caused by multiple scattering in the material between the interaction point and the BPC. The time resolution of the BPC has been measured as 20 ns.

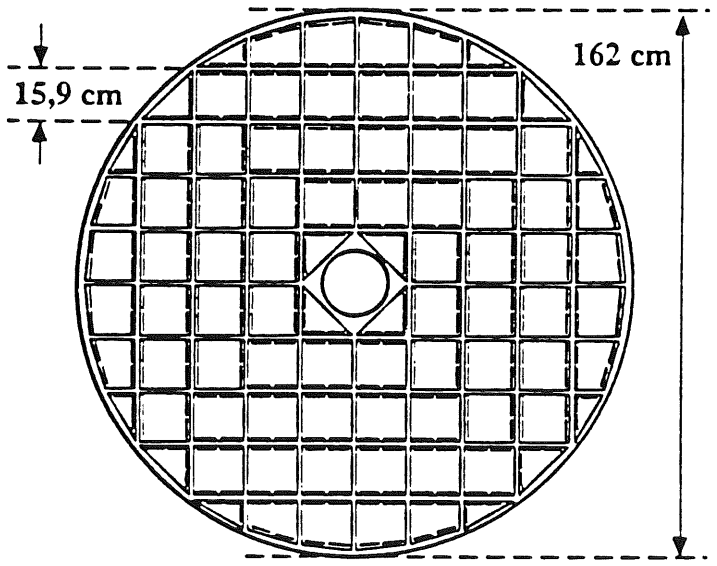

Figure3.15: The Backwards Electromagnetic Calorimeter, BEMC (x-y view).

The Plug Calorimeter

The plug calorimeter is designed to fill the gap in acceptance between the liquid argon calorimeter, which ends at $\theta=3°$, and the beam pipe, which begins at $\theta=0.6°$. The plug is a silicon-copper detector, where the silicon is used as a reverse-bias diode with a large depletion region. Showers produced in the copper produce electron-hole pairs in the silicon which are collected to give the signal. The energy resolution for hadrons has been measured as $150\%/\sqrt{E}$. The plug was not fully instrumented for the Autumn 1992 run and it will not be discussed further.

The Instrumented Iron

The instrumented iron serves three purposes in H1. Firstly, it acts as a return yoke for the superconducting solenoid. Secondly, it acts as a tail-catcher calorimeter to contain hadronic showers that escape from the liquid argon calorimetry. Finally, the iron acts as a muon filter and allows a measurement of muon momentum to be made as the iron is magnetised.

In order to be able to measure hadronic energy flow, the iron has gaps in it containing gas counters operated in limited streamer tube mode. These tubes are oriented along the beam axis in the barrel region ($25° < \theta < 130°$) and vertically in the forwards and backwards endcaps. The tail catcher covers the angular region $5° < \theta < 175°$. Of the 16 layers of streamer tubes in the iron, 11 are equipped with readout pads varying in size from 30 cm x 30 cm in the endcaps to 50 cm x 40 cm in the barrel region. The pad signals from the five inner and six outer layers are summed to form inner and outer towers. The energy resolution for hadrons has been measured as $100\%/\sqrt{E}$.

Muon measurement is provided by muon boxes. Inside the inner radius of the iron is a muon-box consisting of three layers, two strip layers with strips perpendicular to the wire direction and one pad layer. Pad layers are also installed in the first three iron slits for the calorimeter. The fourth slit is twice the width of the others and contains two chamber layers, one pad and one strip. Pad layers are inserted in the remaining five slits and another muon-box is attached to the outside of the iron.

The instrumented iron chambers were operated with a 88% CO_2, 2.5% argon, 9.5% isobutane gas mixture in 1992. The detector resolution for space points was measured to be 10 cm for the pad readout tubes, 3-4 mm for wire hits and 10-15 mm for strip hits.

The Forward Muon Spectrometer

The Forward Muon Spectrometer is designed to provide muon tagging and momentum measurement in the forward region, $3° < \theta < 17°$, and will be discussed in detail in chapters four and five.

The Time-Of-Flight Device And The Veto Walls

The time-of-flight (TOF) device, shown in figure 3.16, consists of two scintillator walls situated behind the BEMC. The function of the TOF is to provide timing information for the level one trigger in order to be able to reject proton beam related backgrounds. Losses from the beam occur due to the protons interacting with residual gas in the beam pipe and interactions between off-momentum beam particles and the wall, producing showers of hadrons and halo muons which can extend for 30 m or more along the beam direction. It is expected that H1 will typically be hit by such background events at a frequency of 2.6 MHz.

Each of the two TOF walls consists of a 3 cm thick layer of plastic scintillator sandwiched between two 6.5 mm thick lead layers, mounted on a backing plate of non-magnetic steel. The lead, corresponding to 1.1 radiation lengths, absorbs synchrotron radiation, protecting the counters and limiting the background rates. The TOF is read out by photo-multiplier tubes.

The TOF has been measured to have a time resolution of 4 ns, although the individual counters were found to have a resolution of 2 ns. The TOF provides a trigger signal within 250 ns of an interaction occurring. Figure 3.17 shows a typical time distribution of hits in the TOF and clearly illustrates the discrimination that is possible between background events and data events.

The large and small veto walls are situated at z=-6.5 m and z=-8.1 m respectively, as

shown in figure 3.5. These counters consist of double layers of plastic scintillator and are designed to provide additional time-of-flight information for background rejection. The small (or inner) veto wall covers the region near the beam pipe down to a radius of 11 cm. The large (or outer) veto wall overlaps the inner veto wall and most of the instrumented iron endcap. There is a 3m thick concrete wall between the large veto wall and the H1 detector.

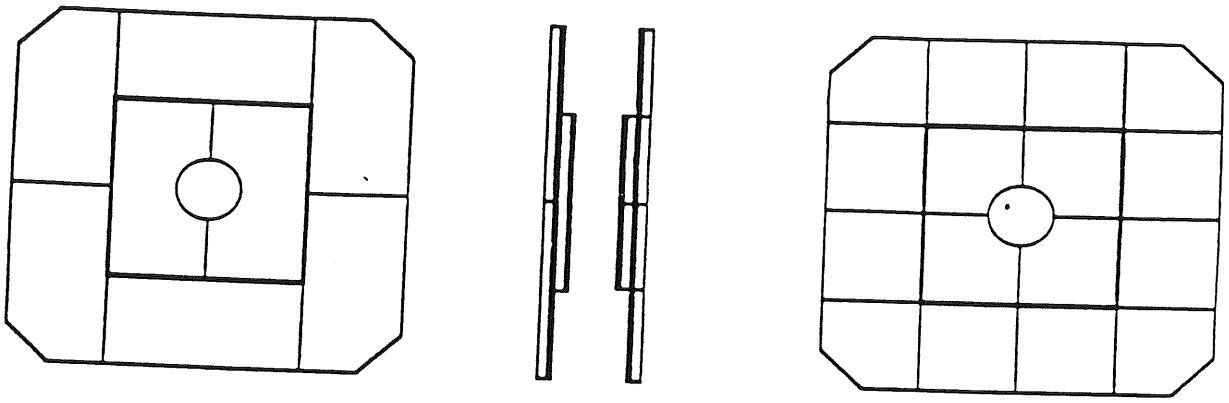

Figure 3.16: The TOF device.

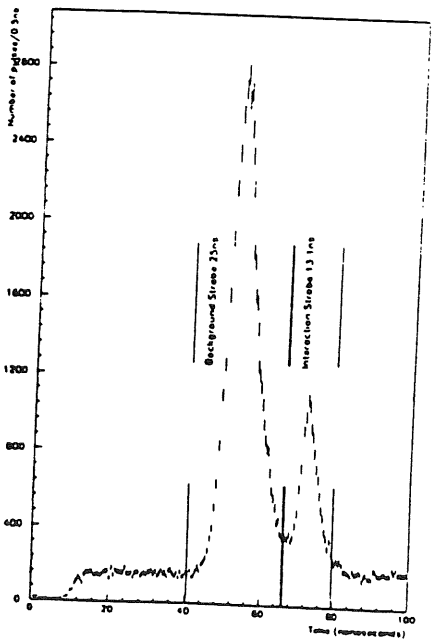

Figure 3.17: Time distribution of hits in a TOF counter, showing a clear discrimination between background and data.

The Luminosity System

The H1 luminosity monitor consists of two counters, an electron (e) tagger located at $z=-33.4$ m and a photon (γ) tagger at $z=-103$ m. The counters are placed close to the beamline in order to detect particles scattering through small angles at the interaction point. The luminosity is determined by measuring the rate of Bethe-Heitler events (i.e. $ep \rightarrow ep\gamma$), which have an electron in the electron tagger and a photon in the photon tagger.

The luminosity system is shown in figure 3.18. Scattered electrons are deflected by a set of quadrupoles and a bending magnet such that they pass through an exit window at $z=-27.3$ m to hit the electron tagger. The bremsstrahlung photons leave the proton beam pipe through the photon exit window at $z=-102.9$ m, pass through a two radiation length lead filter followed by a one radiation length water Cerenkov counter before hitting the photon detector. The lead protects the counter from the high flux of synchrotron radiation. The Cerenkov counter is used to detect whether the photon has passed through the lead without interacting.

The luminosity detectors are total absorption Cerenkov calorimeters made of KRS-15 crystals (78% TlCl and 22% TlBr). They correspond to 0.93 radiation lengths and have a crystal length of 20 cm. The energy resolution of both counters has been measured as $10\%/\sqrt{E}\oplus 1\%$ and the time resolution as 3 ns. The position resolution has been measured as 0.3 mm for the electron tagger and 1.2 mm for the photon tagger.

In addition to their luminosity measuring function, the counters may be used to trigger on photoproduction events where the scattered electron is detected in the electron tagger. The acceptance of the luminosity system, summarised in figure 3.19, allows the detection of such events with $Q^2<0.01$ GeV^2 and $0.2 < y < 0.8$.

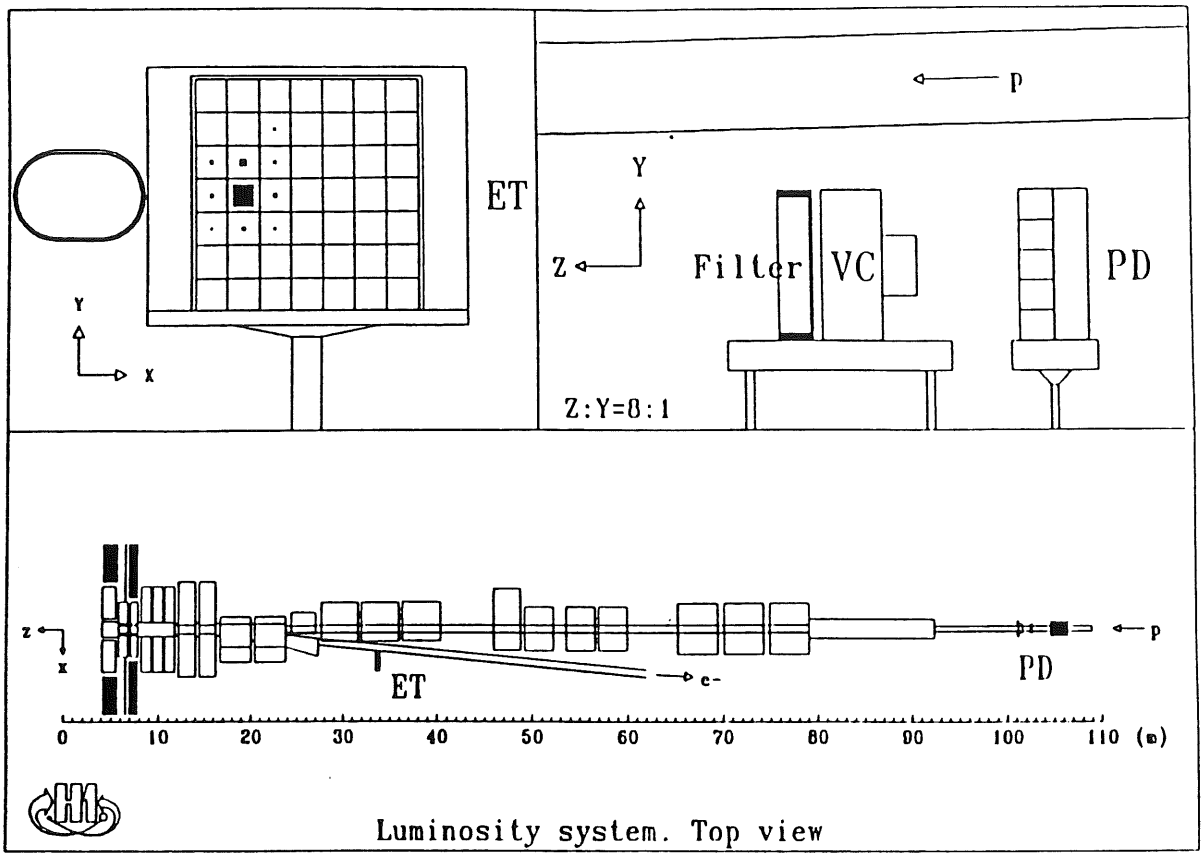

Figure 3.18: The H1 luminosity monitoring system.

	unit	ET	PD
Energy interval, $E_\gamma/E_e = 1 - E_{e'}/E_e$		0.2 – 0.8	0.004 – 1.0
Polar angle acceptance interval	mrad	0 – 5	0 – 0.45
Average acceptance for luminosity events	%	48	98
Average acceptance for photoproduction	%	36	–
Visible $ep \rightarrow ep\gamma$ cross section	mb	28	174
Luminosity rate for $E > E_{th_\gamma} = 4$ GeV	MHz	0.4	1.3
Photoproduction event rate	Hz	20 – 30	–

Figure 3.19: The acceptance of the luminosity system.

Trigger and Data Aquisition

The H1 trigger system was designed to distinguish electron-proton collisions from background processes at a rate which is comparable with the time taken for the next bunch crossing to occur. Typical background processes are caused by off-momentum protons hitting the beam wall and other components, protons interacting with residual gas nucleii and synchrotron radiation from the electron beam. As the rate of ep collisions is small compared with the background rate, the trigger has to be very efficient at keeping ep events but at the same time remove a large fraction of the background events.

The ep collisions should occur within the fiducial volume of the ep interaction region (i.e. within $\approx$1m of the nominal interaction point). In contrast, beam-wall and beam-gas interactions may take place anywhere and hence those outside the fiducial volume may be rejected. The remaining backgrounds within the fiducial region may be rejected by making further requirements on the event topology. Hard scattering events have a higher total transverse energy than background events. Charged-current deep inelastic scattering events may be identified by searching for missing transverse energy and neutral-current deep inelastic scattering events may be identified by searching for isolated energy deposition in the calorimeters from the scattered electron. Photoproduction events may be triggered by requiring an electron in the e-tagger and no photon in the γ-tagger. Heavy flavour states producing muons may be triggered by searching for muon candidates in the instrumented iron and forward muon spectrometer.

All detector readout is first performed into 'pipelines' which store the digitised signals until a trigger 'keep' signal (i.e. a signal to accept the event) is received or until the pipeline can no longer store the information. This system was necessary to allow H1 to trigger at a beam crossing interval of 96 ns without introducing deadtime in the level one trigger.

The level one trigger consists of nine different trigger systems, each based on the information from a single sub-detector. The output of these systems are called trigger elements, which are then combined in the central trigger logic to supply various subtriggers. Each subtrigger produces a level one keep signal which stops the pipelines and prepares the event to

be read out. The most important level one trigger elements are:

1) The TOF trigger, which uses the TOF counter signals to produce a powerful discrimination between 'in-time' interactions in the fiducial volume and 'out-of-time' interactions elsewhere. The TOF background trigger element is the most effective background rejection criterion and is therefore applied as a veto to many physics sub-triggers.

2) The z-vertex trigger, which uses the CIP, COP and the first forward MWPC to find sets of hits (called rays) consistent with the passage of a particle through the detector. The z origins of the rays are then examined to determine the position of the event vertex. Another important trigger element is z-vertex*t0, which indicates that there is at least one ray in the tracking (i.e. that there is some activity in the centre of the detector).

3) The forward ray trigger, which finds rays in the forward MWPCs and CIP.

4) The MWPC triggers, which includes the CIP trigger (used to provide triggers for taking cosmic muon data) and the BPC trigger (which looks for coincident hits in at least three out of four BPC layers). The CIP trigger may also be used to search for rays pointing mainly backwards which may indicate a proton-gas interaction upstream.

5) The big ray trigger, which looks for combinations of rays from z-vertex and forward ray triggers.

6) The CJC triggers, used principally to find rays in the CJC that have a distance of closest approach to the beam axis of less than 2 cm. Tracks with high and low transverse momentum can be distinguished. Topological requirements may be made on the rays, such as requiring two rays to be back-to-back in ϕ.

7) The z-chamber trigger, which uses CIZ and COZ to find rays and hence measure the position of the interaction vertex.

8) The liquid argon calorimeter trigger, which provides triggers based on transverse and total energy as well as allowing various topological signals to be identified using lookup tables.

9) BEMC Single Electron Trigger (BSET) which looks for an isolated electron in the BEMC.

10) The Instrumented Iron trigger, which looks for muons in the iron.

11) The forward muon trigger, which looks for muons in the forward muon spectrometer. The

operation of the trigger system for the forward muon system will be described in greater detail in chapter four.

12) Luminosity triggers, principally ETAG, which searches for an electron in the electron tagger and no photon in the photon tagger.

The level two trigger is used to decide quickly (within 20 μs) whether the event should be kept or rejected. Once a level two trigger keep signal has been produced, readout of the detector proceeds, extracting the data stored in the pipelines. The level two trigger includes topological and neural net triggers, but was not available for the Autumn 1992 run and so will not be discussed further. Similarly, the level three trigger, which runs on AM 29000 RISC processors, is able to assemble more information for a better trigger evaluation. This was also not installed for the Autumn 1992 run.

The level four trigger is a filter farm based on fast mips R3000 processor boards. It is integrated into the central data acquisition system and performs a cut-down version of the full event reconstruction online to allow a powerful discrimination on the basis of physics class. In the Autumn 1992 run, the filter farm was mainly used to reconstruct the event vertex from the CJC information and reject those events with a vertex outside the fiducial volume.

The H1 data acquisition system is shown schematically in figure 3.20. It is based mainly on the IEEE VMEbus standard [34]. Information is read out in parallel from each subdetector system before being combined into a single event record by the event builder. Data compression is carried out online to reduce the volume of data from 3 MBytes of raw data down to event sizes of between 50 KBytes and 100 KBytes. Fast data transmission is provided by a VMEtaxi optical bus. Control of the experiment is provided by several Macintosh computers in the H1 control room. These computers do not actually perform any of the data aquisition tasks, which are handled by processors in crates, but they do provide control of parameters and monitoring of the experiment.

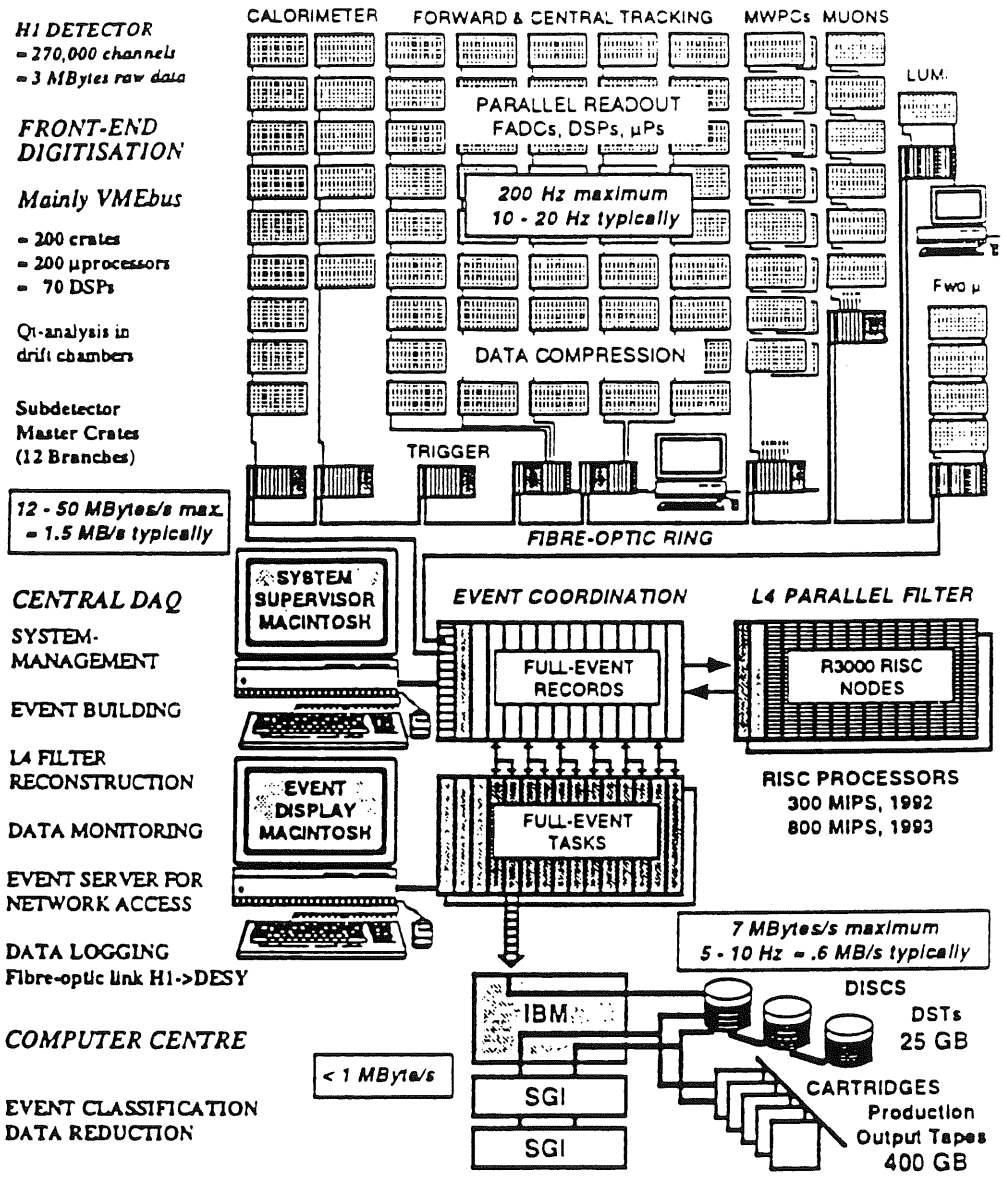

Figure3.20: The H1 data acquisition system.

The Data Processing System And Reconstruction Software

The data taken by H1 are stored on raw data tapes on the DESY IBM 9000/720 VF mainframe. This machine is used, together with a robot tape silo, to store, manage and export all of the experiment data (raw, reconstructed and simulated). The reconstruction program for H1, H1REC [35], runs offline on many platforms but the production reconstruction is done by a semi-online system consisting of three Silicon Graphics 4D/460 workstations with six processors each. This processing produces Production Output (POT) tapes from the raw data. A cut-down version of H1REC also runs on the level four trigger filter farm. Data analysis is carried out on the DESY IBM, on Hewlett-Packard workstations and on the Silicon Graphics machines. Data Summary Tapes (DSTs) consisting of event selected on the basis of physics class are exported to outside institutions for further analysis work.

H1 software is principally written in FORTRAN 77, with the exception of the QT analysis program H1QT [36] which is written in C as the code has to run on front-end processors as well as offline machines. The code is managed using the CMZ code manager [37]. Memory management is provided by the BOS package [38] with additional discipline provided by a data definition language [39]. All data are contained in BOS banks, which are tabular arrays of values and pointers to related rows in other tables. Steering through the relations of a bank is performed by DATMAN, a tool written for this purpose [40]. Machine-independent input-output is provided by the FPACK package [41].

All H1 software has been written in a modular fashion. A module is a self-contained set of routines that perform their own initialisation upon first call and thereafter operate on input BOS banks to produce output BOS banks. A module is not allowed to change its input banks, nor is a module allowed to change the output banks produced by a different module. A large program such as H1REC therefore consists solely of a number of module calls to each of the subdetector reconstruction systems. The operation of a module may be controlled by steering banks, a BOS bank with just one row that supplies parameters to the code when run. These banks are stored as text files and are read in at the start of a job, so that reconstruction parameters may be changed without re-compiling the code.

The calibration constants, geometry and run summary information are all stored in BOS banks. A purpose-written database MDB [42] holds all this information and provides mechanisms for marking the range of validity for different versions of a bank. The database also contains default version of steering banks. The database also allows update and inspection of the calibration constants.

The Simulation Software

The H1 simulation program H1SIM [43] is based on the GEANT package [44]. The geometry of the detector and beamline within 100 m of the interaction point has been implemented with two levels of granularity to allow faster simulation when maximum accuracy is not required. The granularity of each detector component is controlled by a steering bank, as is the information produced by each sub-detector volume. In addition, components may be switched off to allow detailed simulation of single detector components.

In order to provide accurate detector response simulation, especially with fine geometry, it is necessary to keep track of particles with kinetic energies as low as 1 MeV. This leads to a simulation time of 600 s for a typical deep inelastic scattering event on a Silicon Graphics 4D/460 processor. To help contain the CPU requirement, the tracking step (where all particles are tracked through the subdetector volumes and energy deposition recorded) is separated from the digitisation step which simulates the detector response to this energy. This allows limited re-processing for different calibration constant without repeating the tracking step. The trigger simulation step is also separated so it can be repeated without duplicating the digitisation step.

A fast parameterisation of energy showers in the calorimeters, H1FAST [45], was developed and implemented. This suffices for non-critical applications as the detailed shower profiles are not generated, saving a factor of 10 in CPU time. Finally, for relatively coarse work such as feasibility studies, an ultra-fast parameterised simulation program called H1PSI [46] was developed. This program has a simulation time of about 0.1 s on a Silicon Graphics 4D/460 processor.

The Physics Analysis Software

H1 has two physics analysis tools. The first of these is LOOK [38], a graphics package which provides histogramming functions and also provides a user-friendly, machine independent interface with the low-level graphics primitives used (currently GKS [47]). The LOOK system runs on many platforms, including the Macintosh computers that monitor data acquisition in the H1 control room. The H1 event display H1ED [48] is written within the LOOK framework and allows histogram analysis to be performed whilst scanning events. H1ED can also call any H1 modules, for example, to repeat the digitisation step of the current simulated event with a new set of calibration constants.

The second package for physics analysis is called H1PHAN [49]. This program is essentially a subroutine library that operates on four-vectors which are constructed by the H1PHAN program from the reconstruction output banks. H1PHAN includes a large number of standard routines such as Lorentz transformations, deep inelastic scattering kinematics and jet finding algorithms, allowing these to be maintained centrally and avoiding duplication of effort. The user of H1PHAN writes his own subroutines for physics analysis work which can call any of the standard routines. H1PHAN is usually used to produce histograms for interactive analysis in LOOK.

Chapter 4: The Forward Muon System.

Introduction

The H1 Forward Muon Spectrometer is designed to identify and measure the momentum of muons in the forward direction ($4° < \theta < 17°$). The system consists of six double planes of drift chambers and an iron toroid, as illustrated in figure 4.1. The detector hardware hierarchy is shown in figure 4.2.

The active detector area is split into two sections, before the toroid and after the toroid (before and after here are for a particle originating from the H1 vertex, i.e. travelling in the same direction as the proton beam). Each of these sections consists of three double layers of drift chambers, two with wires strung around the beam pipe and one with wires strung radially out from the beam pipe. A layer is also radially segmented into octants, each octant being mounted on its own octant frame.

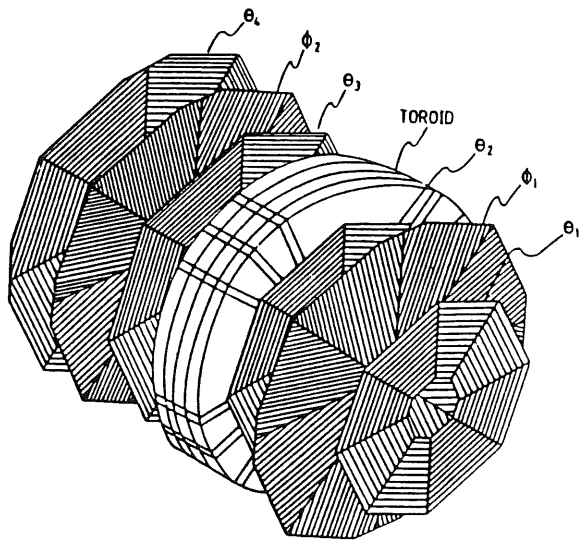

Figure 4.1: The forward muon spectrometer. From [30].

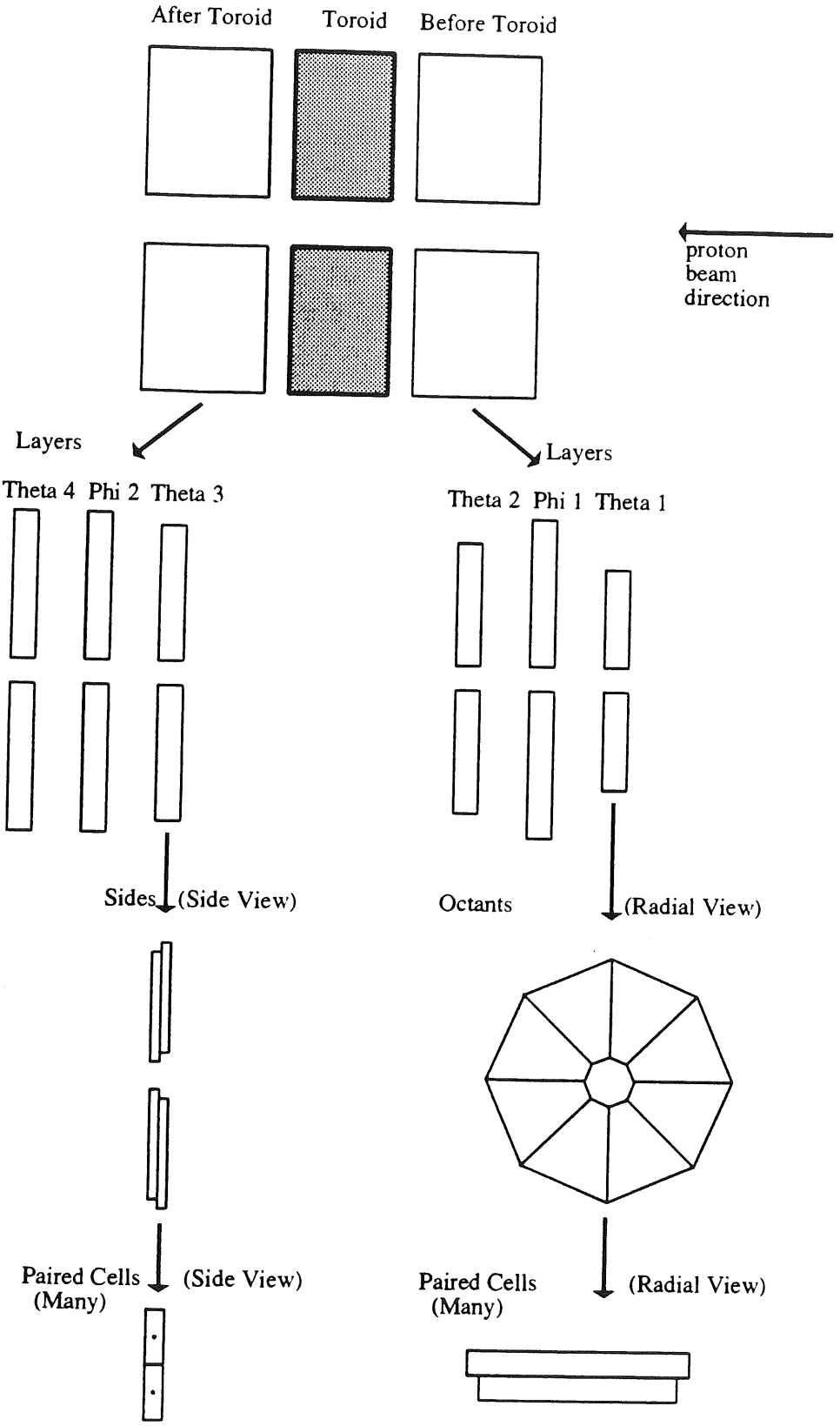

Figure 4.2: The forward muon system hardware hierarchy.

Within one side of an octant the cells are arranged into pairs, connected together using a 330 Ω resistor. This halves the amount of readout electronics required for the detector, at the expense of introducing more resistance into the system and hence creating greater pulse attenuation. The cells on each side of a layer are offset by half the width of a cell, allowing resolution of drift sign ambiguities and extraction of an independent T_{zero} by the forward muon trigger.

Principle Of Operation

The basic principles of operation of the forward muon system are show in figure 4.3. A charged particle passing through the system leaves a trail of ionised gas in the chambers through which it has passed, figure 4.3(a). An electric field is maintained in each cell so that the electrons produced by this ionisation drift toward the sense wire at the centre of the cell and the positive ions drift towards the cell walls. A potential difference is maintained between the sense wire and the drift voltage in the cell, such that when the ionisation electrons approach the wire they experience a strong radial field. This accelerates the electrons so that they can cause further ionisation in the gas near the wire, creating an avalanche of electrons and hence a larger signal, an effect known as gas amplification, figure 4.3(b).

These charges produce pulses on the sense wire which are then collected by the readout system. Analysis is done online to give information on the time taken for the first electrons to drift from the path of the particle to the wire and the integrated charge collected at the two wire ends, figures 4.3(c) to (k). This is referred to as Qt information.

In the offline reconstruction program, the Qt values are converted to space points, figures 4.3(l) and (m). As the drift time contains no information on which side of the sense wire the particle passed, there is an ambiguity in the sign of the drift co-ordinate. This ambiguity may be resolved by looking for a corresponding hit in the other side of the double layer. As the sides are offset by half a cell, two hits may line up to form a pair as shown in figure 4.3(n).

Once pairing has resolved the drift sign ambiguity, track segments before and after the toroid are formed by considering all possible combinations of pairs. The chi-squared (χ^2) method is used to assess quality of fits, as described later. The value of χ^2 for each straight line

fit is calculated and those pairs that satisfy a cut are accepted. The track segments before and after the toroid are then associated as possible track candidates, figures 4.3(o) and (p). A series of extrapolations is then carried out for each each track candidate assuming a range of momenta and a χ^2 calculated for each possibility, figures 4.3(q) to (u). The value of momentum giving a minimum for this χ^2 is then taken to be the momentum of the track (assuming that the minimum value of χ^2 is less than a cut). Reconstruction is now complete and other subdetector information may be linked to the forward muon information, but this linking will not be described further.

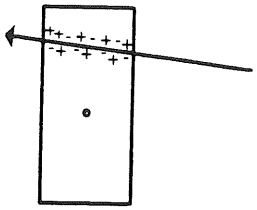

a) A charged particle passes through a cell producing a number of electron-ion pairs.

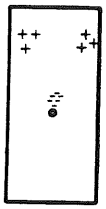

b) The electrons drift towards the wire, the ions drift (more slowly) towards the cell walls. Once the electrons get close to the wire, the strong radial field produces an avalanche.

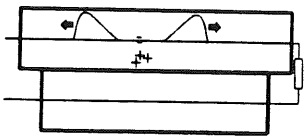

c) The avalanche produces a pulse in the wire which propagates in both directions along the sense wires of the two linked cells.

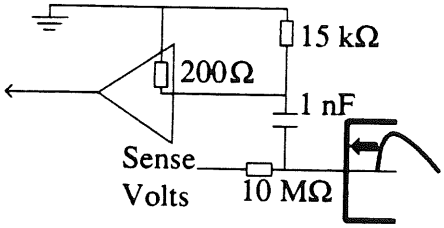

d) As the pulse propagates along the wire, the different frequencies travel at different velocities. The net result is that the leading edge steepens while the trailing edge becomes more spread out. The pulse reaches the pre-amplifiers at the end of the cells and is picked off the sense wire by a 1 nF capacitor.

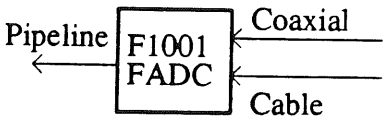

e) The preamplified pulses from both wire ends are fed through 50 m coaxial cables to an F1001 Flash Analogue to Digital Converter. Here, they are digitised into 9.6 ns bins and stored in a 256-bin pipeline.

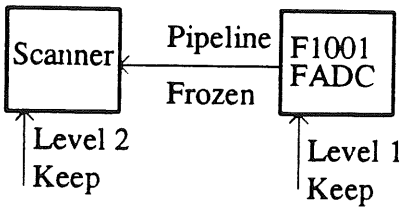

f) When a level one trigger keep signal is received, the FADC sampling is stopped, freezing the last 256 time bins in the pipeline. When a level two trigger keep signal is received, the scanner reads out the pipeline into its own buffer.

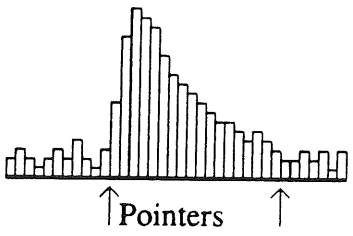

g) As the data are being read out, pulse height analysis is carried out upon the samples. Pointers are created to mark when the signal crosses a threshold value and remains above it for a number of bins. A second pointer is created for when it falls below threshold for a second number of bins.

Figure 4.3 (a-g): The stages of particle detection and reconstruction in the forward muon system. Stages d,e,f,g form the readout chain of the chambers.

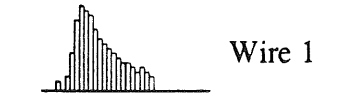

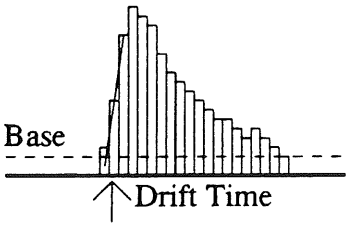

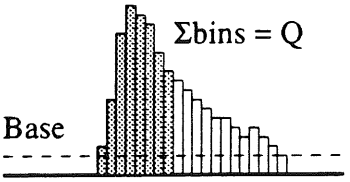

h) The signals from the two wire ends are compared. If pulses exist on both within a certain time of each other they are associated. If not, the pulse is retained but flagged as single-ended. This can occur when the hit is near the preamp of one wire end and thus the pulse on the other wire end is small.

i) Drift time extraction is performed. This is based on extrapolating the leading edge back to the background (or base) level, then taking the time to be a constant fraction along the leading edge from this time. An event T_{zero} is required from the central trigger to give the starting point for drift time.

j) Charge integration is performed. The signal is summed for eight time bins unless either associated pulse is less than 8 bins long in which case this shorter pulse length is used. The signal is corrected to start at the obtained drift time instead of the first channel in the pulse. Finally, the pedestal is subtracted.

MRTE	Chan	Q(1)	Q(2)	···
Hit 1				
Hit 2				
Hit 3				
...				

k) The event is assembled by the event builder and the Qt information is stored in the MRTE BOS-bank (MRPE for phi chambers). This is the end of the online processing and data aquisition chain.

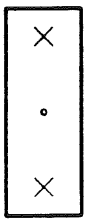

l) Offline, the drift time information is converted to a drift distance using the drift velocity and wire t_{zero} information. This gives a distance but not a direction, so the information has drift sign ambiguity. The drift distance errors are ≈250 μm.

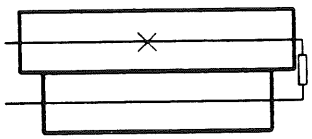

m) The charges on the two wire ends are used in the charge division algorithm (Q(1)-Q(2))/(Q(1)+Q(2)) to determine how far along the wire the hit occurred. Single ended hits are placed at the preamp end of the wire that gave the signal. Charge division errors are ≈1% of wire length, that is, of order of centimetres.

n) Pair finding is carried out on both sides of a layer. Hits are required to be within a certain distance of each other in drift and charge division co-ordinates to be paired. No vertex pointing is required. Hits not associated into pairs are retained but are flagged as being unpaired hits.

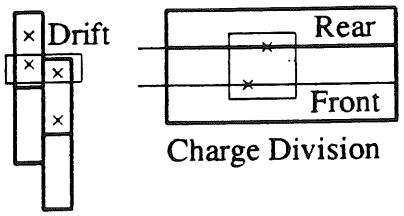

Figure 4.3 (h-n): The stages of particle detection and reconstruction in the forward muon system. h,i,j together form the Qt analysis which may be performed on the front end processor (as assumed here), on the level 4 filter farm or offline.

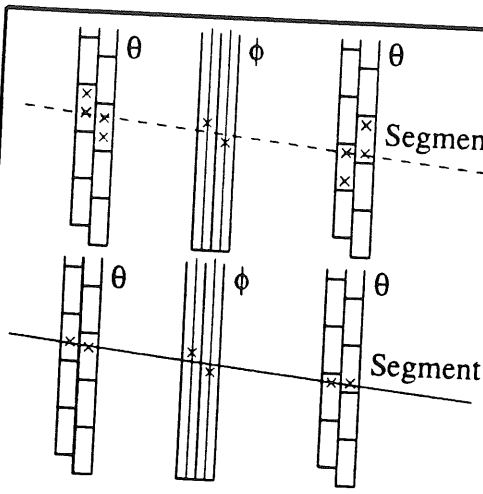

o) Track segments are formed from pairs. At least one pair is required in a theta layer, plus at least an unpaired hit in the other theta layer. Nearby hits in the phi chambers are associated with the segment.

p) The track segments are assessed on the basis of a χ^2 fit. Drift ambiguities are resolved at this stage. A single pair may be used in more than one segment, but no two segments may differ only in the drift sign ambiguity resolution of the component hits: the one with the lowest χ^2 is taken.

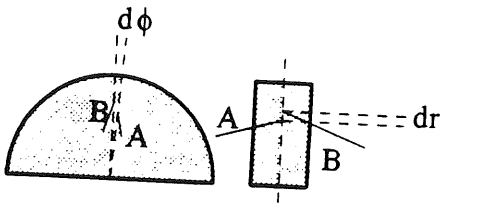

q) Track segments before and after the toroid are compared. For each segment after the toroid, a search is made for segments before the toroid that lie within a certain distance in the radial and phi co-ordinates, dr and dφ, defined at the central plane of the toroid.

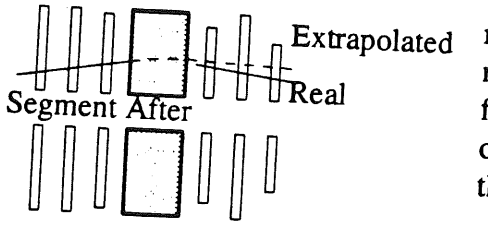

r) For each track candidate, a momentum determination is made by extrapolating from the segment after the toroid for several values of momentum. A χ^2 is calculated based on the difference between the extrapolated segment and the actual segment.

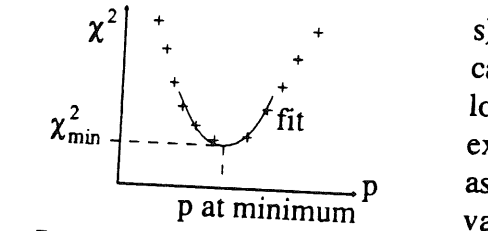

s) The minimum value of the χ^2 for the track candidate is calculated by fitting a quadratic to the points around the lowest value found in the scan. If this minimum value exceeds a cut, the candidate is rejected. The track is assigned the momentum corresponding to this minimum value.

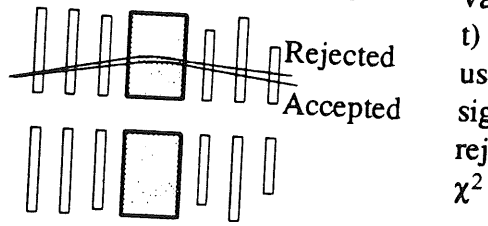

t) All tracks are compared to ensure that no hit has been used more than once. Segments may be formed with both signs of drift ambiguity, and these duplicates are now rejected so that only the candidate with the lowest track χ^2 remains.

MTKR	1/p	Theta	Phi	...
Track1				
Track2				
Track3				
...				

u) The final track information is stored in the MTKR BOS bank and written to the output stream. Forward muon reconstruction is now complete. Other software modules may now attempt to link the MTKR tracks with tracks elsewhere in the detector.

Figure 4.3 (o-u): The stages of particle detection and reconstruction on the forward muon system.

The Drift Cells

Figure 4.4 shows a cross section through four forward muon drift cells mounted on an aluminium octant frame. The cells are built from two planes of printed circuit board (PCB). These boards are coated on both sides with copper: the outer surface is kept at ground to screen the cell whereas the inner board has been machined to form 19 copper strips, 4mm wide with 2mm gaps except for the first and last strips which are thinner to partially compensate for edge effects. These two layers of PCB are held 2.0 cm apart by 0.7mm thick aluminium extruded side profiles, again held at ground. The strips on the interior of the cell are connected via 230 MΩ metal film resistor chain to the drift high voltage power supply to produce the drift field in the cell. The nominal drift voltage is 3 kV, producing an average drift field of 0.45 kV cm^{-1}.

Along the long axis of each cell runs a Nichrome sense wire, 20 μm in radius for the short inner cells and 25 μm for the longer outer cells. Wires more than 1.5 m long have a support at the mid-point of the cell. The wire is kept at positive high voltage, notionally 4.5 kV, which ensures a potential difference of 1.5 kV between the centre of the drift field and the wire. This potential difference produces a radial field around the wire which is responsible for the gas amplification of the primary pulses.

The cell endcaps are made of moulded Noryl with a precise dowel hole for fixing the cell to the octant frame with a precision of 50 μm in the drift direction and 1 mm in the other directions. Both endcaps contain wire crimps to hold the sense wire and holes for the gas supply to the chambers. One endcap also contains the resistor chain, high voltage connectors for the drift voltage and sense voltage and the sense wire readout, which is decoupled from the DC sense voltage supply by a 1 nF ceramic disk capacitor. The other endcap contains a sense wire connection via a 330 Ω resistor to the sense wire of the adjacent cell.

The connection between two cells forms a readout pair. Ideally, both ends of each wire would be read out to obtain the charges at the two wire ends for charge division. However, connecting two cells together allows the detector to be read out using only half the number of channels.

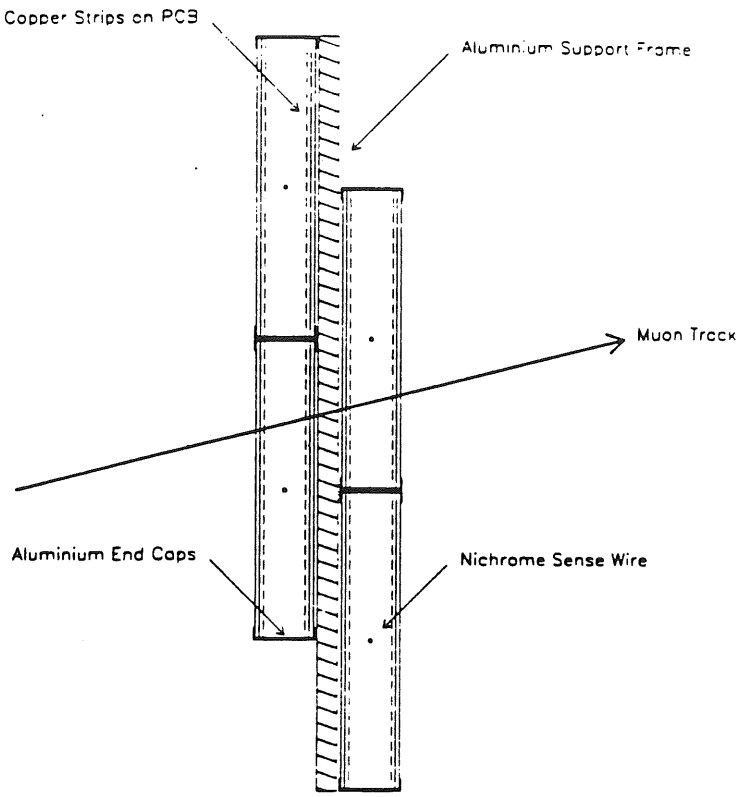

Figure 4.4: Cross-section of forward muon drift cells mounted on an octant frame. From [50].

Greater pulse attenuation is introduced when using pairs linked by a resistor as the pulse has to travel through a greater length of wire. This can be a problem when the hit is close to one of the preamplifiers as the pulse on the far wire end may be so attenuated that it cannot be resolved from the pedestal. Such hits, with a large pulse on one wire end and no pulse on the other wire end, are called single-ended hits.

The Gas System

The chamber gas is supplied from a recirculator in the main H1 gas room. The gas mix used in Autumn 1992 was 92.5% Argon, 5.0% Carbon Dioxide and 2.5% Methane. The composition of the mixture is optimised to satisfy several criteria. The signal produced in the chambers originally comes from ionisation produced by the passage of a charged particle so one requirement of the gas is that it should be easy to ionise, such as a noble gas. A quenching agent is added to prevent the gas from breaking down and discharging continuously.

The drift velocity of the gas is dependant primarily on the gas mixture, the applied electric field (E) and the pressure (p). The dependence on other parameters, such as temperature and applied magnetic field, is comparatively weak. Figure 4.5 shows the variation in drift voltage versus electric field over gas pressure. The region where the drift velocity only varies slowly with changes in E/p is called the plateau. It is advantageous to operate in this region because minor variations in E or p will not affect the drift velocity significantly.

The drift velocity of the gas must be chosen as a compromise between two conflicting requirements. First, the time resolution of the system is roughly constant as the shape of the pulses produced does not depend strongly on the drift velocity. This means that a long drift time and hence a low drift velocity is desirable to achieve high spatial precision. The second requirement is that the chamber signal must be delivered in a short enough time for the forward muon trigger to be able to produce a decision. The nominal drift velocity of the final gas mix is 4.5 cm/μs.

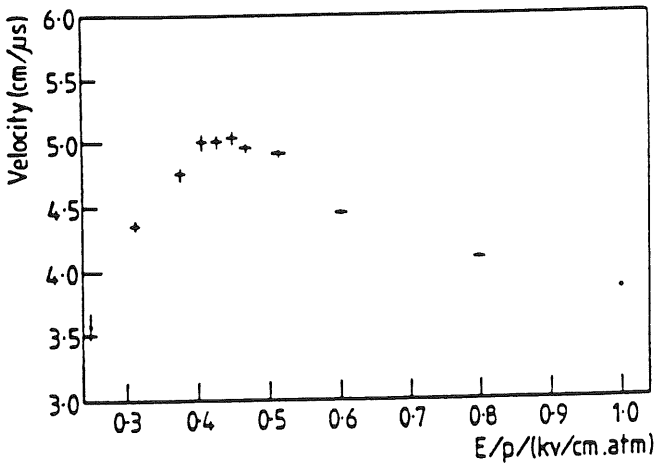

Figure 4.5: Graph of the drift velocity versus E/p for the final Ar:CO_2:CH_4 gas mixture. From [30].

Readout Electronics

On reaching the wire, the electrons produce a pulse which then travels down the wire in both directions. The pulses at the wire ends are picked off the sense wire by a 1 nF capacitor and are then preamplified. These preamplified pulses are then digitised by F1001 Flash Analogue-to-Digital converters. The F1001 FADCs are clocked at 104 MHz, ten times the HERA clock frequency, and have a resolution of eight bits with a non-linear response, giving an eight bit resolution for small pulses with a 10 bit dynamic range. The result of the digitisation is fed into a 256 time bin pipeline (actually a 256 byte memory used as a circular buffer) where it is stored until a level one trigger signal is received or 256 clock signals have arrived, in which case it falls off the end of the pipeline. Up to 16 FADCs are present in each crate, plus a scanner unit and a front-end processor (described below) and other control cards which will not be discussed further.

Once a level one trigger keep signal is received, the sampling is frozen. If a level two trigger keep is received, the pipeline is read out by an M1070 scanner which analyses the pulses for hits crossing threshold and performs zero suppression on the signal. If a level two reject is received, the pipeline is unfrozen and sampling begins again.

When a level three trigger keep is received, the scanner sends an interrupt to the FIC 8231 front end processor in the crate. This processor now reads the hit pointer information created by the scanner and assembles the raw data into offline format raw data banks, called MRTD (for the theta chambers) and MRPD (for the phi chambers) banks. These banks contain the pulses identified by the scanner plus several (currently six) time-bins before the pulse start to allow dynamic pedestal subtraction. An intelligent decision is also made for the case when two hits occur close together on the same wire; if the tail of the first pulse might influence the second pulse, all bins are kept.

Hardware Organisation

The theta layers are constructed by mounting cells onto aluminium octant frames. All octant frames are identical, but not all cell positions are populated in a given layer. An octant of theta layer one has 12 cells on each side, starting at the lowest cell position. Theta two octants have 14 cells per side starting from the lowest position. Theta three octants have 18 cells per side but the lowest position is not filled. Theta four octants have 20 cells per side and again the lowest position is not filled. This gives a total of 1024 theta cells. The top right corner of the octant frames are truncated or 'cutoff' to allow the frames to fit into the H1 experiment hall.

All of the octants in a given theta layer are identical. However, in order to fit the frames into the H1 hall, alternate frames must be 'flipped' so that the cutoff corners lie at top, bottom, left and right, as shown in figure 4.6. In order to allow the chambers to fit together without gaps, a small overlap is provided at octant boundaries and so each octant is offset from its neighbour in z. Hence, the arrangement is two Maltese crosses, shown in figure 4.6, where the octants mounted in nearest H1 are marked '+', those further from H1 with '-'. The octants are mounted on each side of aluminium door frames with each door frame holding 2 octants and forming a quadrant. The four door frames are mounted on an iron layer frame. The door frames may be retracted to allow access to the beam line.

It was envisaged that the environment near the beam line might prove too hostile for the chambers to be operated safely. Hence, the inner six cells on each octant side have their own voltage control, independent of the outer cells, so that they may be turned off if necessary. As the phi chambers are radial, the long cells that extend to near the beam pipe are mounted on a movable frame called a slider. This arrangement is shown in figure 4.7 where the cells mounted on the slider are shaded grey. The sliders are mounted on the front of the octant frame, giving three 'sides' to a phi octant.

Phi layer 1 has 27 cells mounted on each octant, with the two left-most and two right-most positions on each side of the octant not filled. Phi layer 2 has 35 cells mounted on each octant. The odd number of cells per octant leaves one cell that has to be read out at both ends. This is referred to as an unlinked cell. This gives a total of 496 phi cells but 512 readout

channels, and 1520 cells in the whole system.

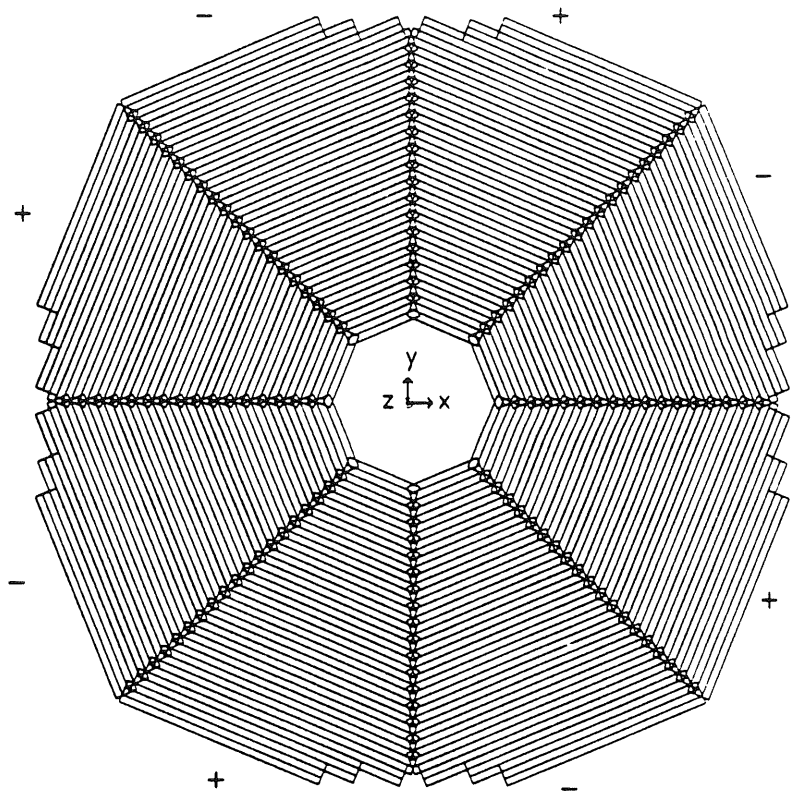

Figure 4.6: Theta layer four, showing cutoff orientation. Octants marked '+' are nearer H1, those marked '-' are further from H1.

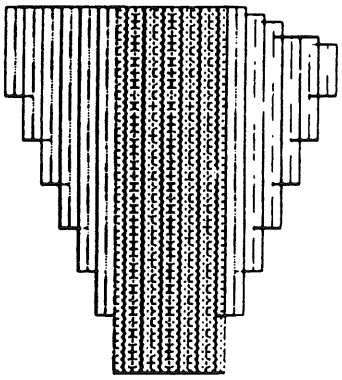

Figure 4.7: A single phi octant. Shaded cells are on the slider. From [50].

The Toroid

The toroid is composed of two movable halves, each of which is composed of four semi-circular sections. The assembled halves are held together by iron bolts. The toroid may be opened to allow access to the beam line. The current is supplied by twelve rectangular coils, each of which is composed of fifteen turns of copper tubing, 11.5 mm square, with an 8.5 mm square hole through which cooling water flows. The assembled toroid is 1.2 m thick, with an inner radius of 0.65 m and an outer radius of 2.90 m. The nominal current in the coils is −150 Amps. The toroid is held together by six bolts.

The field is monitored by observing the change in flux as the magnet is switched on and off in 9 wire coils threaded through holes in the iron, producing a radial map of the field. There is a distortion where one of the coils includes a bolt as the bolt does not make good magnetic contact with the rest of the toroid. This is thought to distort the field in the adjacent coils as well. Figure 4.8 shows the position of the monitoring coils in the toroid.

The parameterisation used for the toroid magnetic field is

$$B_\phi = \frac{B_0}{r^{0.0932}}$$

where B_ϕ is the ϕ-component of the magnetic field in Tesla, r is the radial distance from the beam axis and B_0 is a current dependent constant. The radial and z-components of the field are assumed to be zero, and the field outside the toroid is also assumed to be zero. B_0 is related to the current in the coils, I, in Amperes, by the parameterisation

$$B_0 = \sum_{j=1}^{6} c_j \left(\frac{|I|}{100 \text{ Amps}} \right)^{j-1}$$

where the constants c_i are given by (from [52]):

$c_1 = +0.95918$ T $c_2 = +0.13198$ T $c_3 = -0.11112$ T

$c_4 = +0.52165$ T $c_5 = -0.12564$ T $c_6 = +0.12219$ T

The above parameterisation applies for a negative current in the toroid, and the field

produced is such that positively charged muons are de-focussed by the field. For positive currents, the value of B_0 is negated so positive muons are focussed by the field. Figure 4.9(a) shows the parameterisation of B_0. Figure 4.9(b) shows the measured and parameterised field for various values of the current in the coil. The penultimate point (at approximately 2.5 metres) is the coil containing one of the six bolts and this point and the points on either side are not used in the parameter fitting. It may clearly be seen from the figure that the parameterisation is not valid for $|I|<100$ Amps. The nominal operating current is -150 Amps and it is not foreseen to take physics data with a reduced current except for alignment data taken with zero magnetic field.

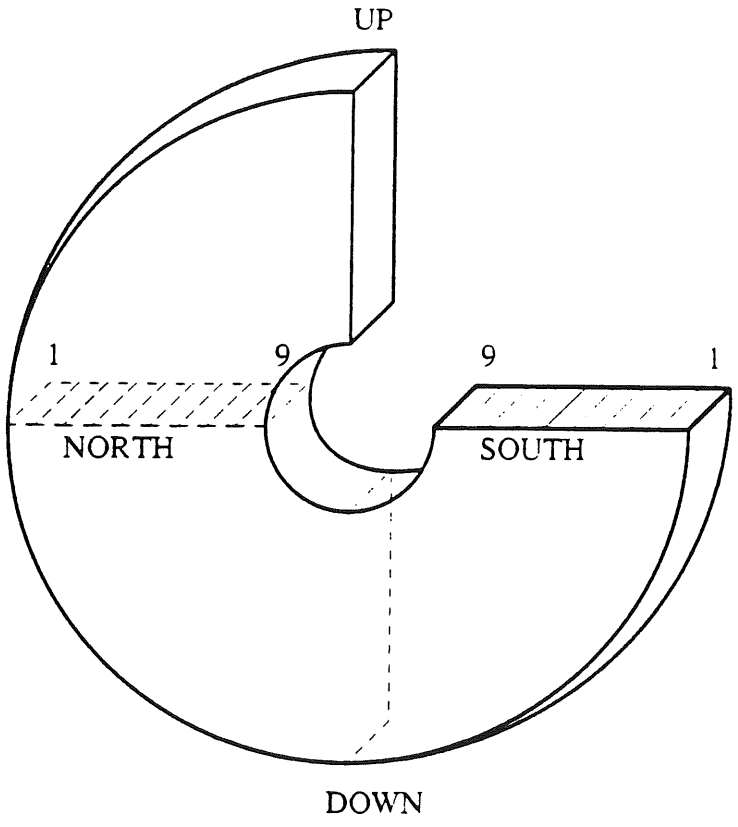

Figure 4.8: The forward muon toroid showing the position of the monitoring coils. The field strengths are measured in two sets (North and South) each of nine coils. There are also two large coils (Up and Down).

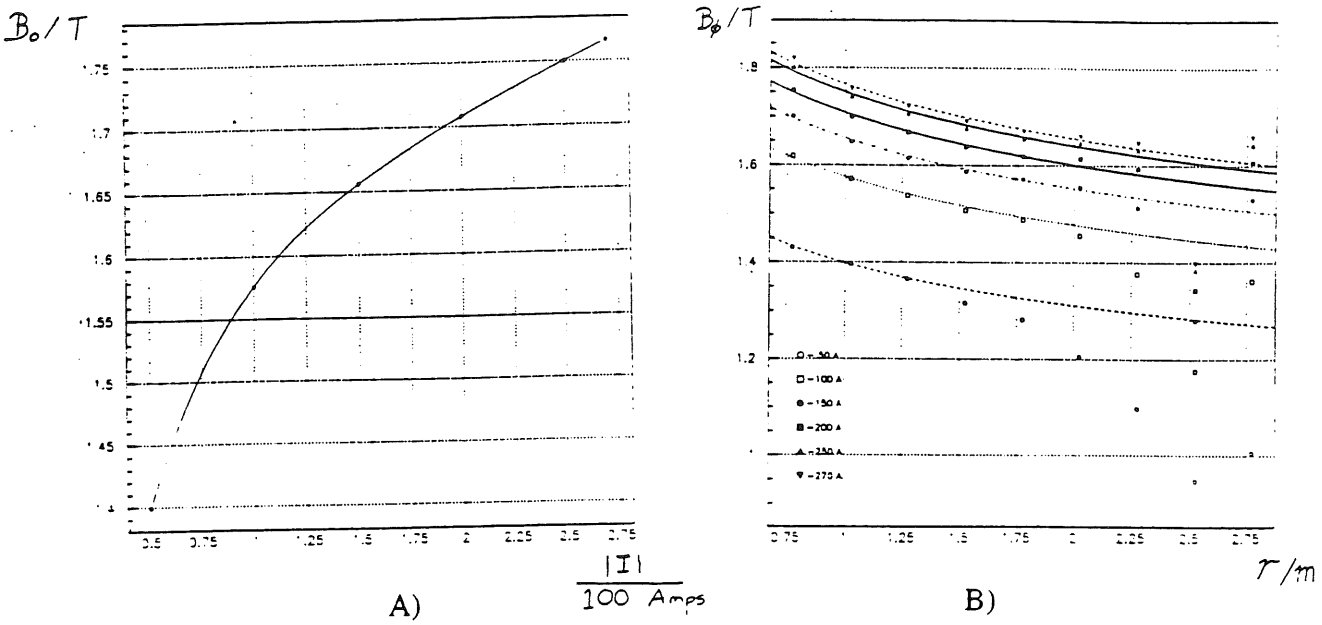

Figure 4.9: Parameterisation of the magnetic field in the toroid. a) B_0, b) field strength. From [52].

Qt Analysis

The purpose of the Qt analysis is to extract the drift time, t, (the time taken by the first electron in the ionisation droplet to drift from its original position to the wire) and the charge integrals for the leading edges of the two pulses, Q(1) and Q(2). This analysis may be performed by the front-end processor, by the level four filter farm or offline. A full description of the Qt algorithm may be found in [53].

The drift time determination uses a leading edge algorithm, as shown in figure 4.10. First, the background level LBASE is calculated by taking the average level of the pre-samples taken before the pulse. Then, for each pulse, the maximum difference in pulse height between successive samplings in the rising edge is identified. This difference is called MAXDOS. The centre of the second of the two samplings involved is labelled IMAXDOS, and a line of slope $MAXDOS^{-1}$ is drawn from IMAXDOS back to the background level LBASE. This point is

labelled A. The drift time is then taken to be a fraction K (currently 1/3) of the distance from point A to IMAXDOS.

The determination of the charge integrals, Q, of the two pulses must be carefully optimised because the charge collected at each wire end is not exactly proportional to the resistance between the struck point and the preamplifier. The pulses that travel from the struck point are initially identical and the connection is a dispersive transmission line rather than a simple resistance.

The signal in the first eight bins of each pulse are summed unless the pulse on either wire end is less than eight bins in length. In this case the sum is taken over the length of the shorter pulse. The summation is then corrected to begin at the drift time calculated above rather than at the edge of the first bin of the hit. The background integral is then subtracted using LBASE as calculated above. A detailed study of this algorithm may be found in [54].

The end result of this analysis is the MRTE (theta chambers) and MRPE (phi chambers) banks which contains the Qt hit information which is the starting point for the forward muon reconstruction.

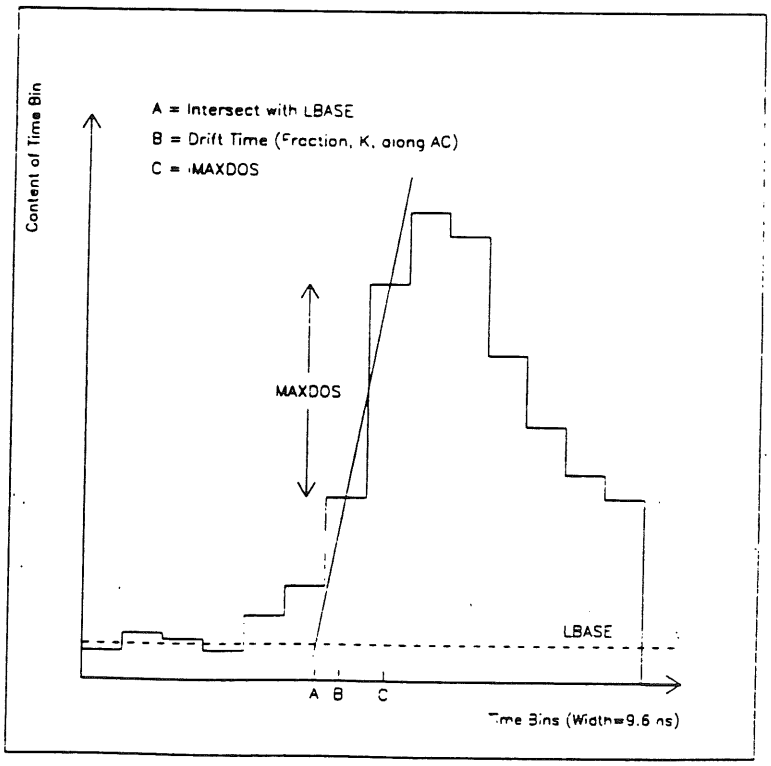

Figure 4.10: The leading edge algorithm for finding the drift time from the raw pulse data. From [50].

The Forward Muon Reconstruction Code

With the determination of the Qt values, the online data acquisition ceases and all further analysis is carried out offline. This analysis is carried out in the framework of the main H1 reconstruction program, H1REC [35]. The H1 software is written in a modular fashion (as described in [55]) so that the code for each subdetector may be run independently. The module that performs the forward muon reconstruction is called MTREC. A complete technical description of this code may be found in [52].

Qt to Space Point Conversion

1) Drift Co-ordinate

The drift time delivered by the Qt algorithm is relative to the global event T_{zero} as determined by the trigger. It is necessary to correct for various delays in the system before converting to a drift distance by multiplying by the drift velocity. Hence, the expression used is

$$x_{drift} = v_{drift}(t_{drift} - t_{zero} - t_{jitter} - t_{tof})$$

where x_{drift} is the drift distance, v_{drift} is the drift velocity, t_{drift} is the drift time as given by the Qt analysis. The corrections are

1) t_{zero} , a global offset determined by the minimum drift time of a reference cell.

2) t_{jitter} , a wire by wire offset relative to the global t_{zero} , measured using test pulses.

3) t_{tof} , a correction based on the time of flight, the time taken for a photon to travel from the front plane of the detector to the plane of the hit.

For Monte Carlo, all three corrections are set to zero. The determination of these constants and the drift velocity for data will be discussed in a later section. Several assumptions are made in order to be able to use the above formula:

1) That the drift time to drift distance relationship is linear, or equivalently that the drift velocity is a constant across the cell. Studies [51] have shown that this approximation is not

valid unless the operating voltage of the chambers is chosen carefully.

2) That the electron that arrives first at the wire corresponds to the central plane of the cell. This may not the case for angled tracks, where the electron closest to the wire does not come from the central plane. This is further complicated by the change over from a relatively uniform drift field to a radial field near the wire. Ideally, what is needed is an *Isochrone Map* of the cell. An Isochrone is a line of constant drift time to the wire. This analysis is in progress. However, for the current level of understanding of the chambers, the above determination of the drift distance is sufficient.

3) That all cells have similar drift characteristics. This is expected to be the case as the cells differ in length, not cross section. Minor differences such as propagation times down the wire are included in the t_{jitter} correction.

The drift distance obtained by the above procedure corresponds to a distance from the wire of the struck cell, but no information is given on the sign of this drift. Therefore, the drift distance is added to and subtracted from the co-ordinate of the wire to give two ambiguous solutions. The error on each point is not calculable from the data directly and so is given to the program as a single value worked out by offline analysis, as described later. The design value for the drift co-ordinate resolution is 250 μm.

2) Charge Division Co-ordinate

The charge division co-ordinate is worked out by considering the resistance to ground seen by the pulses heading towards each wire end. Consider a hit as shown in figure 4.11, a distance x along the wire from the nearest preamp. The resistance seen by the pulse from cell 1 is

$$R_1 = R_{preamp} + R_x$$

where R_{preamp} is the input resistance of the preamplifier (in fact, the mean of the two resistances as this is all that can be measured) and R_x is the resistance between the preamplifier and the hit. The resistance seen by the pulse from cell 2 is then

$$R_{tot} - R_l = R_{preamp} + R_{wire1} + R_{link} + R_{wire2} - R_x$$

where R_{tot} is the total resistance of the pair given by

$$R_{tot} = R_{wire1} + R_{link} + R_{wire2} + 2R_{preamp}$$

R_{wire1} and R_{wire2} are the resistances of the two wires and R_{link} is the resistance of the link resistor. The fraction of the total resistance between the hit and the resistive centre of the system is given by the charge division ratio

$$Q_R = \frac{Q_1 - Q_2}{Q_1 + Q_2}$$

where Q_1 and Q_2 are the charges at the two wire ends. However, it is possible that the two preamplifiers have different gains, so this expression must be corrected by including the gain ratio, G, giving

$$Q_R = \frac{1 - G\frac{Q_1}{Q_2}}{1 + G\frac{Q_1}{Q_2}}$$

The resistance between the hit and the resistive centre is given by

$$\frac{R_{tot}}{2} - R_l - R_{preamp}$$

and hence R_l is given by

$$R_l = \frac{R_{tot}}{2} - Q_R\left(\frac{R_{tot}}{2}\right)\left(\frac{L_{effective}}{L}\right) - R_{preamp}$$

where $(L_{effective} / L)$ is a measurable correction factor included for compatibility with the central tracker analysis only. It is equal to unity for the forward muon system at the present level of

understanding.

Having calculated R_l in this fashion, x, the distance of the hit from the preamplifier end of the struck cell, is given by

$$x = R_l \left(\frac{L_{wire1}}{R_{wire1}} \right)$$

where L_{wire1} is the length of wire in cell 1. This is then added to the co-ordinate of the preamplifier end of the cell to give the charge division co-ordinate.

As for the drift co-ordinate, the error on the charge division co-ordinate is not calculable directly from the data. The error varies with the length of the wire and is thus given as a fraction of the total wire length (length of wire in cell 1 plus length of wire in cell 2 plus the length of wire equivalent to the link resistor). Single-ended hits (with one charge value of zero) are placed at the preamplifier end of the struck cell with an error of 5% of the wire length. The design resolution is 1% of total wire length.

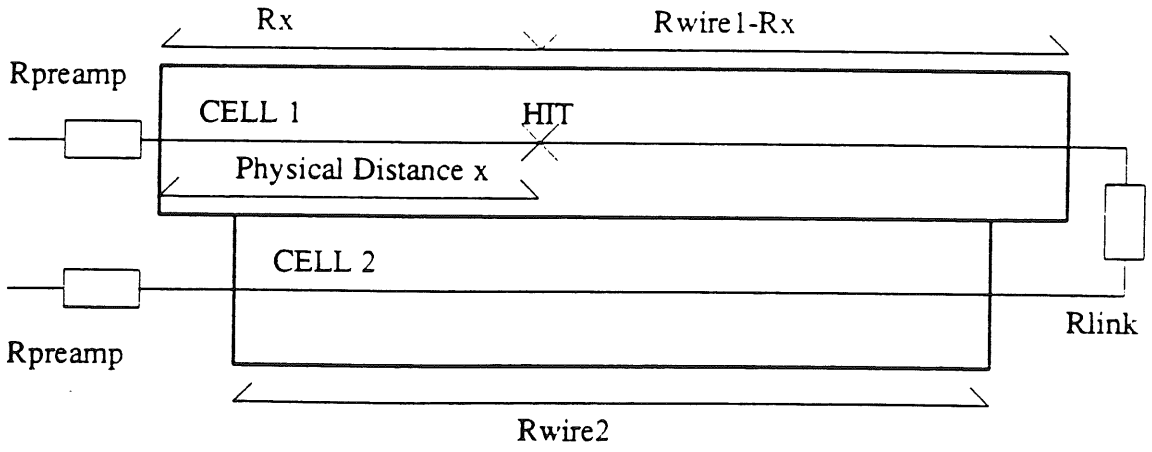

Figure 4.11 : Resistance division in a hit pair. The hit is a distance x along the wire from the nearest preamplifier.

The Pairing Algorithm

The pair finding algorithm attempts to associate hits on each side of a double layer. Only hits within one octant of the double layer are considered. Although there is some overlap between octants, this does not affect the pair finding significantly as a pair would be found in both octants and the best fit of these used in segment finding. As the overlap between octants is small, only a small fraction of events would have better information by including these extra pairs.

For each hit in the octant and layer, a search is performed for hits in the other side of the layer which lie within a distance δx (nominally 15.0 cm) in the charge-division co-ordinate and δy_l (nominally 5.0 cm) in the drift co-ordinate. Single-ended hits may be discarded or accepted by the pairing routine based upon a user-supplied parameter. The co-ordinate system used is local to the octant with y radially outwards, z along the H1 z axis and x defined so as to make a right-handed co-ordinate system. The origin of the co-ordinate system is the nominal beam position in x,y and the centre of the octant frame in z. This co-ordinate system is the natural one for the task, as it does not introduce any mixing between drift and charge division co-ordinates.

The cut in drift distance ensures that the segments found will be flat, that is, below a certain theta angle given by $\tan^{-1}(\delta y_l/\delta z)$ at the centre of the cell, where δz =3.42 cm, the separation between wire planes. Thus track segments with theta angle greater than $\approx 56°$ will not be recognised at the pairing stage. This is to reduce combinatoric problems as in principle all possible combinations of drift sign resolution are valid so long as the track is steep enough. Tracks from the H1 vertex should emerge from the iron with $\theta<20°$, but segments after the toroid may be steeper than this due to bending in the magnetic field and multiple Coulomb scattering in the iron toroid.

Any pair satisfying the above cuts will be considered, but it is possible that more than one resolution of the drift sign ambiguity satisfies the cut for any given pair. An example of this is shown in figure 4.12 where the hit is close to the wire in the left hand side of the layer. In order to reduce this effect, a second pass is performed to reject some of the steeper candidates. If the difference in y is greater than a second cut, δy_r,(nominally 1.5 cm) and there is another

candidate with a smaller y difference, only the candidate with the smaller δy is taken. In the case of figure 4.12, both candidates would be accepted as both are within the tighter y cut.

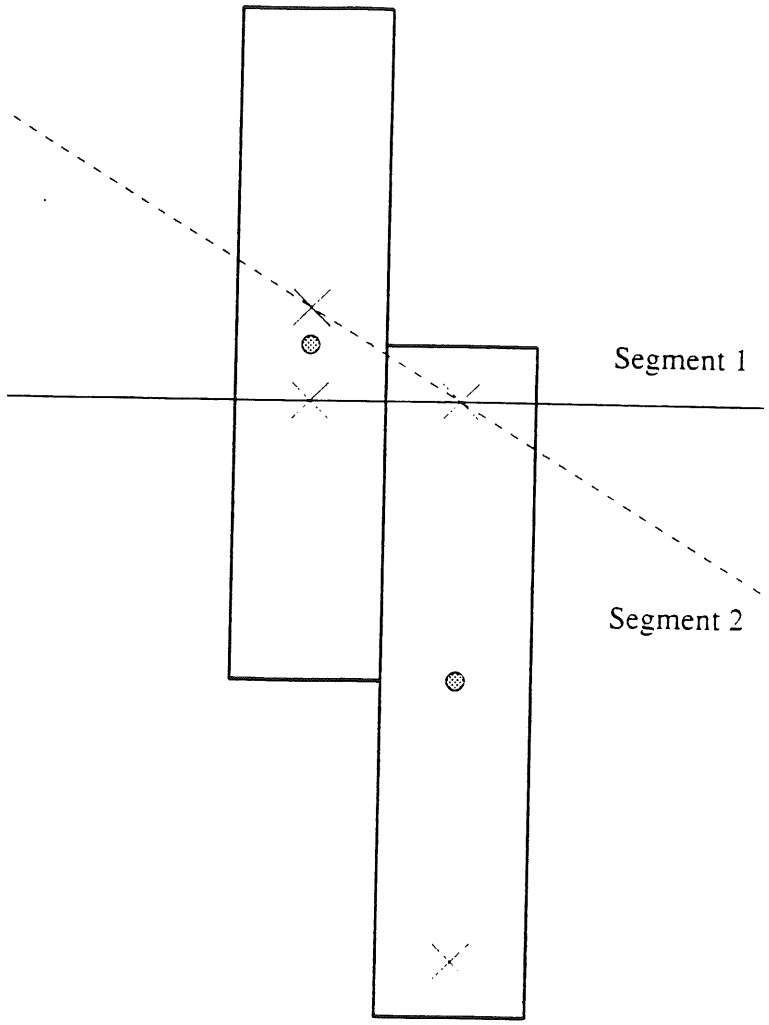

Figure 4.12: Multiple pairing possibilities. The drift resolution in the right hand cell is obvious, but it is not clear which solution to choose for the left hand cell as segment 1 and segment 2 are both valid possibilities.

The above scheme is also suitable for finding beam halo tracks, that is, real muon tracks that come in time with the proton beam and form a halo around the beam. These tracks, which are almost horizontal ($\theta \approx 0°$), are very useful for alignment and calibration studies. However, the scheme is not suitable for cosmic muon tracks, which are usually steep. In order to be able to reconstruct cosmics, the y cuts must be opened up to $\delta y_t = \delta y_f = 10.0$ cm to allow steep segments to

be found.

Pair finding in the phi chambers is complicated somewhat by the sliders, which mean that the phi layers effectively have three 'sides'. A search for pairs is therefore made in sides 1 and 2, 1 and 3 and finally 2 and 3.

The Segment Finding Algorithm

The segment finding algorithm relies on finding a segment between two theta layers and then associates any information from the intervening phi layer afterwards. The reason for this is historical: initially, only the theta layers were installed. All 1992 H1 data were taken with the theta layers only. The phi layers were installed in the 1992-1993 shutdown and are now fully operational. In principle, a more complex pattern recognition algorithm could be used to pick out tracks by requiring a certain number of hits along a straight line, regardless of whether they lie in theta or phi chambers. However, a good θ measurement is necessary for accurate momentum determination so any segments found without at least three theta hits are not useful. The straight-forward algorithm used provides this minimum of three theta hits.

The search proceeds by looping over all theta pairs and trying to find a hit, paired or unpaired, in the other theta layer (i.e. for a pair in theta one, search in theta two) in the same or one of the adjacent octants.

For each hit combination, the ϕ co-ordinate and error in phi of each pair is worked out. From this, the difference in ϕ co-ordinates of the two pairs, $\delta\phi$, and the error on that difference, $\Delta\delta\phi$, are worked out. The error on the ϕ difference is required to be less than a a cut E_{seh}, nominally 5.0 degrees, which ensures that the segment is reasonably well defined. This is mainly to exclude segments made solely with single-ended hits, which have a large error on the charge division co-ordinate. A test is also made to ensure that the segment is roughly radial by insisting that the ratio $\delta\phi/\Delta\delta\phi$ be less than a cut, nominally 10.0. This ensures that the pairs are close to each other in ϕ within errors.

For all segments passing these criteria, a straight line fit is made in x-z (charge division) and y-z (drift). The quality of the fit is assessed by the chi-squared method [59]. Given a set of

values, y_i, measured at a set of points, x_i and a functional form of $y=f(x)$, χ^2 is given by

$$\chi^2 = \sum_i \sum_j \left(y_i - f(x_i)\right) V^{-1}_{ij} \left(y_j - f(x_j)\right)$$

where V^{-1}_{ij} are the elements of the inverse of the covariance matrix V. In the simple case where the measurements are independent, V and V^{-1} are diagonal and the expression reduces to

$$\chi^2 = \sum_i \frac{\left(y_i - f(x_i)\right)^2}{\sigma_i^2}$$

where σ_i are the estimated errors on the measurements y_i.

The χ^2 values from the the two fits are added together to give the total value of χ^2 for the segment. The hits are all transformed to the local co-ordinates of the original pair before fitting but full covariance information is preserved. If the χ^2 is less than a cut value χ^2_{max} (nominally 100.0) multiplied by the number of hits on the segment, the segment is accepted.

A loop is then made to check for using hits twice with different drift ambiguity. All segments with χ^2 less than a cut (nominally 10.0) are kept. Segments which share the same hits but have χ^2 greater than this cut are compared. If the χ^2 of the worse fitted segment is at least a factor (nominally 4.0) greater than the better segment, it is rejected.

Once segments have been found using the theta information, the segment is extrapolated to the plane of the phi layer in between the two theta chambers. The same procedure as used above is now used to associate phi hits to the segment, with $\delta\phi$ being the difference between the extrapolated segment ϕ-coordinate and the ϕ-coordinate of the phi chamber pair. If this satisfies cuts, the x-z and y-z fits are re-done including the phi hits, and a new χ^2 formed. If this χ^2 is less than χ^2_{max} multiplied by the new number of hits, the segment is accepted. If more than one phi pair satisfies the association criteria, only the combination with the lowest χ^2 is accepted. If no phi pair was associated or the combinations had too high a χ^2, the theta segment is output as found in the earlier stage.

Track Finding And Momentum Determination

To find tracks, all segments are first extended in a straight line to the centre of the toroid. A search is then made for segments on the other side of the toroid whose intersection with this plane lie within a difference in radius δr (nominally 20.0 cm) and a difference in the phi co-ordinate of $\delta\phi$ (nominally 30.0°). The code checks to see whether there are more segments before or after the toroid in order to decide whether to extrapolate from before the toroid to after the toroid or vice versa. If there are more segments before the toroid only the segments after the toroid will be extrapolated. This is normally the case for real data where particles have been sprayed up into the detector from the beamline magnets and sail-through and punch-through from the instrumented iron is significant. This is the case that will be discussed, although both cases are implemented in the code.

The extrapolation proceeds by tracking the segment back to the face of the toroid, then extrapolating through the toroid in small steps (normally 15 steps are used). This extrapolation is done for a range of candidate momenta from 2.25 GeV to 1000.0 GeV and for both muon charges. As there is no sensitive volume in the toroid for tracking particles, it is necessary to evaluate where a muon of given charge and momentum will emerge from the toroid on average and calculate the expected deviation from the average position due to multiple scattering. This is then compared with the segment on the other side of the toroid. The deviation in angle, $\delta\theta$, caused by a magnetic field of field strength B Tesla is

$$\delta\theta = \frac{0.003\ B\ \delta l}{p}$$

where p is the muon momentum in GeV/c and δl is the distance travelled in the field in cm. In extrapolating through the toroid the radial and z-components of the magnetic field are taken to be zero and it is assumed that the field is zero outside the iron.

The muon momentum is recalculated for each step in the extrapolation to take account of the energy lost in traversing the iron [56]. The energy loss for a muon in various materials as a function of momentum is shown in figure 4.13.

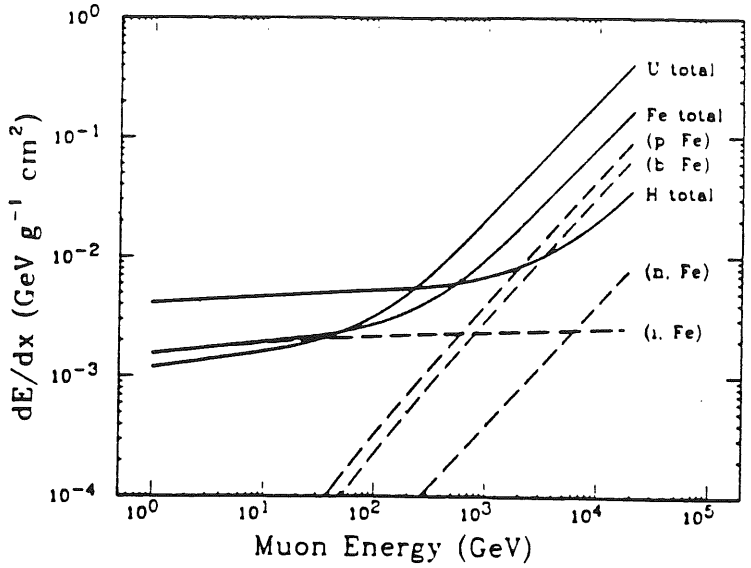

Figure 4.13: The average energy loss of a muon per g/cm^2 of hydrogen, iron and uranium as a function of muon energy. Contributions of several processes to dE/dx in iron are also shown: (p) direct e^+e^- pair production, (b) bremsstrahlung, (n) photonuclear interactions and (i) ionization. From [57].

In addition to the energy loss, the accumulated error due to Coulomb multiple scattering is calculated. This provides an estimate of the expected scatter on the extrapolated segment and is used in conjunction with the errors on the segments to calculate χ^2 for the track candidate. A Gaussian approximation to the Moliere theory [58] of multiple scattering is used. The width of this Gaussian is θ_0, given by [57]

$$\theta_0 = \frac{0.0136\ \text{GeV/c}}{p\beta} Z_{inc}\sqrt{\frac{L}{L_R}}\left[1 + 0.038\ \ln\left(\frac{L}{L_R}\right)\right]$$

where p is the particle momentum in GeV/c, β is the velocity in units of c, Z_{inc} is the charge of the incident particle in units of e, L is the distance traversed and L_R is the radiation length of the scattering medium. In this approximation θ_0 is the r.m.s. value of θ_{plane}, as shown in figure 4.14.

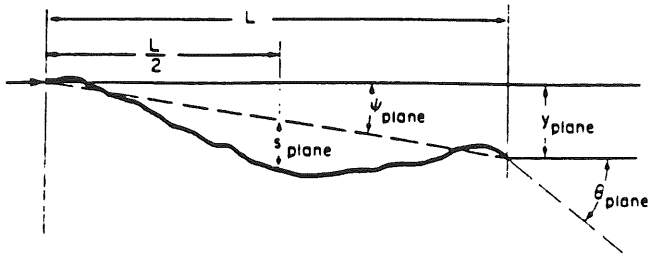

Figure 4.14: Multiple scattering in a plane. From [57].

The random values s, ψ, y and θ as shown in this figure are correlated and these correlations are retained throughout the extrapolation to produce a full covariance matrix for comparing the segment before the toroid with the extrapolated segment.

The above approximation is good to 11% for $10^{-3} < L/L_R < 100$ except for light elements and when the velocity is very small. Typically, 15 steps are used in the extrapolation, giving a length 8 cm for a track normally incident on the toroid. The radiation length of iron is 1.76 cm, so the ratio $L/L_R = 4.5$, within the validity of the approximation. The main source of deviation from this approximation is the occurrence of single large angle scatters, giving a much broader tail to the distribution than is the case for a Gaussian. These tails are a few percent in the regions where the Gaussian has become negligible.

Once the extrapolations have been done, all segments within the δr, $\delta\phi$ cut are compared with the extrapolated segments and a χ^2 is formed for each. This results in a χ^2 versus momentum plot. A quadratic fit is then made to the point corresponding to the minimum value of χ^2 found in the scan and the points in the scan either side of this minimum. The true minimum value of χ^2 is then calculated from this fit and the track candidate assigned a momentum corresponding to this value of χ^2. The track candidate is accepted if it has a χ^2 lower than a cut, nominally 75.0. If more than one segment is associated to the original segment, only the candidate with the lowest χ^2 is accepted.

Once all track candidates have been found, a search is performed to reject multiple tracks formed from the same hits. If more than one track uses an individual hit (including tracks which use different drift signs of the same hit), only the track with the lowest χ^2 is accepted.

The forward muon subdetector reconstruction is now complete and the information is written out in the MTKR BOS-bank.

Event Display Routines

Besides having all relevant information for the track in banks, it is essential to display this information visually. Therefore, subroutines were written for forward muon subdetector displays to fit within the framework of the main H1 event display program, H1ED [48]. This uses the LOOK graphical display system [41] as a histogramming package and interface to the graphics primitives, in this GKS graphics [47].

Options exist to view the chambers radially or in side views, and the granularity of the displays may be changed to show all cell boundaries or just octant outlines. It is possible to display single octants, whole layers or the whole detector. It is also possible to superimpose on the display the information on the Monte Carlo true hits. The structure of the LOOK program makes it easy to define more complex displays from combinations of simple displays.

Tzero And Drift Velocity Determination

The procedure used to determine the calibration constants (drift velocity and t_{zero}) of the forward muon chambers is detailed in [51]. The basic principle is that uniform illumination of a cell at normal incidence, uniform efficiency and constant drift velocity produces a time distribution of hits whose width in time corresponds to the full drift distance of 6cm and whose rising edge is at the appropriate t_{zero} for that cell. The distribution should have a flat plateau.

Deviations from this ideal behaviour occur if the drift velocity varies near the wire (or at the cell edge) or the tracks deviate from normal incidence. These effects, combined with a finite drift time resolution, smear the edges of the distribution and therefore make t_{zero} extraction more difficult. Any deviation from uniform efficiency, uniform illumination or constant drift velocity across the body of the cell changes the plateau of the distribution so it is no longer flat. If uniform illumination and efficiency are assumed, the drift time distribution may be used to extract the drift time to drift distance relationship. For this case, the time distribution may be divided into N equal time bins and the relationship

$$x_p = \frac{\Delta x}{N} \sum_{i=0}^{p} n_i$$

then holds, where x_p is the distance corresponding to the p^{th} time bin, Δx is the total drift distance and n_i is the number of hits in the i^{th} time bin. This procedure was used with a test setup to determine what value of the electric field should be used to provide as uniform a drift velocity as possible. The value chosen for the Autumn 1992 run was 0.45 kV cm^{-1}.

The other method used for calibration uses checksums based upon the fact that segments are straight lines and thus the drift times of the hits on a segment are therefore related. This may be used to extract an independent value of t_{zero} and also to provide a measurement of the spatial resolution of the chambers.

The values obtained for the Autumn 1992 run were (from [50]) t_{zero} = 216 ± 5 ns and v_{drift} = 4.93 ± 0.04 cm μs^{-1}. The r.m.s. drift distance resolution obtained was 310 ± 5 μm, compared with the design value of 250 μm.

Chamber Alignment

Finding the alignment of the forward muon system is not straightforward, as there is insufficient space around the chambers to allow a detailed survey. This means that the bulk of the alignment must be done using tracks in the detector. However, in 1992, only the theta chambers were installed and as this only gives a maximum of four hits on a segment, there is very little redundant information to work with. Alignment is done using beam halo tracks taken during dedicated runs with no field in the toroid to allow relative alignment of chambers before and after the toroid. The alignment procedures used are described in detail in [50].

Chapter 5: Tests Of The Forward Muon Reconstruction Code

In order to test the performance of the MTREC code, the H1SIM program was used to generate a dataset with 1,000 μ^+ and 1,000 μ^- (one track per event) with each of the following momenta: 5, 10, 20, 30, 40, 50, 75, 100, 125, 150, 175, 200, 225 and 250 GeV. The muons were generated in the range $-180° < \phi < 180°$ and $4° < \theta < 17°$, covering the whole of the forward muon system.

The muons were tracked from the H1 vertex straight to the forward muon system with the rest of the detector not present so that the parameters of the muons were well known at the start of the forward muon system and the muon tracks produced were radial. The simulated dataset was processed by the MTREC module with an option to produce histograms and n-tuples of the data switched on. The data were then analysed using the LOOK program. It should be emphasised that this is the cleanest possible environment for running MTREC and the results presented here are the upper limits of the code performance, not the expected values when the code is run on real data.

Previous studies [50] on the performance of the reconstruction code used an older version of the MTREC code which did not preserve full covariance information throughout and in which certain approximations were made, valid at the time as the phi chambers had not been installed. Newer versions of the code (H1REC version 3.09 and above) contain exact evaluations of co-ordinate transformations including full covariance information. In order to fully assess the performance of the reconstruction, studies were made using the new code with theta layers only and with phi layers installed. Only one simulation was performed but the phi chamber hits were ignored in one run of the reconstruction.

Momentum Resolution

The momentum resolution of the forward muon system is driven by two factors: multiple scattering in the toroid and the position resolution of the chambers. Both of these lead to errors in measuring the amount of bending suffered by the particle in the toroid. The amount of bending in the toroid is given by

$$\delta\theta = \frac{0.003\ B\ \delta l}{p}$$

as before, where B is the field in Tesla, p is the momentum in GeV/c and δl is the distance travelled in the field in cm. The scatter about this mean deviation due to multiple scattering in the iron toroid also varies as $1/p$. Hence, the fractional error on p, $\sigma(p)/p$, is

$$\frac{\sigma(p)}{p} = \frac{\theta_0}{\delta\theta}$$

where θ_0 is the deviation due to multiple scattering as before and the momentum dependence cancels. Taking notional values of B=1.5 T and δl=120 cm gives the total bending in the toroid as $0.576/p$ radian GeV. The value of θ_0 computed for the whole toroid is $0.140/p$ radian GeV. The resolution expected by considering just multiple scattering is therefore $\sigma(p)/p \approx 24\%$.

The resolution of the chambers contributes to the momentum resolution by producing an error on the measured theta angle of the segments before and after the toroid. As this error should be independent of momentum and the bending depends upon $1/p$, this contribution is expected to rise linearly with p.

The order of magnitude of this error may be estimated by assuming that the error in the radial distance from the beamline for a given hit is 250 μm (only true when the segment is in the middle of an octant). Considering only the first and last hits, the spacing between the hits is 65 cm and error on the slope of the line defined by these two hits is $\approx 5 \times 10^{-4}$. Since there are two segments involved, the error in theta angles used to determine momentum comes to $\approx 8 \times 10^{-4}$ radians. Thus the resolution in position gives a contribution to the momentum resolution of order

of 8×10^{-4} $p/0.576 \approx 0.13$ p %/GeV. This contribution is only 0.7% at 5 GeV, so at low momentum the resolution is driven by multiple scattering. However, as segments are made using between three and six hits, the actual error on the theta angle is expected to be smaller than the above estimate.

The momentum resolution of the reconstruction code may be determined by comparing the reconstructed value of momentum with the value that was generated. Plots were made of $(1/p)_{MC} - (1/p)_{REC}$ where the subscript MC indicates the true value from Monte Carlo and REC indicates the value returned by MTREC. The plots were made in $1/p$ rather than p as the errors are approximately Gaussian in $1/p$ (at least at lower values of momentum). Initially, a Gaussian was fitted to each plot. However, above 100 GeV, the method of fitting used no longer converged, a Gaussian being a very poor fit to the distribution. The LOOK peak-fitter program [38] was then allowed to choose the form of the peak and the sigma and central value of this fitted peak were then used in the analysis of these higher momenta tracks. A constant error of 2×10^{-3} was assumed on the values from the peak fitter.

The sigma value of each peak then gives the momentum resolution at several values of p for both positive and negative muons. Figure 5.1 shows $\sigma(1/p)/(1/p)$, the value of $\sigma(1/p)$ from the fit divided by $1/p$ to give the fractional error. A straight-line fit to the resolution in figure 5.1(a) (without the phi chambers) gave a constant term of 22.3±0.4% and a slope of 0.057±0.005%/GeV. When the phi chambers were included, as in figure 5.1(c), the constant term became 23.4±0.3% and the slope was 0.049±0.004%/GeV. These values are consistent with the estimates calculated above. The resolution for radial tracks was not found to improve when phi chambers were included. However, the same is not expected to be true for non-radial tracks where the phi angle of the track, Φ, is no longer the same as the phi co-ordinate of the track, ϕ.

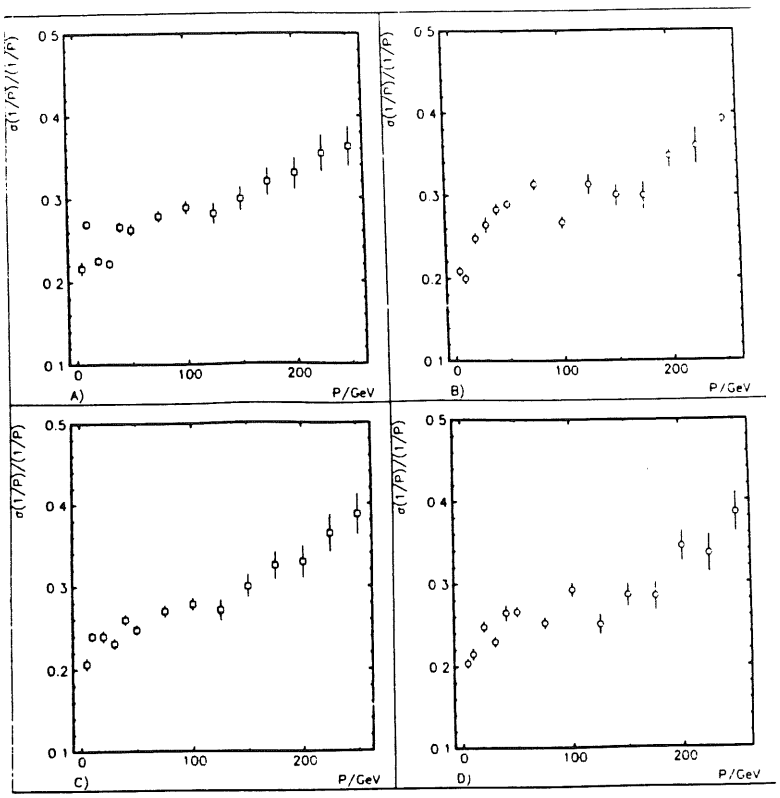

Figure 5.1: Fractional resolution in $1/p$ as a function of momentum for a) μ^+ without phi chambers, b) μ^- without phi chambers, c) μ^+ with phi chambers and d) μ^- with phi chambers.

In addition to the resolution, the value of momentum reconstructed must be checked for any systematic variation. A plot was made of the deviation of the centre of the peak in the $(1/p)_{MC} - (1/p)_{REC}$ plots, $\Delta(1/p)$, as a fraction of $1/p_{MC}$ against $1/p_{MC}$. This is shown in figure 5.2. It was observed that there was a systematic deviation: the magnitude of the reconstructed momentum was systematically too low at low momenta and too high at high momenta. The effect was found to be in the same sense for positive and negative muons. The effect was most pronounced at low values of momentum where the shift was as high as 10%. This effect is obviously not desirable and is not fully understood. It is possible that fitting a quadratic to the χ^2 distribution might introduce such a shift if the real χ^2 distribution were asymmetric.

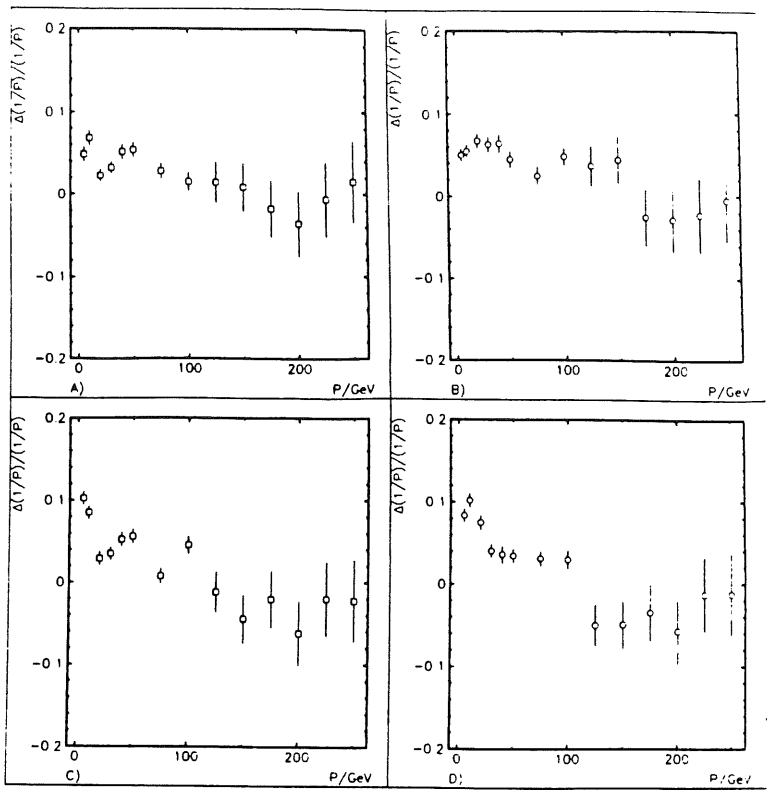

Figure 5.2: Fractional systematic deviation in $1/p$ as a function of momentum for a) μ^+ without phi chambers, b) μ^- without phi chambers, c) μ^+ with phi chambers and d) μ^- with phi chambers.

A check must also be made to ensure that the error on the momentum as calculated by the reconstruction code is approximately correct. A residual plot was therefore produced. The value of the residual is given by

$$Residual = \frac{p_{MC} - p_{REC}}{\sigma_{REC}}$$

where σ_{REC} is the error on the momentum as estimated by MTREC. If the reconstruction is functioning perfectly, this distribution is a Gaussian centred at zero with unit sigma. If the value of the reconstructed momentum is wrong, the peak is shifted from zero. If the error estimate is wrong, the peak has sigma not equal to unity.

The momentum residual plots are shown in figure 5.3 with peaks from the LOOK peak-fitter superimposed. The peaks were found to be non-Gaussian and asymmetric. This may be a result of the fact that the distribution is Gaussian in 1/p rather than in p. Also, as the reconstructed value of momentum was found to have a systematic shift, it is possible that

summing over all values of momentum distorts the peak shape. The peaks were also found to be offset from zero, the net result of the systematic shifts measured above. However, their sigma values were close to 1.0, meaning that the error calculated by the reconstruction code was approximately equal to the spread of the reconstructed values about the true value.

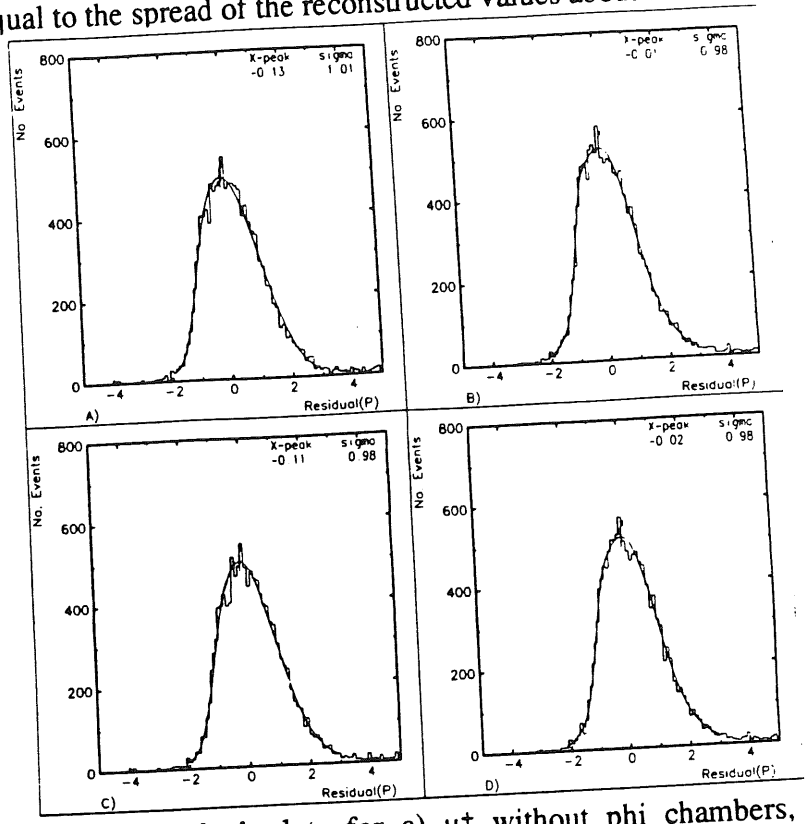

Figure 5.3: Momentum residual plots for a) μ^+ without phi chambers, b) μ^- without phi chambers, c) μ^+ with phi chambers and d) μ^- with phi chambers.

Efficiency

The second major test of the reconstruction code is to evaluate how efficient it is at reconstructing muon tracks. The datasets generated were clean, with only one track per event, no noise added and no extra material in front of the chambers to produce showers or scatter the muons. The efficiency of the reconstruction code under these circumstances sets the upper limit for performance on data (which is certainly not clean in the above sense). The efficiency for reconstruction in a given bin is defined here as the fraction of tracks simulated within that bin that gave at least one track as an output. No requirement was made on the parameters of the output track.

Figure 5.4 shows the reconstruction efficiency for μ^+, μ^- with and without the phi chambers as a function of incoming track momentum, integrated over all incoming θ, Φ. The efficiency was found to vary from 80% for μ^+ (85% for μ^-) and rose to a plateau at 89±1%. The lower efficiency at low momenta is due to multiple scattering or a single large-angle scatter deviating a muon that passes through the edge of the toroid so that the muon leaves the toroid at its inner or outer radius, missing the later chambers. Negative muons are focussed in the toroid so those nearer the inner radius are more likely to escape than positive muons. The opposite is true at the outer radius, but the toroid inner radius is 65 cm c.f. the chamber inner radius of 48 cm whereas the toroid outer radius is 290 cm c.f. the chamber outer radius of 198 cm for theta layer one. The effect is therefore more important for the negative muons.

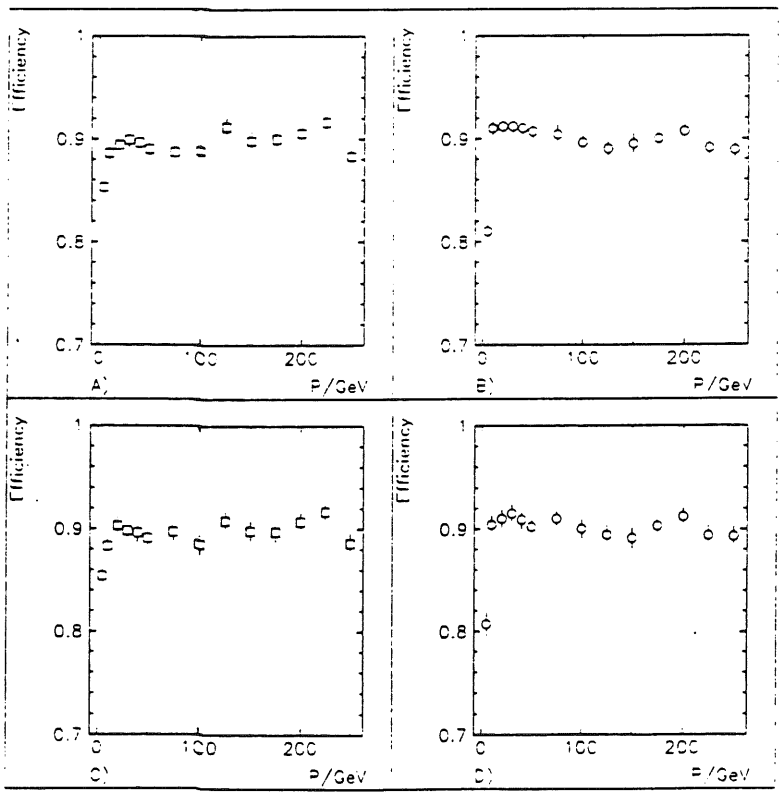

Figure 5.4: Reconstruction efficiency versus momentum for a) μ^+ without phi chambers, b) μ^- without phi chambers, c) μ^+ with phi chambers and d) μ^- with phi chambers.

Figure 5.5 shows the reconstruction efficiency as a function of incoming track θ, integrated over all momentum, charge and Φ. The drop-off which was observed below 0.1 radians and above 0.27 radians was due to the edges of the geometric acceptance of the chambers. The plateau was at 92.0±0.8%. The errors were based on the statistics in each bin. An efficiency of more than 100% may arise as the original dataset was generated with the events randomly spread over the full range rather than in discrete bins as for the momentum. The statistical fluctuations of the two figures are 100% correlated as the same input dataset was used for runs with and without the phi chambers. The inclusion of the phi chambers had no significant effect on the efficiency as a function of θ.

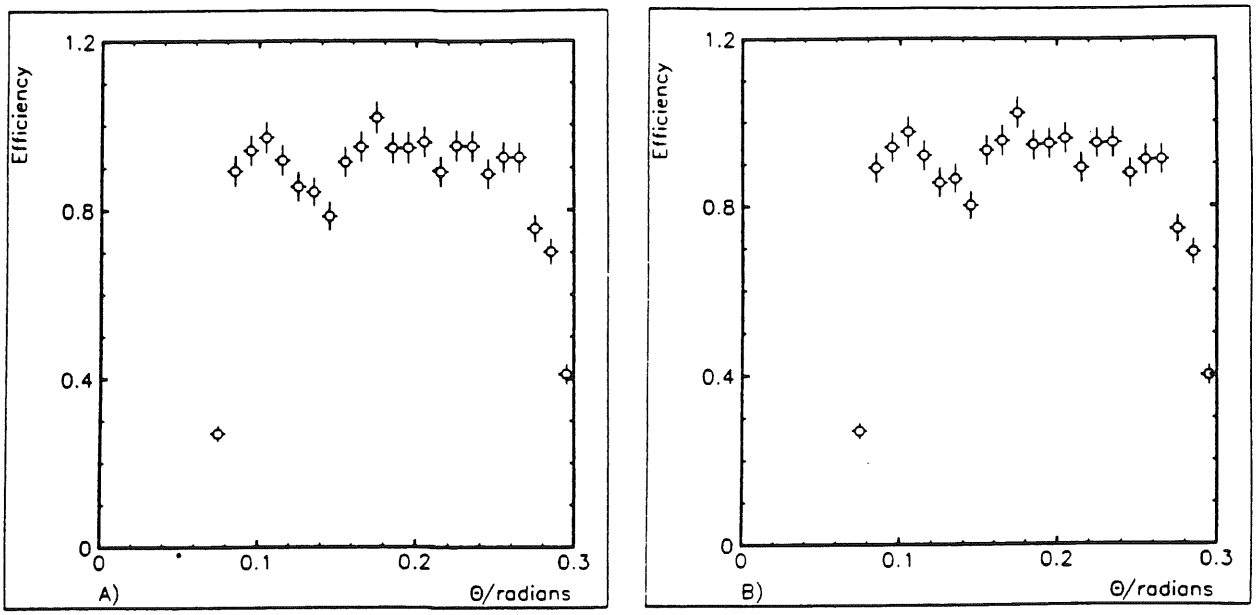

Figure 5.5: Reconstruction efficiencies versus θ a) without phi chambers and b) with phi chambers.

Figure 5.6 shows the reconstruction efficiency as a function of position within an octant, i.e. as a function of $\phi_{off} = \Phi - \phi_{centre}$, where ϕ_{centre} is the phi co-ordinate of the centre of the octant containing the track. The data were integrated over all momentum, charge and θ. There is no reason to expect that one octant be different from another in the simulation, so plotting against

ϕ_{off} gives eight times the statistics and hence allows smaller bins sizes. The plateau was at 88±0.7%. The drop-off observed in the first and last bins was due to the edges of the acceptance within an individual octant. The inclusion of the phi chambers was found to have no effect on the efficiency with Φ.

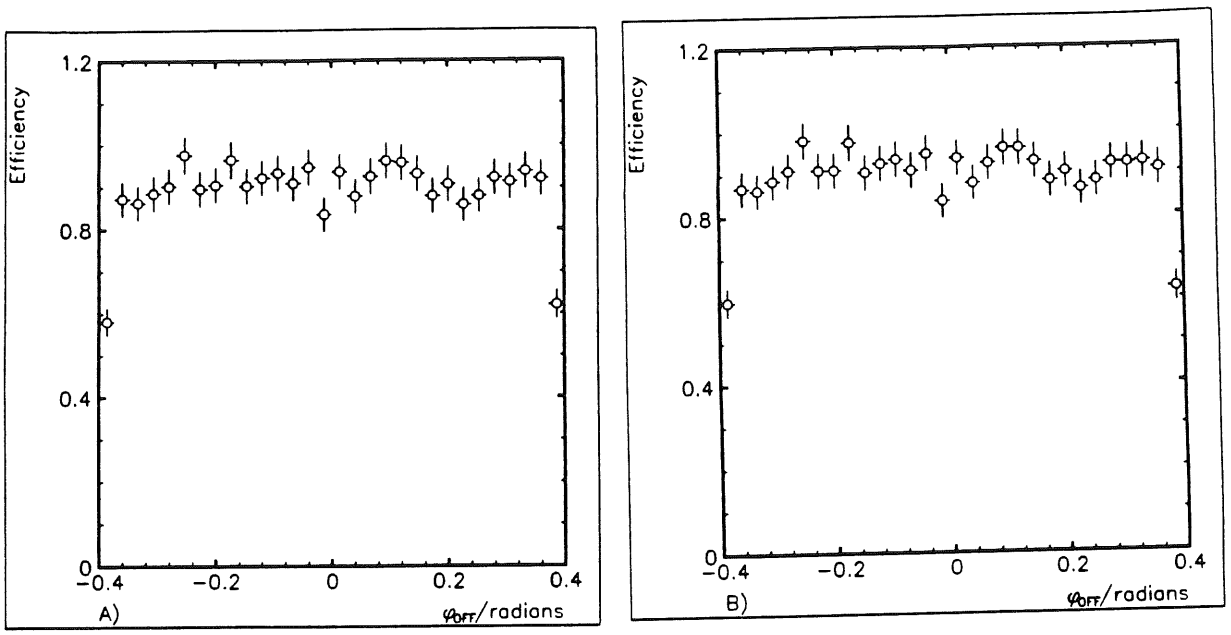

Figure 5.6: Reconstruction efficiencies versus $\phi_{off} = \Phi - \phi_{centre}$ a) without phi chambers and b) with phi chambers.

Resolution In Theta, Phi And Position

The momentum resolution of the forward muon detector is important for stand-alone measurements. However, muons in the forward muon system may also leave tracks in the forward tracker or the instrumented iron. In order to be able to link these tracks together it is necessary to know the resolution in the two track angles θ and Φ and the resolution in position, H1 x and y. It is also important to know the estimated errors on these measurements. The error estimated by the reconstruction code was checked using residual plots as was done for the momentum. The residual in a quantity x is defined as

$$Residual(x) = \frac{x_{MC} - x_{REC}}{\sigma_{REC}}$$

where x_{MC} is the true value of x from the Monte Carlo program, x_{REC} is the value of x returned by the reconstruction program and σ_{REC} is the estimate of the error on x returned by the reconstruction program.

Figures 5.7(a) and 5.7(b) show θ_{MC} - θ_{REC} for all tracks with and without the phi chambers present. As can be seen from the plot, the resolution was not well described by a Gaussian and the peak was therefore fitted using the LOOK peak fitter. The sigma of the peak without the phi chambers was 0.00161 radians and its centre was at 9×10^{-5} radians, consistent with zero. However, there appeared to be two contributions to the peak, one a sharp peak and one a much broader peak. This may be understood by considering the fact that the theta angle measured at the centre of an octant depends only upon the drift co-ordinate whereas at the edge of an octant it depends upon a mixture of the drift and charge division co-ordinates. The sigma of the peak with the phi chambers was 0.00111 radians and its centre was at 9×10^{-5} radians. The two component structure was much less pronounced. Figures 5.7(c) and 5.7(d) show the residuals in θ. The sigma values of the peaks were found to be 0.79 and 0.95 without and with the phi chambers respectively, suggesting that the error in theta was somewhat overestimated.

Figures 5.8(a) and 5.8(b) show Φ_{MC} - Φ_{REC} for all tracks with and without the phi chambers present. The sigma of the peak without the phi chambers was 0.266 radians and the centre was at 0.008 radians. The sigma of the peak with the phi chambers was 0.0027 radians and the centre was at 0.05. It was therefore concluded that the addition of the phi chambers allowed a much better measurement of the track Φ angle. Figures 5.8(c) and 5.8(d) show the residuals in Φ. The sigma values of the peaks were 0.84 and 0.94 without and with the phi chambers. This suggested that the errors were slightly overestimated by MTREC.

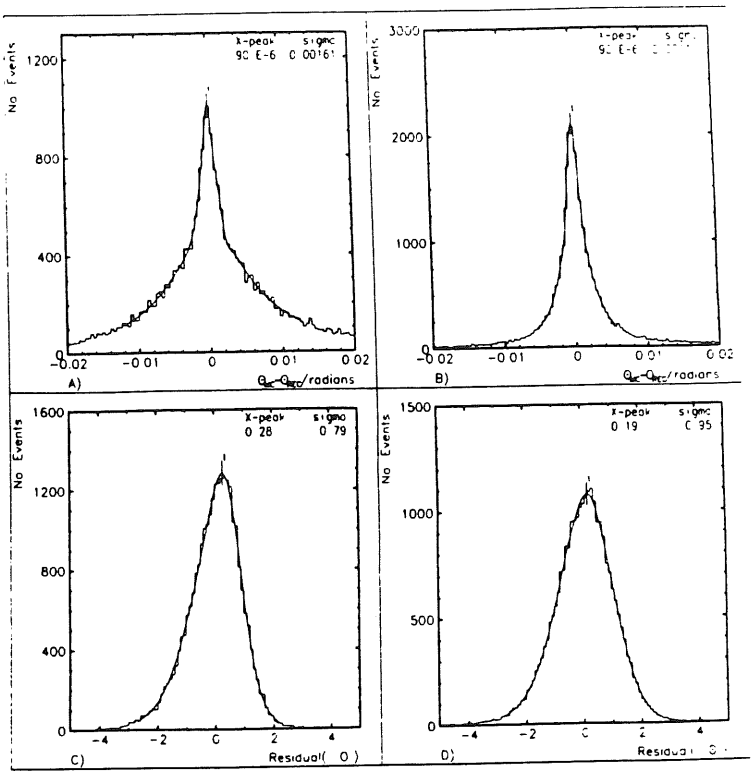

Figure 5.7: a) Resolution in θ without phi chambers, b) resolution in θ with phi chambers, c) residuals in θ without phi chambers and d) residuals in θ with phi chambers.

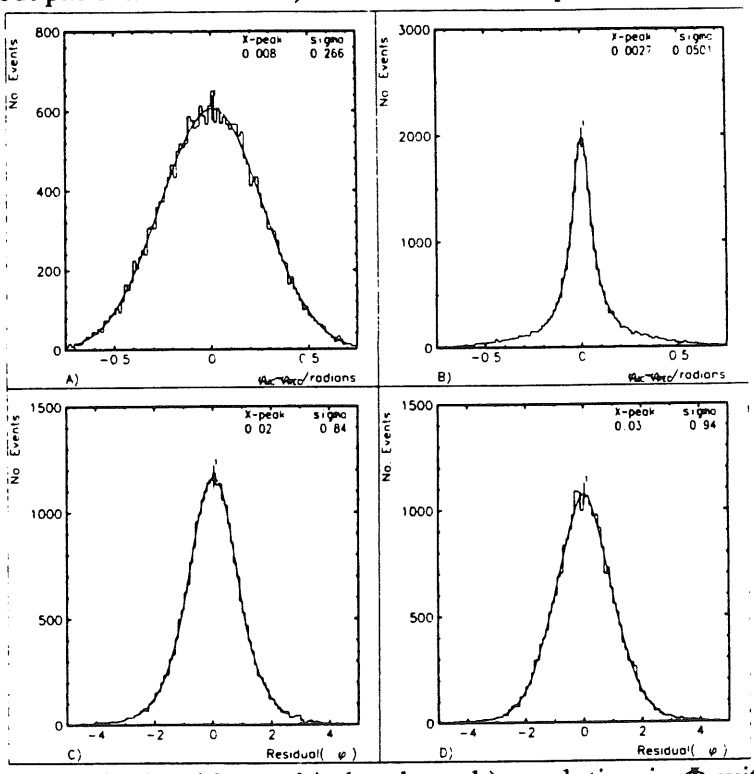

Figure 5.8: a) Resolution in Φ without phi chambers, b) resolution in Φ with phi chambers, c) residuals in Φ without phi chambers and d) residuals in Φ with phi chambers.

Figures 5.9(a), 5.9(b), 5.10(a) and 5.10(b) show x_{MC} - x_{REC} and y_{MC} - y_{REC} for all tracks with and without the phi chambers present. The sigma of the peaks without the phi chambers present were 1.0/1.0 cm for x/y, and the centres were found to be at 0.01/-0.04 cm. With the phi chambers included, this became sigma 0.172/0.166 cm and centre -0.005/-0.005 cm. It was concluded therefore that the overall precision of x and y measurement was improved by the addition of the phi chambers because good measurements were being made in two perpendicular co-ordinates rather than one good and one poor measurement. Figures 5.9(c), 5.9(d), 5.10(c) and 5.10(d) show the residuals in x and y, with sigma consistent with 1.0 for all plots.

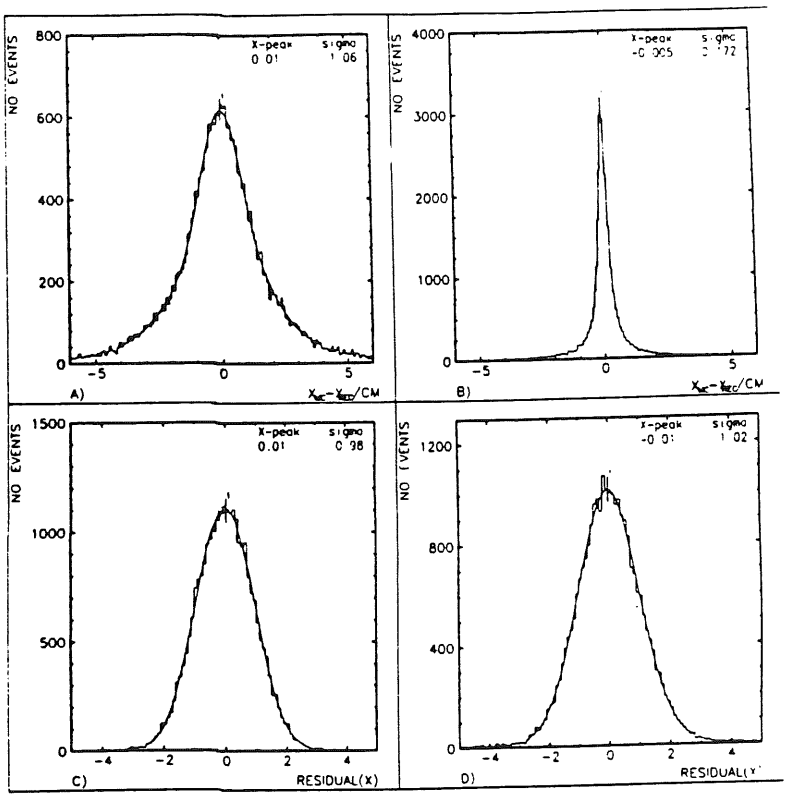

Figure 5.9: a) Resolution in x without phi chambers, b) resolution in x with phi chambers, c) residuals in x without phi chambers and d) residuals in x with phi chambers.

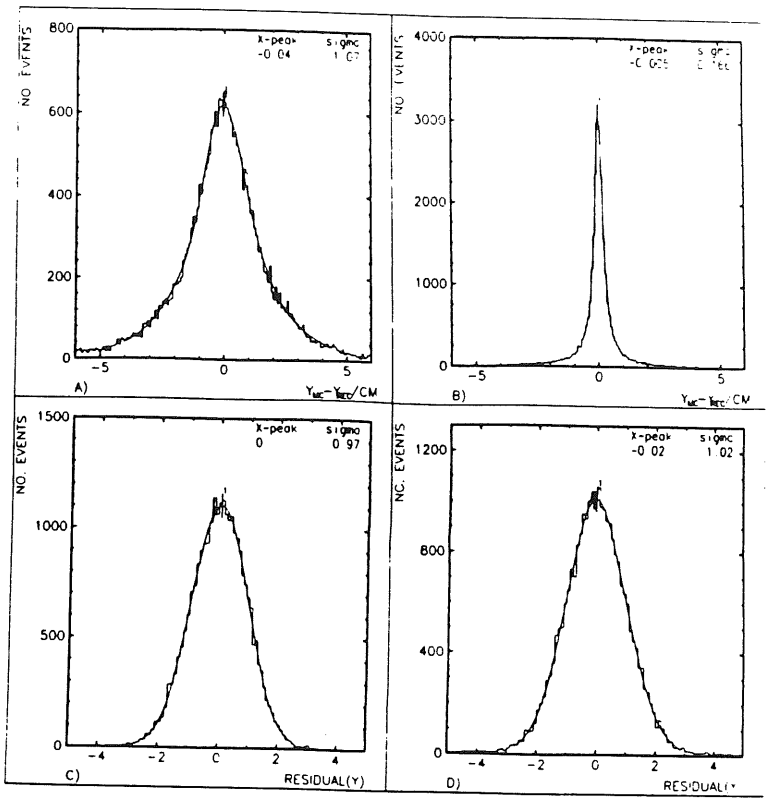

Figure 5.10: a) Resolution in *y* without phi chambers, b) resolution in *y* with phi chambers, c) residuals in *y* without phi chambers and d) residuals in *y* with phi chambers.

The above resolutions were an average over the whole detector for a large number of tracks. There are systematic effects in these resolutions, particularly when the phi chambers are excluded. For example, measurement of the θ angle is dependent upon a good measurement of the radial co-ordinate. In the centre of an octant, this is the drift co-ordinate and hence is well measured. At the edge of an octant, this is a mixture of drift and charge division co-ordinates, giving a larger error on the measurement. Figure 5.11 demonstrates this, plotting the value of $\theta_{MC} - \theta_{REC}$ against $\phi_{off} = \Phi - \phi_{centre}$. The value of θ was reconstructed much better at the centre of an octant than at the edge when the phi chambers were absent. When they were present the difference in reconstruction across on octant was observed to be much smaller.

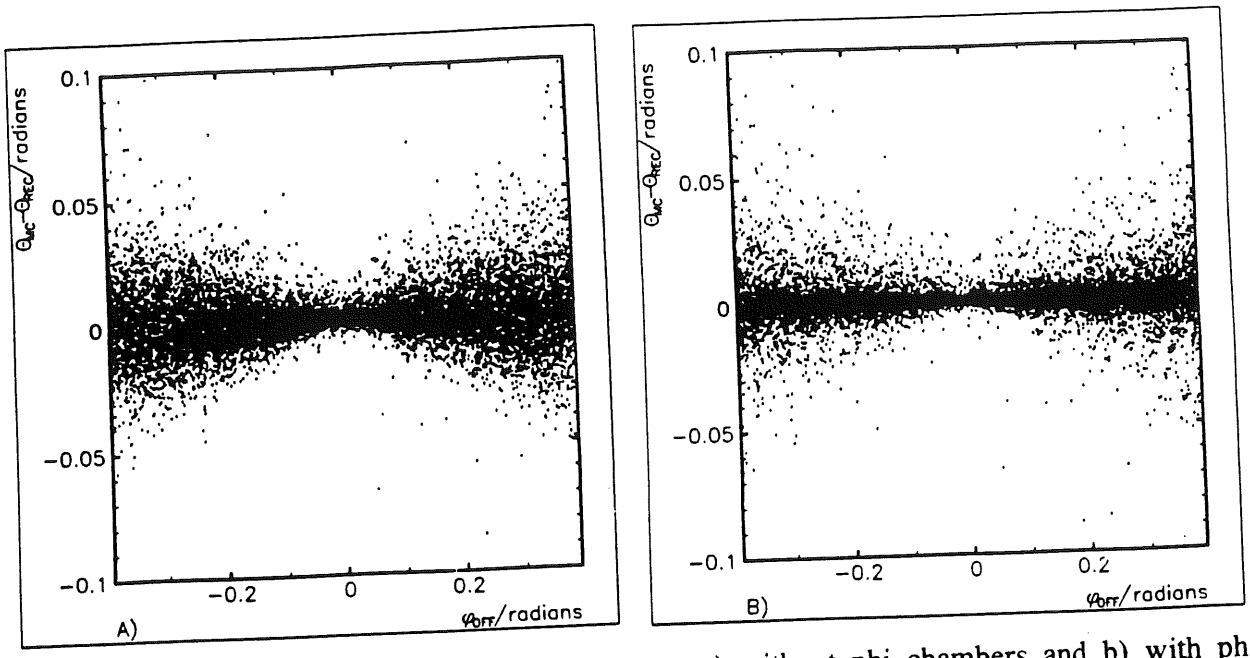

Figure 5.11: θ_{MC} - θ_{REC} against $\phi_{off} = \Phi - \phi_{centre}$ a) without phi chambers and b) with phi chambers, showing the systematic variation in θ resolution across an octant.

Real Data

The studies presented in this report have used simulated data generated by the H1SIM program with an error on the drift co-ordinate of 250 μm and an error on the charge division co-ordinate of 3.33% of the struck wire length. The chambers were assumed to be perfectly aligned and no noise hits were introduced. It has already been reported that the resolution on the drift co-ordinate for the real detector was 310±5 μm in 1992 and it is clear that much more work is necessary to align and calibrate the chambers so that the design resolution of 250 μm can be attained.

Studies are being carried out intensively at DESY, Manchester and Birmingham to understand the real data and to align and calibrate the detector. As yet, the low luminosity delivered by the HERA machine has meant that the main source of muons for the forward muon system has been beam halo. Of the particles created in such interactions, only muons are capable of penetrating the shielding around H1 in significant numbers and giving tracks in the forward

muon spectrometer. Figure 5.12 shows a beam halo muon track passing through the detector with the reconstructed track extrapolated through the toroid and the two segments used in forming the track superimposed. Figure 5.13 shows a heavy flavour event in the H1 detector where one of the two muons produced was reconstructed in the forward muon spectrometer.

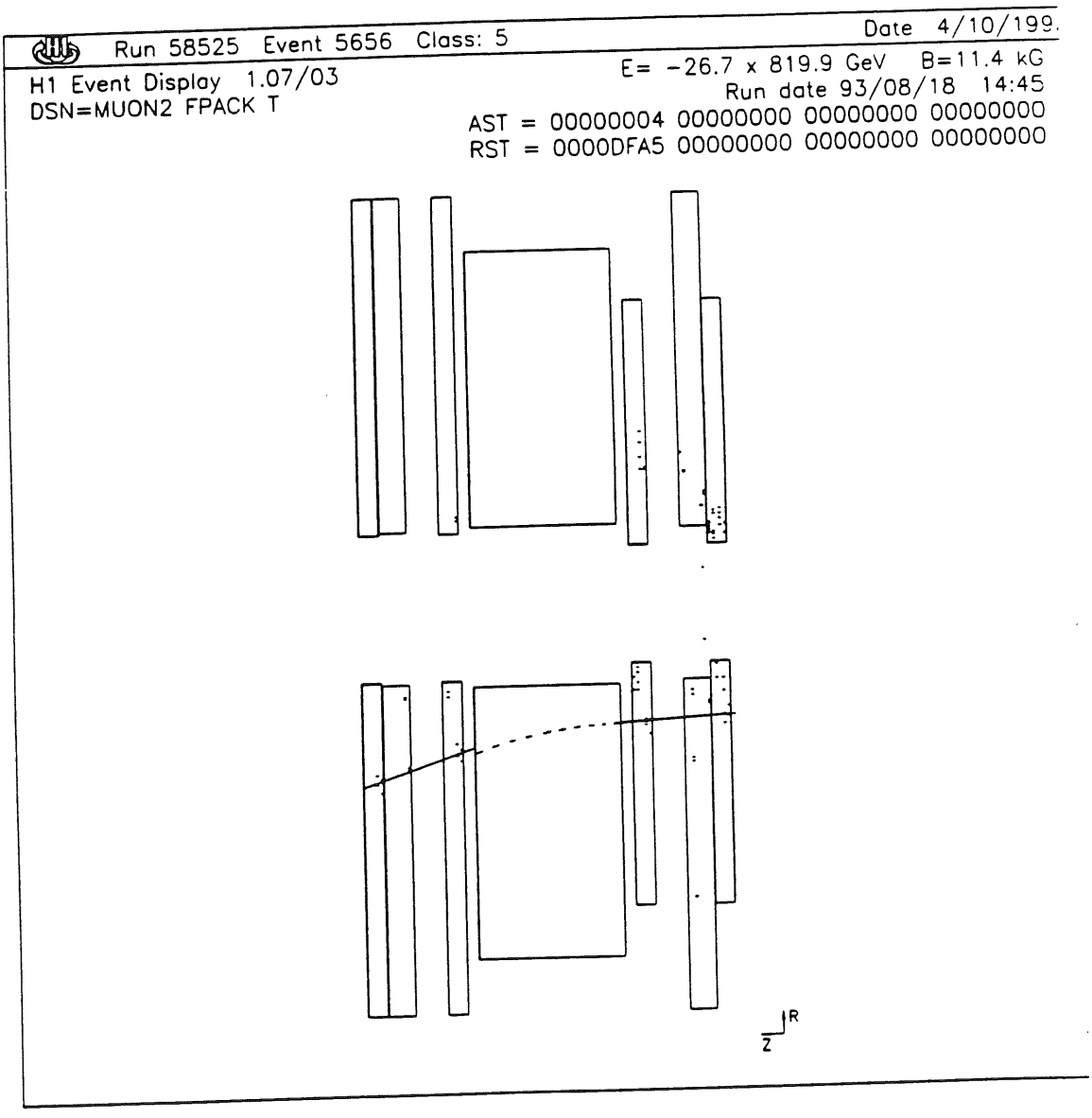

Figure 5.12: A beam halo muon in the H1 forward muon spectrometer. Solid lines are the segments used in forming the track and the dotted line shows the extrapolation through the toroid at minimum χ^2.

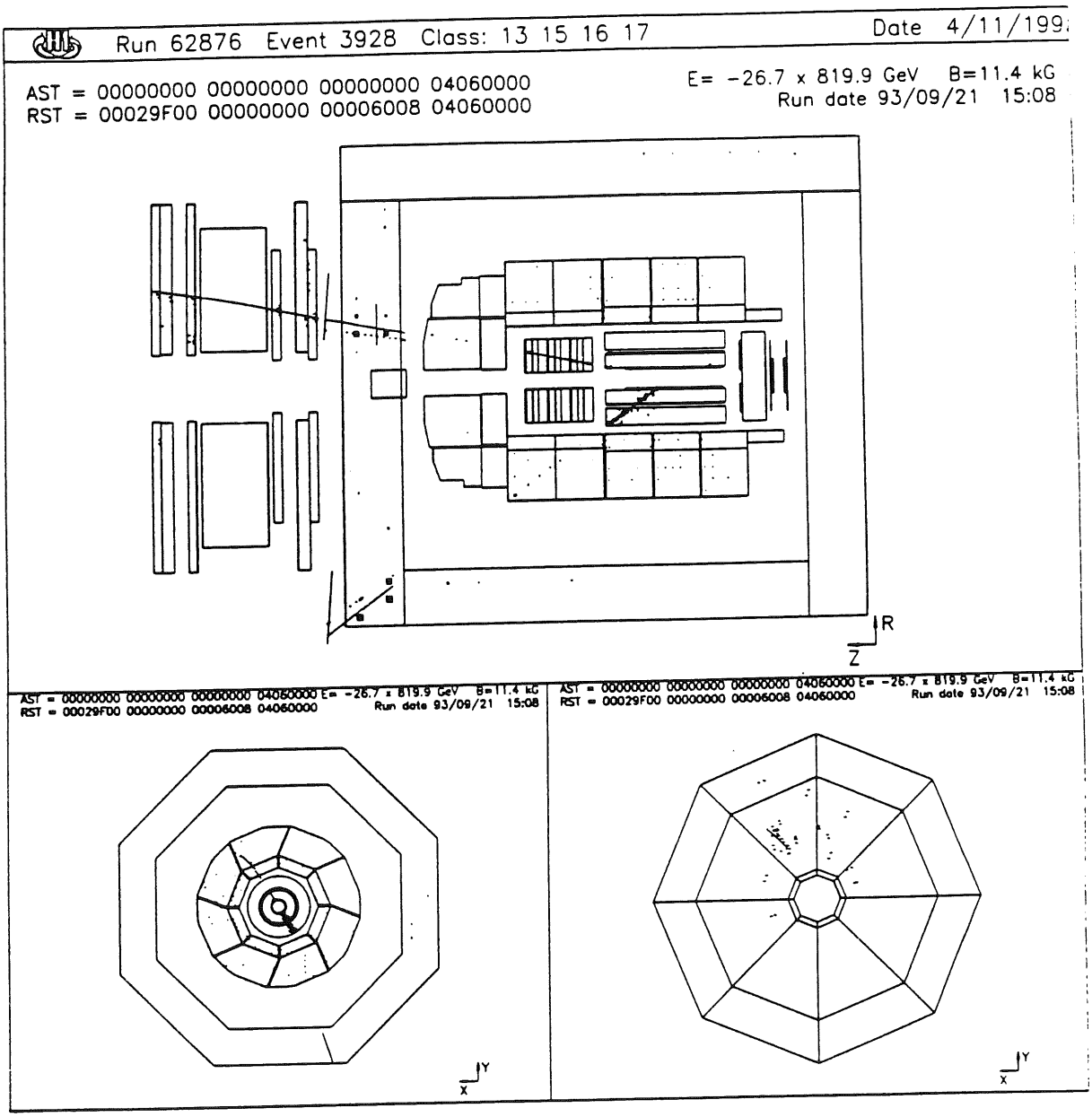

Figure 5.13: A heavy-flavour physics event in which one of the two muons produced was detected in the forward muon spectrometer.

Chapter 6: The Photon Remnant In Resolved Photoproduction At HERA

Introduction

In chapter 2, it was emphasised that resolved events are expected to have a remnant from the photon whereas direct events, in which the whole photon interacts, are not. A search for this photon remnant in photoproduction events may therefore provide a means of discriminating between direct and resolved events. It is expected that resolved processes will dominate when tagged electrons are used as the electron tagger acceptance only covers the region $1 \times 10^{-8} < Q^2 < 0.01\ \mathrm{GeV}^2$.

Therefore, the first task of this study is to confirm the existence of the photon remnant. In the simple parton picture, one parton from the photon interacts with a parton from the proton and the other parton from the photon is left to carry the remainder of the photon's momentum. Hence, in this simple picture, the photon remnant has no transverse momentum and is lost down the beam pipe. However, as the remnant is not a colour singlet, it must be linked by colour forces to the rest of the event. This is expected to impart sufficient transverse momentum to the photon remnant to enable it to be detected. Once the existence of the photon remnant has been confirmed, its properties should be examined and compared with theoretical predictions.

Additionally, the photon remnant can provide useful information on the kinematics of the events. The normal procedure for calculating the kinematics of a photoproduction event makes use of the information about the partons using information from the final state jets. In principle, the photon remnant may be used as an independent check of x_γ, the fraction of the photon energy taken by the parton which hard scattered. When x_γ is small, the photon remnant carries most of the four-momentum of the initial photon and may therefore be easier to reconstruct than the jets.

A complication to the study is an uncertainty in how best to define the photon remnant. As an illustration of the problem, the electron side of a photoproduction event is shown in figure 6.1. It is not clear where initial state radiation from the initiator quark should be placed.

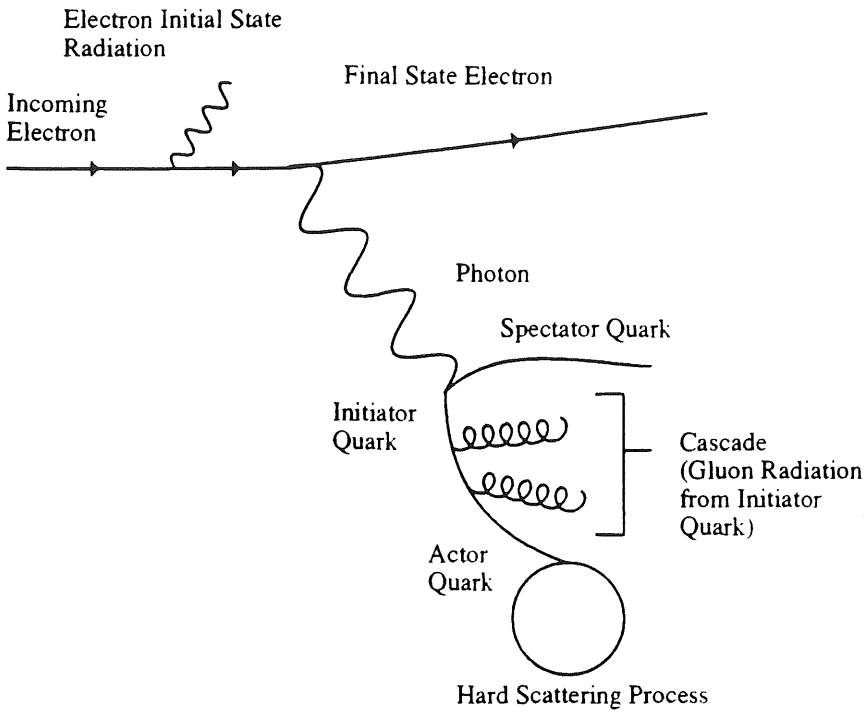

Figure 6.1: The electron side of a HERA resolved photoproduction event.

In chapter 2, it was assumed that the photon remnant comes from the step where the initiator and spectator quarks split. However, it is clear that the detector will not be able to separate out the contribution from the gluon radiation from the initiator quark and therefore the photon remnant must be defined to include all partons from the original photon except for the parton that hard scattered. This definition, whilst not exactly equivalent to the previous one, is more meaningful when the limits of what can be reconstructed by the detector are taken into consideration.

The uncertainty in defining the photon remnant also leads to an uncertainty in defining x_γ as it is not clear whether the relevant x_γ is for the initiator quark or for the actor quark in figure 6.1. With the new definition of the photon remnant, it is clear that the appropriate x_γ is that of the actor quark. This is the x_γ that can be reconstructed from the final state jets and also has the required property that

$$x_\gamma + x_{rem} = 1$$

where x_{rem} is the fraction of the incoming photon's four-momentum taken by the photon remnant

(according to the new definition).

The purpose of this study was to compare data with Monte Carlo predictions rather than to extract absolute cross-sections. Therefore, no attempt has been made to unfold any measurements back to the parton level. Also, the errors shown in all plots in this chapter are statistical only as no attempt has been made to evaluate the systematic errors.

Data Sets

A) Photoproduction Pre-selection

For the 1992 data, runs were assigned a quality flag of good (where all subdetectors were available), medium (where the central tracking, calorimetry and electron tagger were fully functioning) or poor (where a critical subdetector was unavailable). A sample of electron tagged photoproduction candidates has been selected for analysis using only good and medium runs, corresponding to an integrated luminosity of 23.8 ± 1.5 nb^{-1}. From this data sample, a pre-selection of events taken with the ETAG*t0 trigger has been made. This trigger requires an electron candidate in the electron tagger (with an energy greater than 4 GeV), no photon in the photon tagger (i.e. less than 2 GeV deposited in the photon tagger) and at least one track in the MWPCs of the central tracker. In addition to this trigger requirements, cuts were made to reduce the number of background events, as described in the 'Data Selection' section. The resulting pre-selection contained 4927 events.

B) Simulation

The PYTHIA 5.6 generator [60] was used to to compare theoretical predictions with the data. The structure function used for the photon was the leading-order parameterisation of GRV [27] contained in PDFLIB [61]. The proton structure function used was the MRSD0 parameterisation [62].

The first stage of the generation procedure used was to generate the parameters of the scattered electron and photon using the Weizsacker-Williams approximation (allowing initial

state radiation from the electron). Before carrying out the rest of the generation procedure, the events were randomly accepted or discarded with a probability of acceptance equal to the tagger acceptance for the scattered electron. This was done in order to save processing time and to ensure that only events within the acceptance of the tagger were fully generated.

The events were produced using flat distributions in x_γ and x_p, with each event being given a weight based on the probability of obtaining that value of x given by the structure function parameterisations. This has the advantage of producing more events in the tails of the distribution (even though they have small weightings) and saves processing time by not generating large numbers of events in areas that are not necessarily of interest.

This method also has the advantage that different parameterisations of the structure functions may be considered by reweighting the events, avoiding additional Monte Carlo production. However, care must be taken when comparing the predictions of the two different structure function parameterisations as reweighting the same events leads to correlations between the statistical fluctuations in the two predictions. The structure function parameterisation chosen for the reweighting was the LACIII set [25]. This was chosen because it differs significantly from the GRV parameterisation used in generation. Hence, a comparison of the two predictions indicates whether or not the current level of statistics is sufficient to distinguish between alternative structure function parameterisations.

The events generated by the above method were passed through full detector simulation (using H1SIM) and reconstruction (using H1REC). These events were then subject to the same cuts as the data. It was assumed that the trigger efficiencies for the data and Monte Carlo were the same. The sum of the event weights generated before acceptance considerations corresponded to an integrated luminosity of 244.4 nb^{-1}. A scale factor of 0.0974 was therefore applied to the weighted sample in order to compare absolute Monte Carlo predictions with the 23.8 nb^{-1} of data collected in 1992. Applying the acceptance and pre-selection cuts resulted in a Monte Carlo pre-selection of 6744 events.

C) Proton Pilot Bunch Data

Most of the background for photoproduction events is expected to come from a coincidence of a fake electron tagger signal with a proton induced background interaction inside the H1 detector. In the Autumn 1992 run, HERA ran with two pilot bunches, one for the electrons and one for the protons. These pilot bunches had no counterpart in the other beam so interactions produced by these bunches were purely background events. A sample of 3949 proton beam induced background events was prepared and inspected to ensure efficient background rejection. It was not possible to scale the pilot bunch sample up with the luminosity to predict the background as the background rates scale with proton beam intensity and vacuum conditions. It has been assumed in this analysis that the properties of beam induced interactions were similar for pilot and interacting bunches (despite the slightly different conditions encountered by these non-interacting bunches). Using this assumption the proton pilot bunch data may be used to estimate the background contamination in the data sample.

Data Selection

In 1992, the H1 detector was still in the early stages of its operation and some subdetectors were unreliable, poorly treated by reconstruction or not fully instrumented. For this reason, the forward tracker, the instrumented iron calorimetry and the plug were excluded from the analysis. In addition, tracks in the central tracking detector were required to have at least 10 hits in the CJC or 3 in the BPC, lie within the range $5.0° < \theta < 175.0°$ and have a distance of closest approach to the beam axis of less than 2 cm. Tracks were further required to have values of χ^2 from the vertex fit of less than 10,000, a start radius of less than 30.0 cm and to start less than 50.0 cm from the event vertex.

The clustering algorithm used in the calorimetry was not fully reliable in Autumn 1992 so the calorimeter cell information, corrected for dead material, was used for energy flow measurements. Noisy cells with a deposited energy of less than 0.1 GeV in the liquid argon (0.6 GeV for the BEMC) were rejected. The main calibration studies for the BEMC have been

concerned with electromagnetic energy deposition. Monte Carlo studies [63] indicate that a scale factor of 1.6 should be applied when using the BEMC to measure hadronic energy. This factor was applied after the noise cut.

Samples taken with the ETAG*t0 trigger were expected to be relatively free of background. However, background events may be accepted by the trigger if a proton beam-gas interaction occurs inside the H1 detector region while an electron beam-gas or beam-wall interaction scatters an electron into the tagger. In addition to this background, events with beam halo muons in the detector and events with a cosmic ray passing through the detector must also be rejected. For some of the Autumn 1992 data, there was coherent noise in the liquid Argon calorimetry which makes some individual events unuseable.

Standard H1PHAN routines [49] were used to reject cosmic ray, beam halo and coherent noise contaminated events by insisting that there be no cosmic ray muon found, no coherent noise found and that the energy deposited in the calorimeters from beam halo muon candidates be less that 7.5 GeV.

As discussed in chapter 3, the acceptance of the electron tagger covers the range $0.2<y<0.8$ so no photoproduction event accepted by the ETAG*t0 trigger should have a value of y outside this range. Hence, it was insisted that the energy of the electron detected in the electron tagger must lie between 8 GeV and 20 GeV (corresponding to $0.25 < y < 0.7$). Figures 6.2(a) and (b) show the energy spectrum in the tagger for data and GRV Monte Carlo before this cut, which was made on the pre-selection. The shape of this distribution is essentially governed by the acceptance of the electron tagger. The differences between the data and Monte Carlo prediction arise from the fact that the Monte Carlo acceptance is unsmeared by resolution at this stage and the ETAG*t0 trigger conditions have yet to be imposed upon the Monte Carlo.

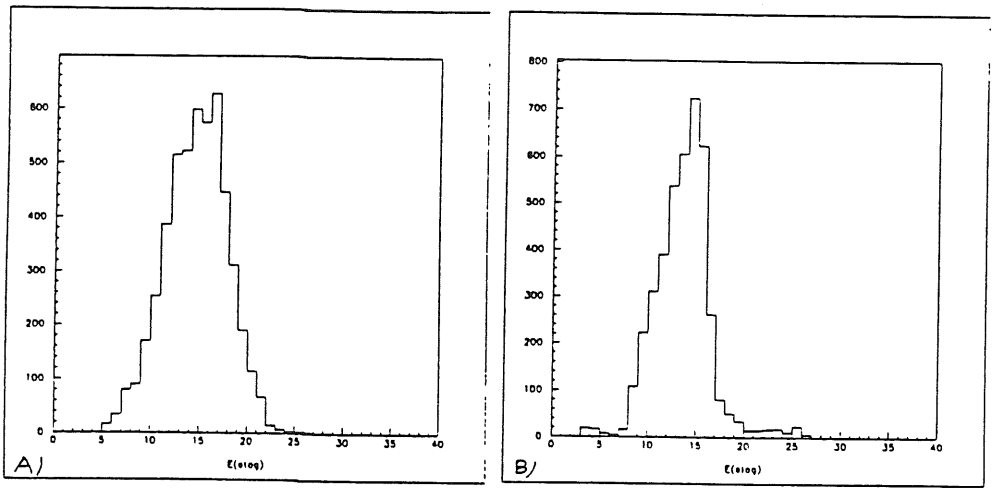

Figure 6.2: Electron tagger energy spectrum before applying cuts for a) data, b) GRV Monte Carlo.

It was further insisted that a primary vertex be reconstructed and that the vertex be within the fiducial interaction region of -44.0 cm $< z_{vertex} <$ 44.0 cm. This cut was imposed in order to reduce the number of events from proton beam-gas interactions. Losses due to this cut have been determined by the photoproduction group to be (12±2)% using a track independent trigger [64]. Figures 6.3(a) and (b) show the distribution of the vertex in z for data and GRV Monte Carlo respectively before applying this cut. Figure 6.3(c) shows the distribution of the vertex in z for proton pilot bunch data. The large peak at zero in this figure, which extended to 1440, is shown truncated. This peak corresponded to events where no good vertex was reconstructed. The distribution was found to extend further in z for the pilot bunch than for the data, as expected. The actual distribution of pilot bunch events was expected to be flat, but this was modulated by the acceptance and efficiency of the central tracking chambers which varies with z. From figure 6.3(c) it was estimated that 50% of proton pilot bunch events have a good reconstructed vertex within the fiducial region.

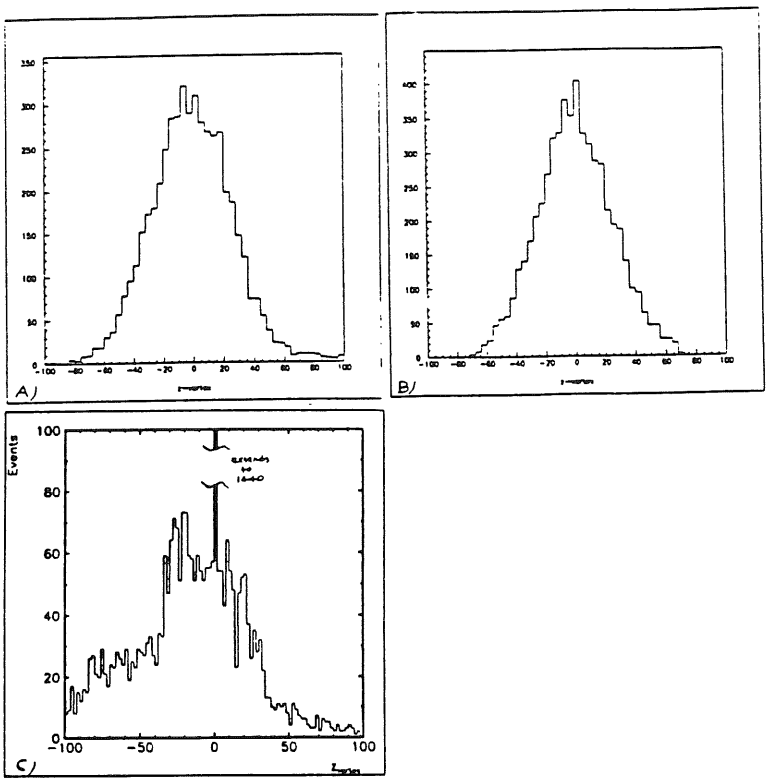

Figure 6.3: distribution of z_{vertex}, the z position of the primary reconstructed vertex before applying cuts for a) data, b) GRV Monte Carlo, c) Proton pilot bunch.

To tag events with a hard scatter, the scalar sum of the transverse energy in the event was required to be above 10 GeV. The transverse energy, E_T, of a particle is defined as

$$E_T = E \frac{p_T}{p}$$

where E is the energy of the particle, p is the magnitude of the particle's momentum and p_T is the component of the particle's momentum transverse to the beam direction. The total transverse energy was evaluated using calorimeter cells with θ>0.1 radians (i.e. excluding the very forward region).

In order to reject the remaining background, a cut was made on y_{hadron}, the value of y calculated by the Jacquet and Blondel method [65] from the hadronic final state, utilising the energy flow information from the calorimeter. This gives

$$y_{hadron} = \sum_{j=1}^{\#hadrons} \frac{(E_j - p_{zj})}{2E_e}$$

where E_j and p_{zj} are the energy and z-component of momentum for hadron j and E_e is the energy of the incoming beam electron. This method is insensitive to losses down the beam pipe. For real photoproduction events, the value of y_{hadron} calculated by this method should agree with that calculated from the electron tagger and should at least lie within the electron tagger acceptance.

Figure 6.4 (a) shows the distribution of y_{hadron} for the data, 6.4(b) for the Monte Carlo. The data distribution was found to have a peak in the region 0.0 to 0.1 which was absent from the Monte Carlo. However, the distribution for the proton pilot bunch events, shown in figure 6.4(c), showed a sharp peak below 0.1. This suggested that the peak in data was due to contamination from events with an interaction in the centre of H1 similar to those induced by the proton pilot bunch. Figures 6.5 (a) and (b) show that the values of y calculated from the hadronic information and from the electron information are correlated for both data and Monte Carlo.

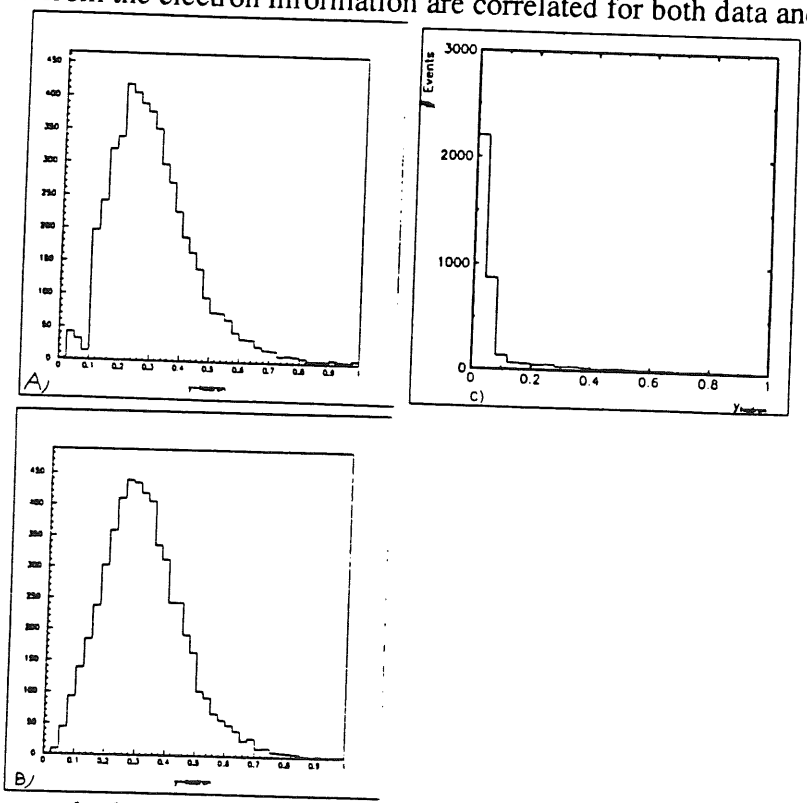

Figure 6.4: y_{hadron} calculated by the Jacquet-Blondel method before applying cuts for a) data, b) GRV Monte Carlo, c) Proton pilot bunch.

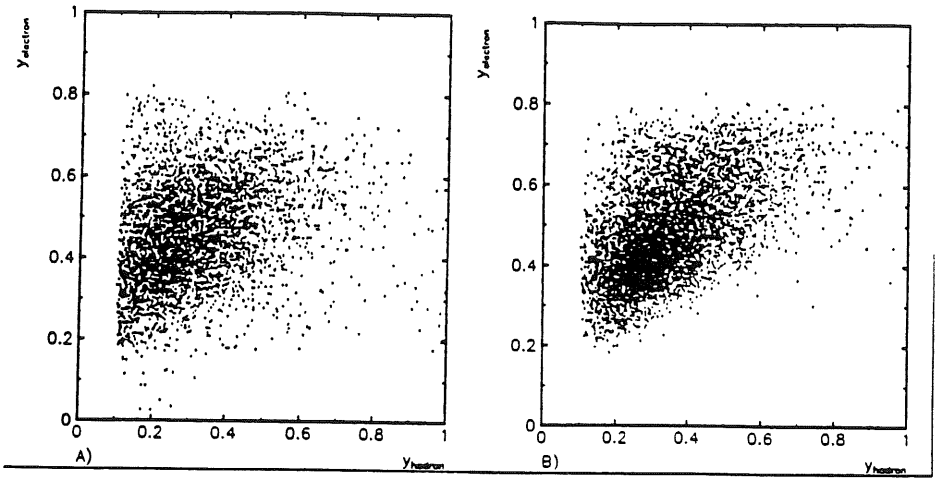

Figure 6.5: correlation plot of $y_{electron}$ against y_{hadron} after mini-DST selection (y_{hadron}>0.1) for a) data, b) GRV Monte Carlo.

When producing the pre-selection it was insisted that y_{hadron}>0.1. Only those calorimeter cells at θ>0.1 radians were used in calculating the value of y_{hadron} in order to avoid possible problems from including part of the proton remnant in the measurement. The peak below 0.1 in the pilot bunch data contained 3084 events (78.1±0.6% of the total). By scaling this peak to the 90 events below 0.1 in the data the total number of proton beam induced background events in the data sample was estimated to be 115.2±17.8 events.

This cut was tightened for this analysis by insisting that y_{hadron}>0.2, calculated using all calorimeter information (i.e. no θ requirement). Imposing this cut, 367 pilot bunch events remained out of 3949 (9.3±0.4%). Imposing the y_{hadron}>0.2 cut resulted in an estimated 10.7±1.7 proton beam induced background events. It was not clear whether these events were distributed in z in the same way as the proton pilot bunch events as the acceptance varies with z. If they were, the z_{vertex} cut would reduce the background by a further 50% to 5.4±0.9 events. No further attempt was made to treat the remaining background in the sample.

After imposition of these cuts, 4354 events remained from the pre-selection, compared with predictions of 5957 events from the GRV Monte Carlo and 10915 events from the LACIII reweighted Monte Carlo.

The Jet Finding Algorithm

In order to examine the properties of the photon remnant, events with two jets from the hard scattering process were selected to ensure clean event identification. The jet algorithm used was the LUCELL cone algorithm [66]. This algorithm uses pseudo-rapidity, η, defined as

$$\eta = -\ln\left(\tan\frac{\theta}{2}\right)$$

where θ is the angle between the particle's momentum vector and the proton beam direction. This is an approximation to rapidity, j, which is given by

$$j = \frac{1}{2}\ln\left(\frac{E + p_z}{E - p_z}\right)$$

for a particle with energy E and z-component of momentum p_z. Intervals in both rapidity and ϕ are invariant under boosts along the beam axis.

A grid was defined in η–ϕ space which was then filled with the transverse energy information from the calorimeters. The grid used had 24 cells in ϕ and 25 in η, in the range $-2.5 < \eta < 2.5$. A search was made for an initiator cell with a transverse energy, E_T, of $E_{Tini} \geq 0.2$ GeV. All cells satisfying this cut, starting with the cell with the highest E_T, were then used as the centre of a cone of radius R = 1.0. If the transverse energy within this cone was greater than a threshold, E_{Tmin}, of 5.0 GeV the cone was accepted as a jet.

Only events with at least two jets defined in this way were accepted for further study. Figure 6.6 shows the fraction of events found with zero, one, two, three and four jets for the data, GRV Monte Carlo and LACIII reweighted Monte Carlo samples.

	Data	GRV	LACIII
Zero Jets	64.8±0.7%	68.7±0.6%	62.6±0.6%
One Jet	24.4±0.7%	26.6±0.6%	30.7±0.6%
Two Jets	8.7±0.4%	4.1±0.3%	5.7±0.3%
Three Jets	1.8±0.2%	0.5±0.1%	0.9±0.1%
Four Jets	0.3±0.1%	0.1±0.1%	0.1±0.1%

Figure 6.6: Fraction of events with zero, one, two, three and four jets in the data, GRV Monte Carlo and LACIII reweighted Monte Carlo samples.

A total of 467 data events remained after this selection. The summed weight of GRV Monte Carlo events remaining was 2836.9, corresponding to 277 events. The weight remaining in the LACIII reweighted Monte Carlo was 7470.3 corresponding to 728 events. Hence, the fraction of two jet events was found to be higher in the data than in either of the Monte Carlo predictions. The absolute predictions for the number of events were found to bracket the data, the GRV predicting fewer events and the LACIII predicting more. With the low value of E_{Tmin} chosen, the presence of noise may have been a significant factor in raising jet energies above threshold. However, a low threshold was necessary in order to find a significant number of two jet events with the small integrated luminosity available. The number of jets was also increased by a difference in forward energy flow between the data and Monte Carlo. This is discussed in the section entitled 'Differences In Energy Flow In The Forward Region Between Data And Monte Carlo Predictions'.

Having established the difference in the number of events after cuts in data and the two Monte Carlo predictions, it is useful to compare the shapes of the predicted distributions with the observed shapes. In order to do this, the area under the histograms for data and Monte Carlo were equated. The value of the area under the histogram chosen for this equalisation was 1.0 and distributions treated in this way will be referred to as 'normalised to 1.0'.

A plot of the transverse energy flow with respect to the highest E_T found in the event

was then made in order to confirm that the events selected had a genuine back-to-back structure. For each calorimeter cell in the event, a histogram entry was made at $\Delta\phi$, the difference in ϕ between the cell and the cell with the highest E_T. This entry was given a weight equal to the E_T of the cell. The plot was then normalised to 1.0 for comparison with Monte Carlo prediction. The resulting plot is shown in figure 6.7(a) and figure 6.7(b) shows a similar plot compiled using central tracks (relative to the highest E_T track). It was concluded that the events selected by LUCELL as having two jets had a clear back-to-back structure for both data and Monte Carlo.

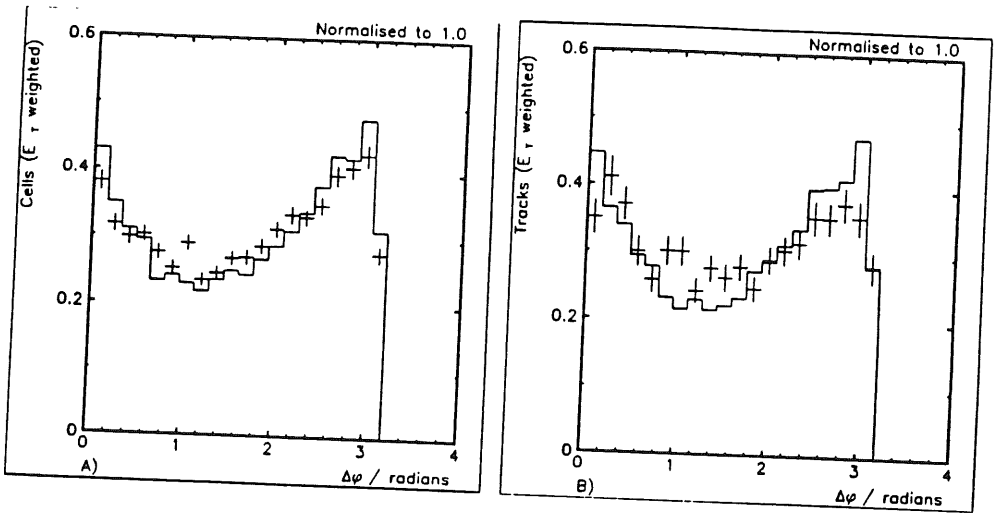

Figure 6.7: Transverse Energy flow in ϕ with respect to the highest transverse energy in the event a) for calorimeter cells, b) for central tracks. Points are data, solid histogram is GRV Monte Carlo prediction.

After jet finding, the shapes of the distributions of electron tagger energy E_{etag}, y calculated from the electron $y_{electron}$, y_{hadron} and z_{vertex} were examined (shown in figures 6.8(a), (b), (c) and (d) respectively) in order to ensure that different biases had not been introduced into the data and Monte Carlo samples. The shapes of the electron tagger energy distributions were found to be similar although the data distribution had a longer tail at higher energies. The shapes were observe to differ less in figure 6.8 than in figure 6.2, where the trigger requirement had not

been imposed on the Monte Carlo sample. The $y_{electron}$ distribution was found to have a tail at low values which corresponded to the tail at high electron tagger energies. The data distribution was found to peak at a lower value of y_{hadron} than the Monte Carlo. The shapes of the data and Monte Carlo z_{vertex} distributions were found to be in good agreement.

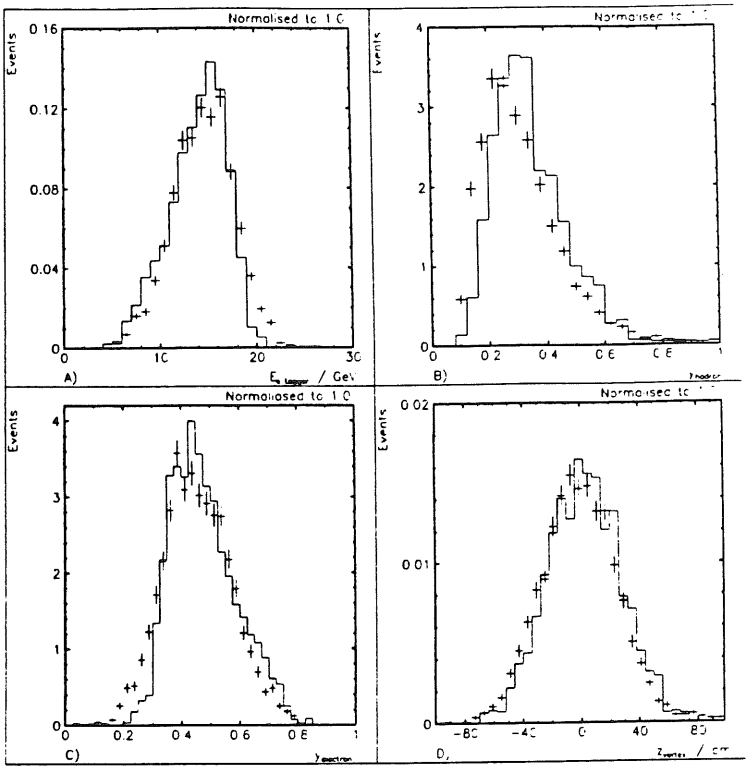

Figure 6.8: Distribution for the two-jet event samples in a) electron tagger energy, b) y_{hadron}, c) $y_{electron}$ and d) position of primary reconstructed vertex in z. Points are data, solid histogram is GRV Monte Carlo prediction.

Comparisons Between Data And Monte Carlo

A) Charged Track Distributions

Figures 6.9(a), (b), (c) and (d) show the E, η, ϕ and p_T distributions respectively of charged tracks in the central tracking detector from the two-jet data and Monte Carlo samples. The shapes of data and Monte Carlo were found to agree well in E and p_T. The data was found to have a peak in the region $1<\eta<2$ which was not predicted by the Monte Carlo. This difference is not fully understood at the present time. A full discussion of this effect and other related problems will be given in the section entitled 'Differences In Energy Flow In The Forward Region Between Data And Monte Carlo Predictions'. The data distribution was also found to have a dip in the region $-3.1<\phi<-2.2$ which was not predicted by the Monte Carlo. This dip was caused by dead sectors in the central jet chamber which were not correctly treated in the Monte Carlo simulations. Further studies could ensure that these sectors are made dead for the same fraction of events as in the data.

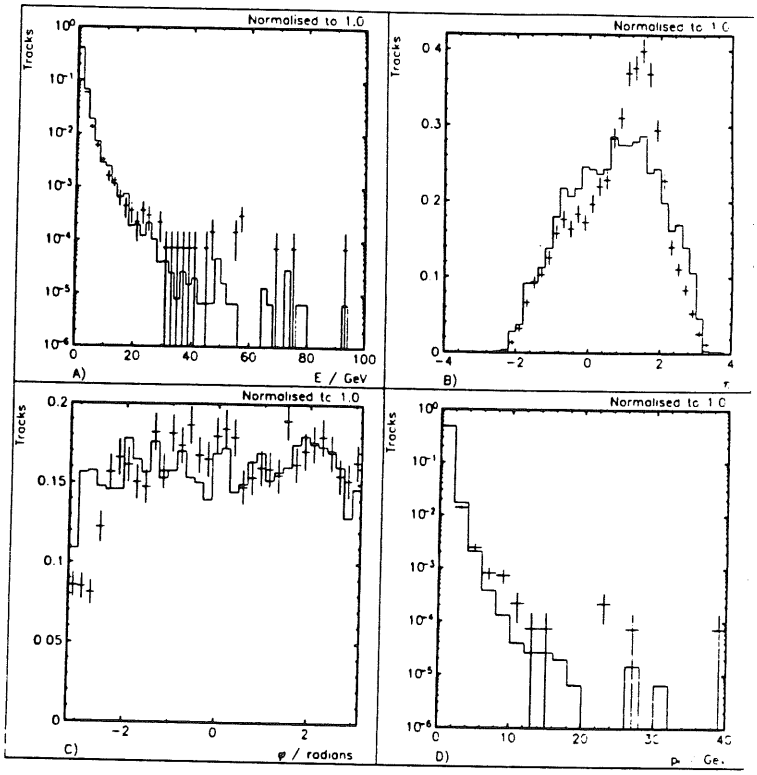

Figure 6.9: Number of charged tracks (normalised to 1.0) in the central detector as a function of a) track energy, b) track pseudo-rapidity, c) track ϕ, d) track transverse momentum. Points are data, solid histogram is GRV Monte Carlo prediction.

B) Jet Distributions

The E, η, ϕ and p_T distributions of the jets were examined for the reconstructed jets, as shown in figures 6.10(a)-(d) (normalised to 1.0) and in figures 6.11(a)-(d) (with absolute normalisation). The shapes of the ϕ and p_T distributions were found to agree well. A peak was observed in the E distribution for the data around 25 GeV which was not present in the Monte Carlo. A caveat should be made regarding jets near the extremes of the η range used ($-2.5<\eta<2.5$) as the truncation of jets may have unpredictable results if the jet shapes in data and Monte Carlo differ. However, even taking this into consideration, the shape of the data η distribution was observed to be different from either of the two Monte Carlo predictions, having a peak in the forward region, $1<\eta<2$.

Figure 6.12 shows that the jets in the E peak (i.e. with 16 GeV $< E <$ 24 GeV) lie predominantly in the η peak also. The presence of these jets is thought to be related to the effects observed in the charged track distributions and will be discussed later.

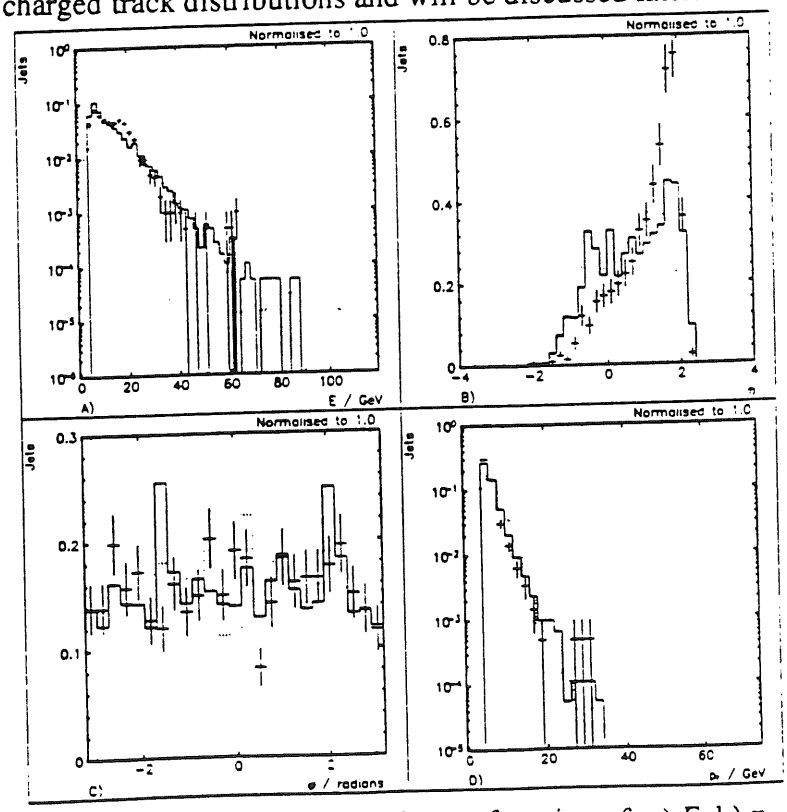

Figure 6.10: Number of jets (normalised to 1.0) as a function of a) E, b) η, c) ϕ and d) p_T. Points are data, solid histogram is GRV Monte Carlo prediction, dotted histogram is LACIII reweighted Monte Carlo prediction.

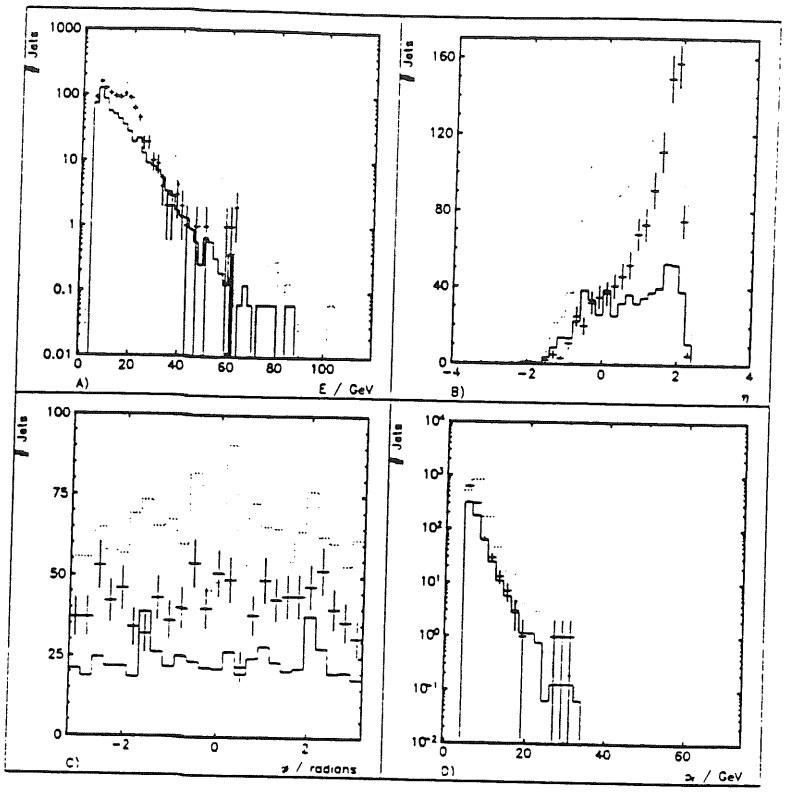

Figure 6.11: Number of jets (absolute normalisation) as a function of a) E, b) η c) ϕ and d) p_T. Points are data, solid histogram is GRV Monte Carlo prediction, dotted histogram is LACIII reweighted Monte Carlo prediction.

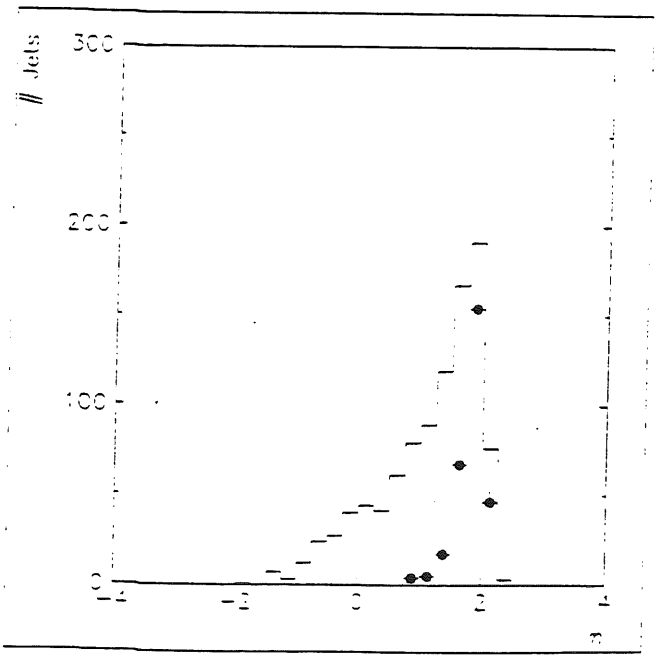

Figure 6.12: Number of jets as a function of η for all jets in the data (solid histogram) and those jets with energies in the range 16 GeV < E < 24 GeV (points).

C) Jet Profiles

A jet profile is defined as the distribution of E_T with respect to the centre of the jet. These profiles were compiled by considering all tracks or calorimeter cells within the jet and making an entry in the profile histogram at the appropriate position, weighted by the E_T of the track or cell. The distributions were then normalised to 1.0 for shape comparison. Figure 6.13(a) shows the jet profile using calorimeter cells in $\Delta\eta$, the difference between the cell η and the η of the centre of the jet. Both the data and Monte Carlo jets were found to be centred at zero, but the data distribution was seen to be broader than the Monte Carlo prediction. The data distribution was also found to contain more transverse energy in the forward ($\Delta\eta$ positive) jet tail than in the negative jet tail.

This effect has also been reported in an H1 paper [64], where it was found that the effect was observed for jets in the region $0.5<\eta<1.5$ but not for those in the range $-1.5<\eta<0.5$. The contribution was found to be almost independent of jet energy but to rise with the jet η. The jet studies in [64] used a sliding-window algorithm requiring $E_T>7.0$ GeV rather than LUCELL to find jets. However, as the cone size used was R=1.0, the results are expected to be applicable to jets found with LUCELL. The majority of the jets found in this study were observed to lie in the forward region, so the observed difference in jet profiles between data and Monte Carlo is consistent with that reported in the paper. This effect will be discussed more fully in the next section. Figure 6.13(b) shows the jet profile from calorimeter cells in $\Delta\phi$, the difference between the ϕ of the cell and the ϕ of the centre of the jet. The data distribution was found to be broader than the Monte Carlo prediction but was symmetric about zero.

The jet profiles were also examined using central tracks. As shown in figures 6.13 (c) and 6.13 (d), the data and Monte Carlo distributions were found to be in agreement within errors for both η and ϕ. The large errors on some points in these distributions resulted from the inclusion of a small number of tracks with high E_T.

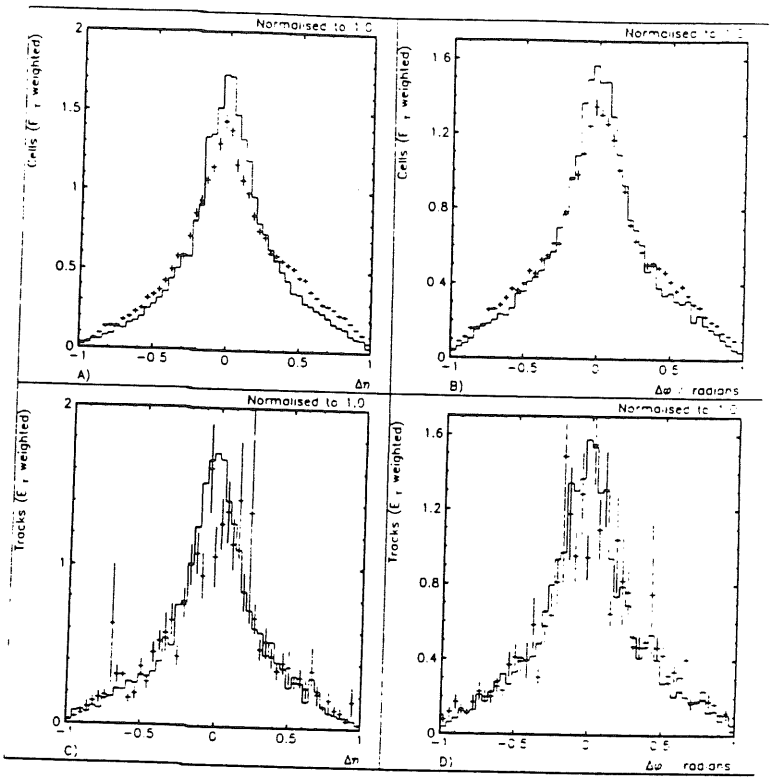

Figure 6.13: Jet transverse energy profiles, normalised to 1.0, for a) calorimeter cells in η, b) calorimeter cells in ϕ, c) central tracks in η and d) central tracks in ϕ. Points are data, solid histogram is GRV Monte Carlo prediction.

Differences In Energy Flow In The Forward Region Between Data And Monte Carlo Predictions.

As described above, significant differences were found between the data and the PYTHIA Monte Carlo distributions using either the GRV or LACIII photon structure function parameterisations. These difference were:

1) That a higher fraction of the data events had two or more jets than predicted by the Monte Carlo.

2) That more tracks were observed in the forward region, $\eta>1$, for data than for Monte Carlo.

3) That more jets were found in the forward region for data than for Monte Carlo.

4) That the jet tails showed an excess of energy in the forward region over that predicted by the Monte Carlo shape. This effect has also been reported in an H1 paper [64].

If the last difference were not observed, a modification of the structure function parameterisation might be able to account for the differences. However, the difference in the jet tails may not be easily explained by making such a modification. It is currently thought that there is more energy in the forward region in data than is predicted by Monte Carlo and that this energy is spread evenly in ϕ within each event ([67] and [68]). This presents a serious problem.

Consider a jet with 4.5 GeV of transverse energy. If this jet were to be scattered into the barrel region, the reconstructed transverse energy would only be 4.5 GeV and the jet would therefore not be tagged by LUCELL. However, if the jet were to be scattered into the forward region, the transverse energy in the LUCELL cone would be the sum of the jet transverse energy and whatever 'extra' transverse energy is present from the evenly-distributed energy flow. If this energy were large enough, the reconstructed transverse energy would be raised above the 5 GeV threshold. This would mean that the jet would now be identified by LUCELL. Therefore, the presence of such energy would result in a larger number of jets being identified in the forward region for data than was predicted by Monte Carlo, despite agreement in the backwards region. This explanation fits the observations described above.

The only way to disentangle the difference in jet rates arising from an inaccurate

structure function parameterisation from a difference in jet rates caused by this threshold effect is to understand and correctly reproduce the energy flow in the forward region. It is currently suggested that, as the data and Monte Carlo distributions match well except for $\eta>1$, there is some physical effect spraying extra particles into the forward part of the detector. However, this has not yet been substantiated. Therefore, any conclusions regarding energy flow, jet rates and photon structure function parameterisations must be treated with a degree of caution, especially in this forward region.

Work is in progress at DESY to understand this effect using both the 1992 data and the new 1993 data for which the forward tracker is fully operational and well reconstructed. Several possibilities are being explored, including:

1) That the model used thus far of one hard scatter per event may be inadequate and that the possibility of multiple partonic interactions occurring in the same event may have to be considered [69]. Preliminary studies [70] indicate that such models may be able to explain the effect.

2) That the fragmentation model used thus far, JETSET [71], may be inappropriate or improperly tuned. Studies are also in progress using the HERWIG [72] and ARIADNE [73] models to investigate the effects of the fragmentation model on the Monte Carlo predictions.

3) That there may be some instrumental or experimental effect spraying particles into the forward region. For example, some dead material around the beam-pipe may be absent or wrongly described in the simulation program.

4) The fragmentation of the proton remnant may not be correctly described by PYTHIA. This may result in the fragments of the proton being spread over a wider range in η than in the Monte Carlo prediction, thus supplying the extra energy.

The x_γ Distribution

The value of x_γ may be calculated from the reconstructed parameters of the two jets using the method described in appendix A. If both jets are in the forward region, $\eta>1$, a low value of x_γ results. The distribution of x_γ obtained by using the jet information with absolute normalisation is shown in figure 6.14(a) and normalised to 1.0 in figure 6.14(b). Although the GRV Monte Carlo prediction was observed to be in agreement with the data above x_γ=0.3, the data distribution was found to have a pronounced peak at lower values of x_γ. This was expected given the difference between the data and Monte Carlo jet η distributions. The LACIII reweighted prediction was found to be significantly higher than the data for $x_\gamma>0.3$ and also did not show a peak at lower values of x_γ. Both Monte Carlo predictions showed a peak at x_γ=0.6 which was not seen in the data. Inspection of the Monte Carlo events led to the conclusion that this peak was due to three events with high weights, illustrating the problem caused by the correlation in statistical fluctuations when reweighting the Monte Carlo events.

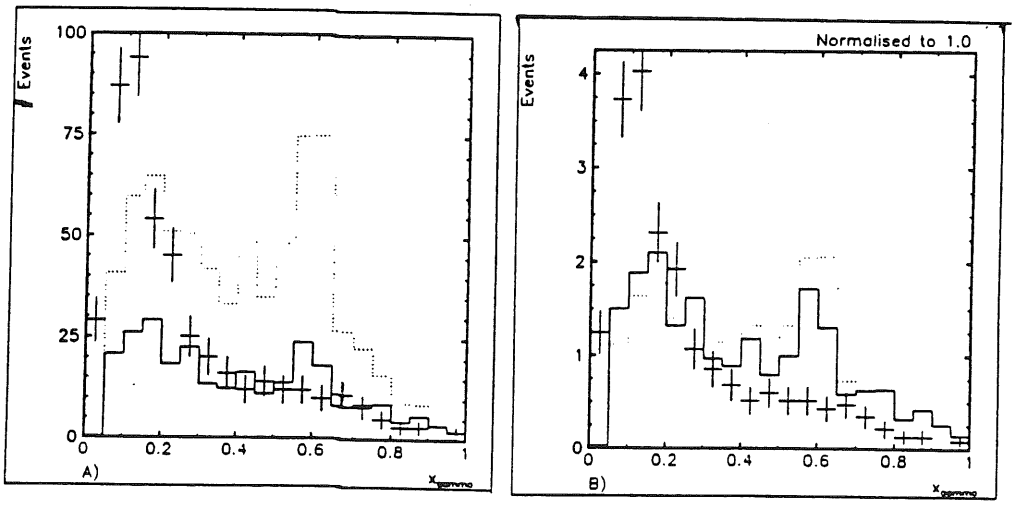

Figure 6.14: Number of events as a function of x_γ calculated from jets, a) absolute normalisation, b) normalised to integral 1.0. Points are data, solid histogram is GRV Monte Carlo prediction, dotted histogram is LACIII reweighted Monte Carlo prediction.

Photon Remnant Algorithm

Using the LUCELL algorithm for jet finding, some of the energy deposited in the calorimeter is tagged as coming from the hard scattered partons. The remaining energy in the event must have come from somewhere, so an algorithm to collect the rest of the cells should in principle give the sum of the photon and proton remnants. However, the radius R = 1.0 described in the Jet Finding section may not fully contain the jets and jet tails, noisy cells and pedestals under the jets may also contribute to energy outside the jet cones. Therefore, a limited range of η-ϕ space should be summed to define the photon remnant. As the photon remnant is predicted to be mostly in the backward region and the proton remnant mostly in the forward region, separation of the two remnants should be possible.

The first study of this kind of collection algorithm was carried out by D'Agostini and Monaldi on Monte Carlo datasets [74]. This work examined the possibility of using the amount of energy in a cone one unit in η behind the backwards-most jet as a discrimination between resolved and direct events. D'Agostini and Monaldi found that good discrimination should be possible by searching for at least 3 GeV of energy in this backwards cone. One approach to finding the photon remnant is therefore to sum all particles in this cone and examine the properties of the entity so formed. The region η–ϕ space summed by this algorithm is illustrated in figure 6.15. This algorithm will be referred to as the D/M algorithm, although they only used it to discriminate between direct and resolved events rather than to define the remnant.

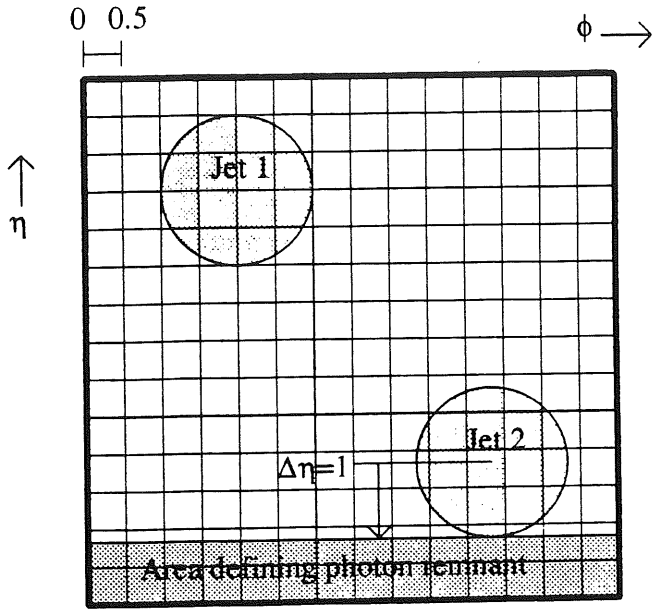

Figure 6.15: The D/M algorithm for defining the photon remnant based on the cone defined by $\Delta\eta=1$.

This algorithm has the advantage of not assuming the presence of a photon remnant in order to find it. Alternative algorithms based on event decomposition may not be used to simply demonstrate the existence of a photon remnant because such routines are always controlled by a cut-off parameter which limits the level of decomposition. The presence of a remnant does not depend on any such arbitrary parameter and it is therefore advantageous to use a simpler algorithm in this initial study to demonstrate the existence of the remnant.

Such an algorithm has the disadvantage of only catching the remnant when it is within this $\Delta\eta=1$ cone and there is no reason to suppose that the remnant is always fully contained within this area. In addition to examining the data with the D/M algorithm, a broader algorithm was devised to find the photon remnant when it is not contained entirely behind the backwards-most jet. The algorithm chosen is shown pictorially in figure 6.16.

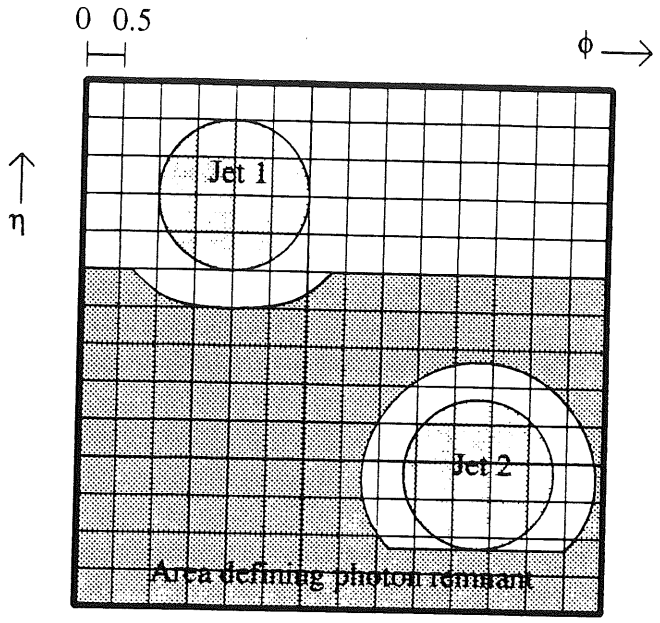

Figure 6.16: The alternative ('new') collection algorithm for defining the photon remnant.

The area included in this second algorithm is defined by the following criteria:

1) Anything at least one unit in η behind the backward most jet is included.

2) Anything at least one unit in η behind the forward most jet and at least a distance $\Delta R=1.5$ units from the centre of the nearest jet.

This algorithm has the advantage of being able to pick up the photon remnant when it is well separated in ϕ from the backward most jet but is at a similar value of η. However, as the area included is larger than for the first algorithm the problems arising from the inclusion of noise and jet tails are expected to be more severe than for the first algorithm. A further problem with both of these algorithms is that the remnant may be identified as a jet if it fulfils the jet finding criterion of $E_T>5$ GeV in a cone of radius 1.0. The performance of the algorithm on Monte Carlo simulations of the photon remnant may be used to assess the severity of these problems. However, the Monte Carlo predictions for the photon remnant must be compared with the data to ensure that such a study is meaningful. As the Monte Carlo generator used had been tuned primarily for proton-anti-proton collisions rather than electron-proton collisions, some differences are expected.

Photon Remnant Results

A) Fraction Of Events With A Photon Remnant

In data, using the D/M algorithm, a photon remnant was found in 367 out of 467 two jet events, (79±2%). In the GRV Monte Carlo, the fraction of those events with a found remnant was 65±1%. In the LACIII reweighted Monte Carlo, the fraction of events with a found remnant was 62±1%. For the new algorithm, the percentages were 96±1% for data, 88±1% for the GRV Monte Carlo and 90±1% for the LACIII Monte Carlo. It was therefore concluded that a substantial fraction of the photoproduction events collected had a remnant present and that this was indicative that a large fraction of the events were resolved, as theoretically predicted.

A greater fraction of events in the data were found to have a remnant present than in the Monte Carlo. However, the presence of a remnant is expected to be very sensitive to the presence of noisy cells and particles not assigned to a jet as one cell above the noise threshold anywhere in the $\eta-\phi$ region considered by the algorithm is sufficient to tag the event as having a remnant. This explains why a larger fraction of events were found to have a remnant when using the new algorithm as it considers an increased area of $\eta-\phi$ space and therefore there is a greater chance of using cells above threshold.

For the Monte Carlo samples, the possibility of using the presence of a remnant to discriminate between direct and resolved processes was examined. Figure 6.17 shows the percentage of events with and without a remnant for direct and resolved processes in the GRV and LACIII reweighted samples. The error on the percentages was estimated as ±2% based on the number of events. For the D/M algorithm, it was found that a reasonable discrimination was achievable based on the detection or non-detection of a photon remnant. With the new algorithm, which includes a much larger area in $\eta-\phi$ space, the discrimination was found to be poor.

For the reasons discussed above, the presence of a remnant is very sensitive to any deposition of energy from whatever source. Therefore, an energy requirement on the reconstructed remnant was imposed in order to improve the discrimination. This was the approach followed by D'Agostini and Monaldi, who required at least 3 GeV in the cone defined

by $\Delta\eta$=1 to tag an event as resolved. The fraction of events with and without a remnant of at least 3 GeV is shown in figure 6.18, again with estimated ±2% errors from the number of events.

	D/M GRV	D/M LAC	New GRV	New LAC
Resolved With	70.4%	63.9%	90.8%	90.8%
Resolved Without	29.6%	36.1%	9.2%	9.2%
Direct With	18.4%	18.4%	64.6%	64.6%
Direct Without	81.6%	81.6%	35.4%	35.4%

Figure 6.17: Percentage of direct and resolved events with and without a photon remnant as defined by the D/M and new algorithms for GRV and LACIII reweighted Monte Carlo, requiring only the presence of a remnant jet.

	D/M GRV	D/M LAC	New GRV	New LAC
Resolved With	46.7%	38.3%	61.6%	55.8%
Resolved Without	53.3%	61.7%	38.4%	44.2%
Direct With	5.9%	5.9%	44.0%	44.0%
Direct Without	94.1%	94.1%	66.0%	66.0%

Figure 6.18: Percentage of direct and resolved events with and without a photon remnant as defined by the D/M and new algorithms for GRV and LACIII reweighted Monte Carlo, requiring at least 3 GeV of energy in the found remnant.

The D/M method for discriminating between direct and resolved events was observed to perform well, discarding most of the direct events while accepting most of the resolved events. Imposing a cut of 3 GeV on the remnant energy improved the rejection of direct events to almost 95% but reduced the acceptance for resolved events to less than 50%. The new algorithm was found to be less useful in discrimination as the difference between the acceptances for direct and resolved events was not as large as for the D/M algorithm. This was due to the inclusion of more noisy cells when defining the remnant. Either algorithm could be used to provide an enriched sample of resolved events but neither could reliably be used to extract a sample of direct events based on the absence of a remnant, even with an energy cut of 3 GeV.

The fraction of two-jet events in the data with a remnant of energy of at least 3 GeV was 55±2%, compared with 42±2% for the GRV Monte Carlo and 37±2% for the LACIII reweighted Monte Carlo. With the new remnant algorithm, the fractions became 69±2% for data, 60±2% for GRV and 55±2% for LACIII. The data were observed to have larger fraction of events with a remnant than the Monte Carlo predictions, even when the 3 GeV energy requirement was imposed.

B) Photon Remnant Distributions

The distributions of the photon remnant were examined for both the D/M and new algorithms. Figures 6.19(a)-(d) show the distributions with E, η, ϕ and p_T respectively for the D/M algorithm, normalised to 1.0, figures 6.20(a)-(d) with absolute normalisation. Figures 6.21(a)-(d) and 6.22(a)-(d) show the distributions for the new algorithm with normalisation 1.0 and absolute normalisation respectively. With the D/M algorithm, good agreement between the shapes of the data and Monte Carlo E distributions was observed and reasonable agreement was found in η and ϕ. The data distribution was found have a larger fraction of events with $\eta>0.0$ than predicted by the Monte Carlo. A peak was found at $\phi=2.5$ in the Monte Carlo distributions but investigation revealed that this was due to one event with high Monte Carlo weight. The data and Monte Carlo p_T distributions were found to agree in the region $p_T>2$ GeV but below this the data distribution was found to be peaked whereas the Monte Carlo prediction fell smoothly.

With the new algorithm, the Monte Carlo predictions for the shapes of the distributions in E, η, ϕ and p_T were found to be in agreement with the data. The single event with high Monte Carlo weight that had given a peak at $\phi=2.5$ with the D/M algorithm was reconstructed to have a remnant at $\phi=-2.75$ by the new algorithm, producing a peak at this value.

The distributions for both algorithms fell sharply with p_T and no remnants were observed with $p_T>6.0$ GeV. It was suggested that remnants with higher p_T might have been labelled as jets by LUCELL if the transverse energy of the jet were sufficiently well-collimated as to exceed the 5 GeV threshold in any one cone of radius 1.0 in $\eta-\phi$ space.

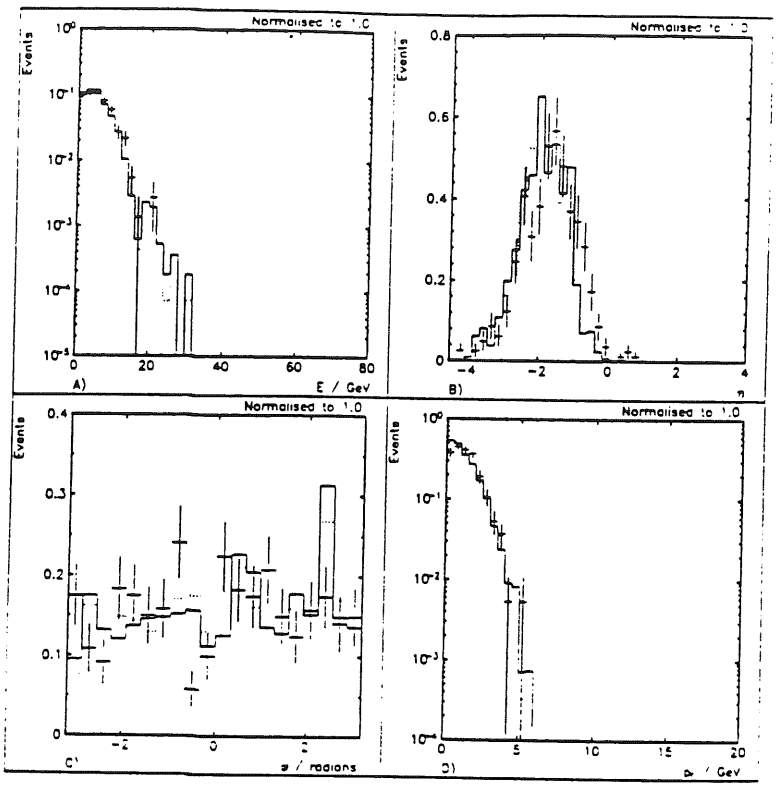

Figure 6.19: Number of photon remnants (normalised to 1.0) defined by D/M algorithm as a function of a) E, b) η, c) ϕ, d) p_T. Points are data, solid histogram is GRV Monte Carlo prediction, dotted histogram is LACIII reweighted Monte Carlo prediction.

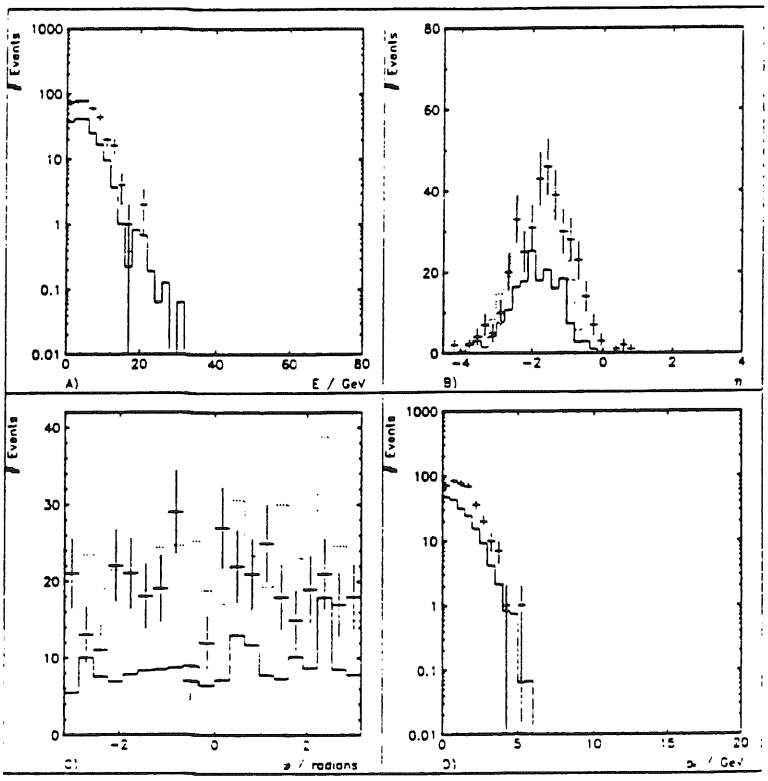

Figure 6.20: Number of photon remnants (absolute normalisation) defined by D/M algorithm as a function of a) E, b) η, c) ϕ, d) p_T. Points are data, solid histogram is GRV Monte Carlo prediction, dotted histogram is LACIII reweighted Monte Carlo prediction.

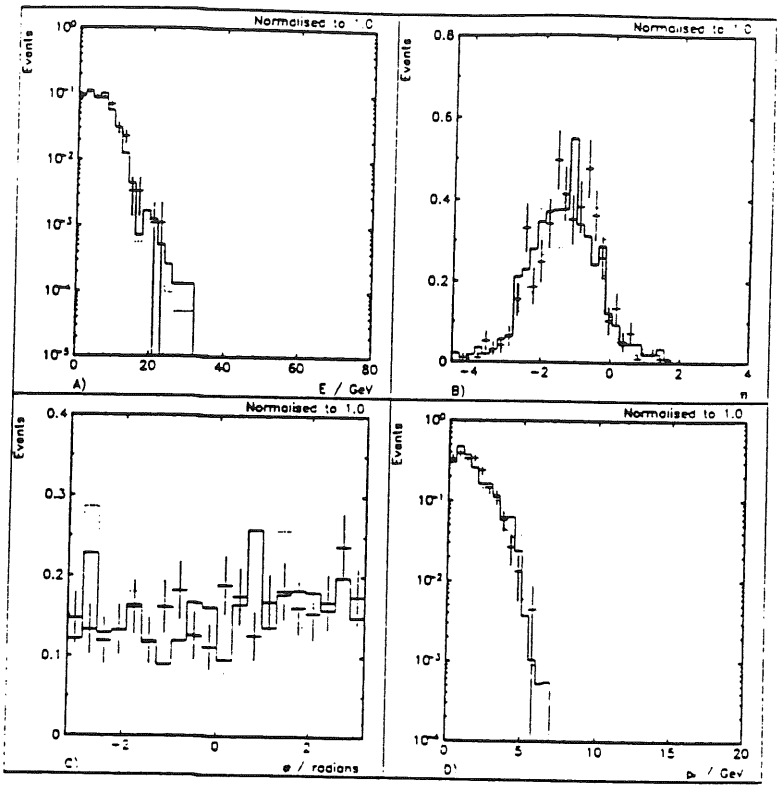

Figure 6.21: Number of photon remnants (normalised to integral 1.0) defined by new algorithm as a function of a) E, b) η, c) ϕ, d) p_T. Points are data, solid histogram is GRV Monte Carlo prediction, dotted histogram is LACIII reweighted Monte Carlo prediction.

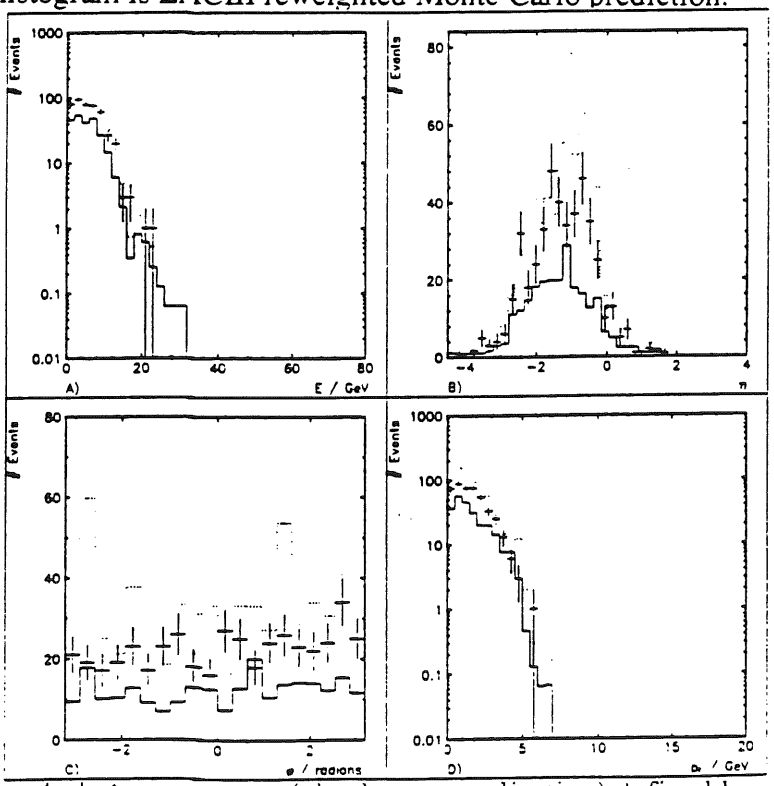

Figure 6.22: Number of photon remnants (absolute normalisation) defined by new algorithm as a function of a) E, b) η, c) ϕ, d) p_T. Points are data, solid histogram is GRV Monte Carlo prediction, dotted histogram is LACIII reweighted Monte Carlo prediction.

C) Photon Remnant Profiles

The transverse energy profiles of the photon remnant in η and ϕ were obtained by the method described in the 'Jet Profile' section. Profiles were obtained using both calorimeter cells and central tracker tracks. Figures 6.23(a)-(d) show the profiles for the D/M algorithm; figures 6.24(a)-(d) for the new algorithm. Good agreement was observed between Monte Carlo predictions and the data profiles.

The observation of peaks in all distributions suggested that concentrations of both calorimeter energy and tracks had been found around the axes of the found remnants, implying the presence of genuine photon remnant jets. The observation of peaks using tracks provided evidence that the found remnants were not due random concentrations of noisy cells in the calorimeter. However, the low track multiplicity in the remnant (discussed in the following section) means that a peaked shape is to be expected when the differences between the directions of the individual tracks are compared with the direction of their four-vector sum.

As described in the 'Jet Profile' section, jets found by LUCELL were observed to be well collimated and were well contained within a cone of radius 1.0 in η–ϕ space. The photon remnants found by both the D/M and new algorithms were found to be less well collimated, which could be due to the lower p_T of the remnants compared with the jets.

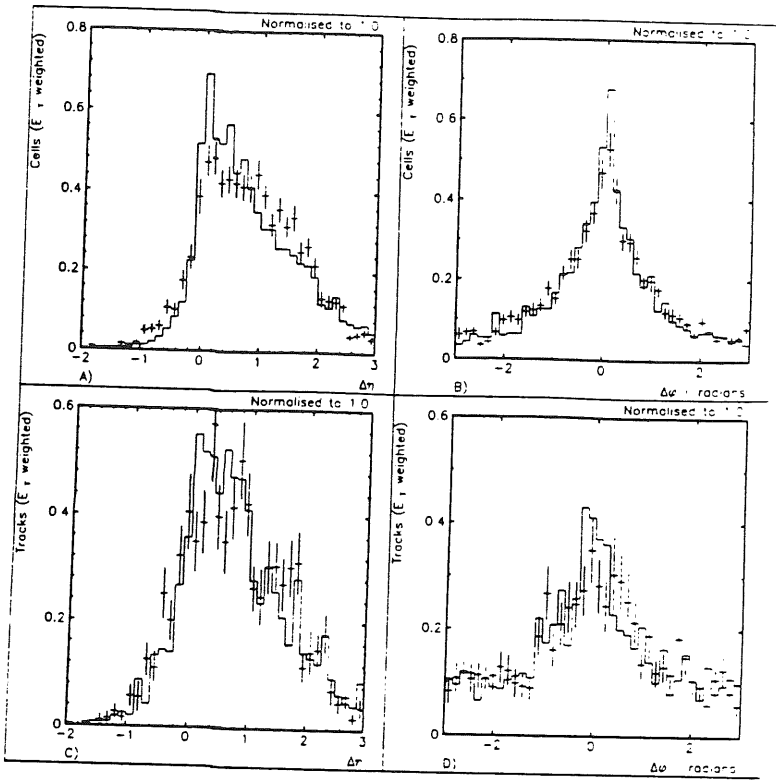

Figure 6.23: Photon remnant transverse energy profiles as defined by D/M algorithm, normalised to 1.0, for a) calorimeter cells in η, b) calorimeter cells in ϕ, c) central tracks in η, d) central tracks in ϕ. Points are data, solid histogram is GRV Monte Carlo prediction.

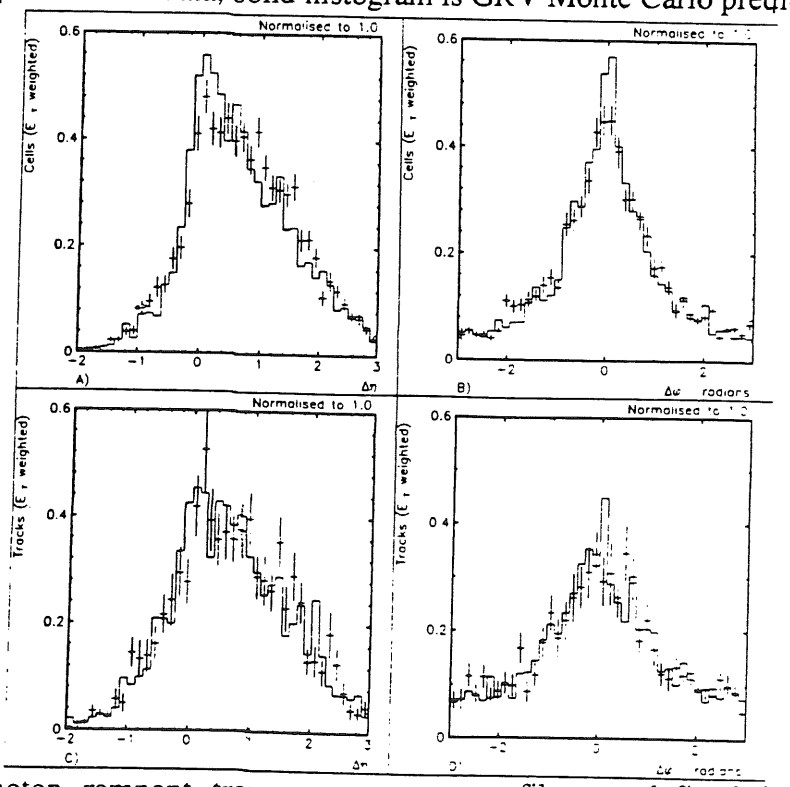

Figure 6.24: Photon remnant transverse energy profiles as defined by new algorithm, normalised to 1.0, for a) calorimeter cells in η, b) calorimeter cells in ϕ, c) central tracks in η, d) central tracks in ϕ. Points are data, solid histogram is GRV Monte Carlo prediction.

D) Distribution Of Tracks Inside The Photon Remnant

The distributions of tracks inside the remnant were found to be in good agreement in η and p_T for the D/M algorithm as shown in figures 6.25(b) and (d) respectively. However, the E distribution for the D/M algorithm (shown in figure 6.25(a)) was observed to fall more rapidly for the data than predicted by Monte Carlo. A dip in the data ϕ distribution, shown in figure 6.25(c), was observed and was found to be due to dead sectors in the central jet chamber, as described in the 'Charged Track Distribution' section. For the new algorithm, good agreement was found in E, η, and p_T, as shown in figures 6.26(a), (b) and (d) respectively. The dip in data ϕ distribution was also observed in the new remnant distribution as shown in figure 6.26(c).

Figure 6.27(a) shows the multiplicity of charged tracks found in the remnant for the D/M algorithm, figure 6.27(b) for the new algorithm. As expected from the larger collection area, the mean multiplicity is higher for the new algorithm than for the D/M. The mean multiplicity is predicted well by the Monte Carlo but the shapes of the distributions differ somewhat.

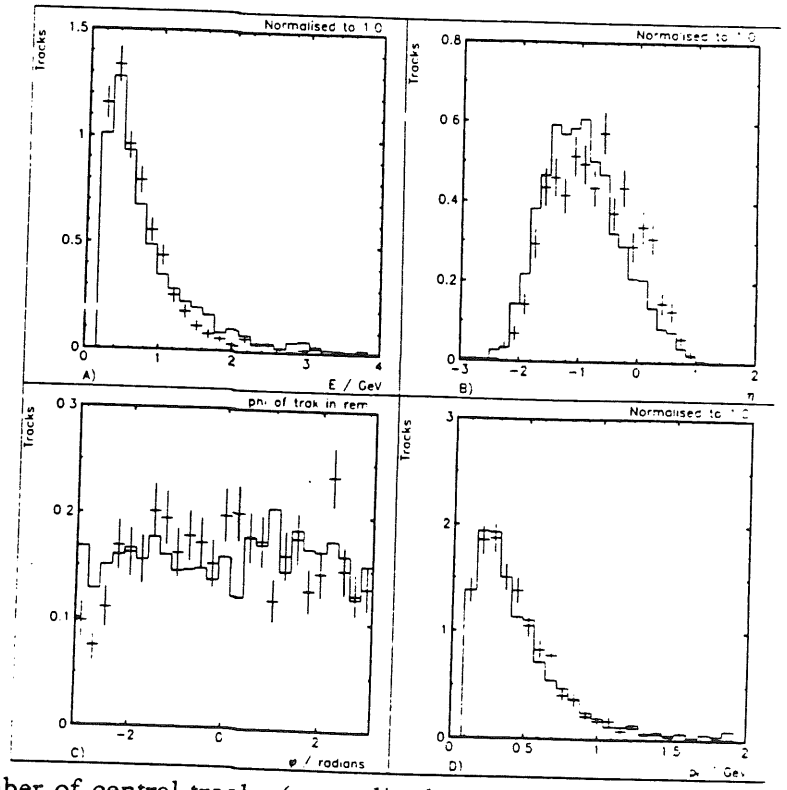

Figure 6.25: Number of central tracks (normalised to 1.0) inside photon remnant as defined by D/M algorithm as a function of a) E, b) η, c) ϕ, d) p_T. Points are data, solid histogram is GRV Monte Carlo prediction.

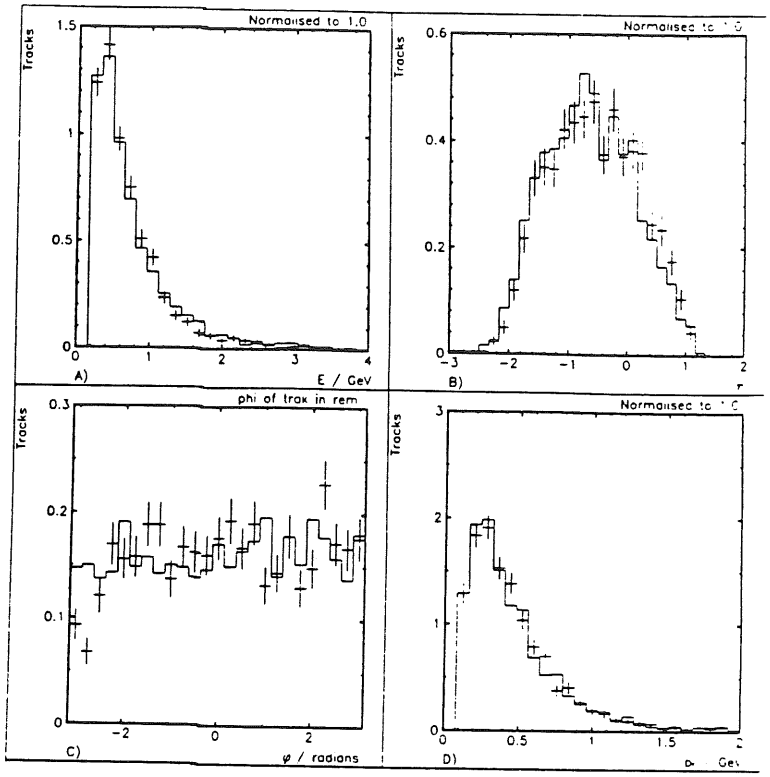

Figure 6.26: Number of central tracks (normalised to 1.0) inside photon remnant as defined by new algorithm as a function of a) E, b) η, c) ϕ, d) p_T. Points are data, solid histogram is GRV Monte Carlo prediction.

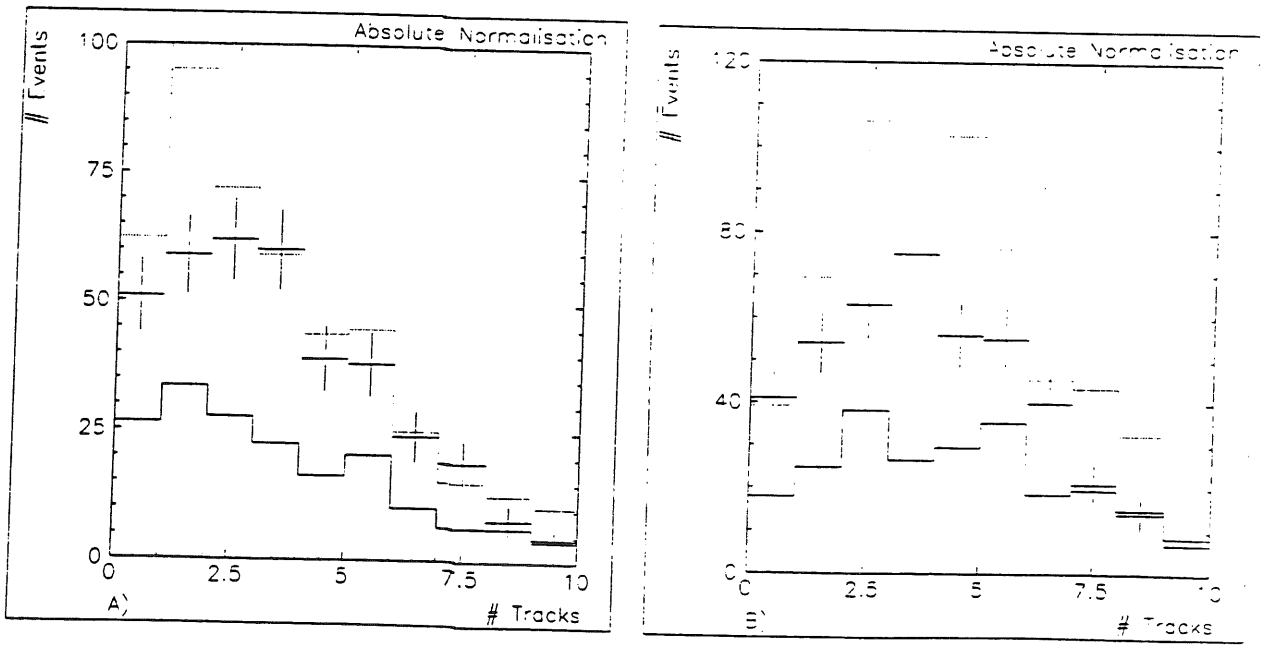

Figure 6.27: Number of charged tracks per event (absolute normalisation) for a) D/M and b) new remnant algorithms. Points are data, solid histogram is GRV Monte Carlo prediction, dotted histogram is LACIII reweighted Monte Carlo prediction.

E) Remnant-Jet Correlations And The $x_\gamma + x_{rem}$ Checksum

Having obtained a reconstructed remnant and a value of x_γ from the reconstructed jets, a check was made to see whether there was any relationship between the two. Plots were made of x_γ against the energy of the reconstructed remnant. The plots for the D/M algorithm are shown in figures 6.28(a) and (b) (for data and Monte Carlo respectively) and for the new algorithm in figures 6.29(a) and (b). As the energy of the remnant varies approximately as $(1-x_\gamma)$, it was expected that the energy of the remnant would be highest when x_γ was lowest. It was concluded from these plots that there was a correlation between the energy of the remnant and value of x_γ. With the D/M algorithm, the distribution for Monte Carlo events seemed to indicate that the events fell along a curve, indicating that some energy was not being reconstructed by the detector. This may be due to excluding particles at the edge of the remnant or to gaps in the calorimeter coverage. The distribution for the new algorithm was found to be more consistent with the expected scatter about a straight line.

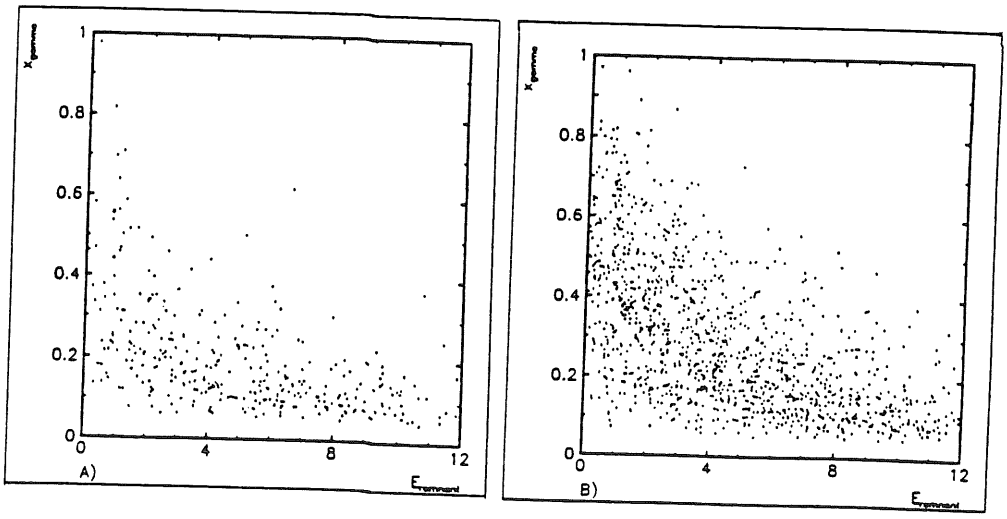

Figure 6.28: x_γ calculated from jets versus energy of photon remnant defined by D/M algorithm for a) data b) GRV Monte Carlo.

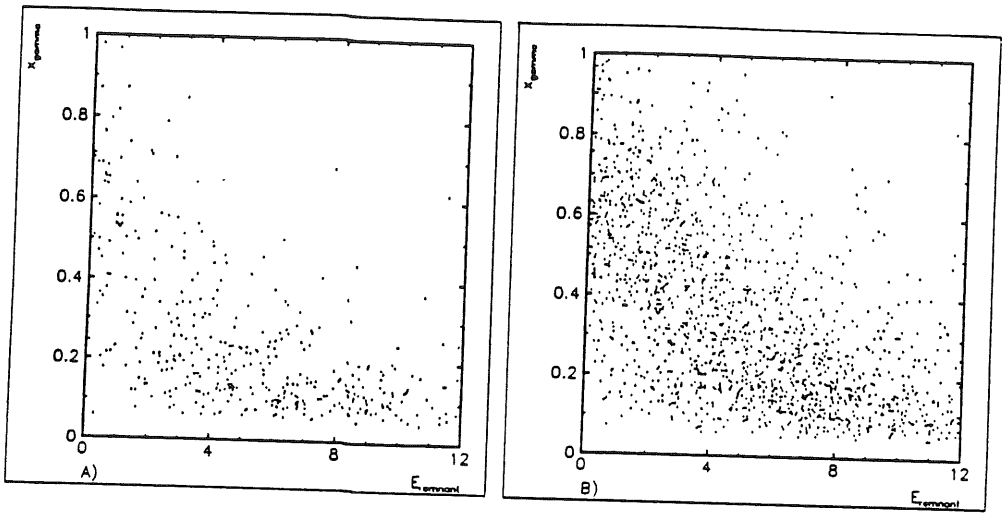

Figure 6.29: x_γ calculated from jets versus energy of photon remnant defined by the new algorithm for a) data b) GRV Monte Carlo.

The checksum $x_\gamma + x_{rem}$ was then plotted using the jet information for x_γ and the remnant information for x_{rem} (as discussed in appendix A). The plot for the D/M algorithm is shown in figure 6.30(a) and the plot for the new algorithm in figure 6.30(b). For the D/M algorithm, the Monte Carlo predictions were in good agreement with the data, with the peak centred in the region 0.5-0.6 and peak widths approximately 0.25 found by the LOOK peak fitter. For the new algorithm, the data peak was centred at 0.68 while the Monte Carlo peaks were centred between 0.7 and 0.8. The peak widths were again found to be approximately 0.25 by the LOOK peak fitter. It was concluded that the rise in the value of the checksum in going to the new remnant algorithm was due to the inclusion of a larger area in $\eta-\phi$ space. It was not clear why the data peak, which agreed for the D/M algorithm, was found to be lower than the Monte Carlo predictions for the new remnant algorithm.

As four-momentum conservation requires $x_\gamma + x_{rem}=1$, the energy in the events does not appear to have been correctly reconstructed. As the formula for x_γ using the jet information is

mainly dependant on the rapidity values of the two jets, missing energy in the jet reconstruction would not be expected to lower the checksum value significantly so long as the jet direction is well reconstructed. The difference between the rapidity and pseudo-rapidity is negligible (approximately 2% for a particle with mass 1 GeV, momentum 10 GeV and θ=20°) and could not account for the shortfall (that is, the shift of the peak from 1.0 to lower values) in the checksum.

Missing energy in the remnant reconstruction would be expected to have a more serious effect and it was suggested that poor backward hadronic calorimetry could be responsible for the shortfall in the checksum. Inclusion of the instrumented iron calorimetry in the region should improve the situation despite the large amount of dead material between the BEMC and iron. An upgrade to the backward calorimetry is also planned.

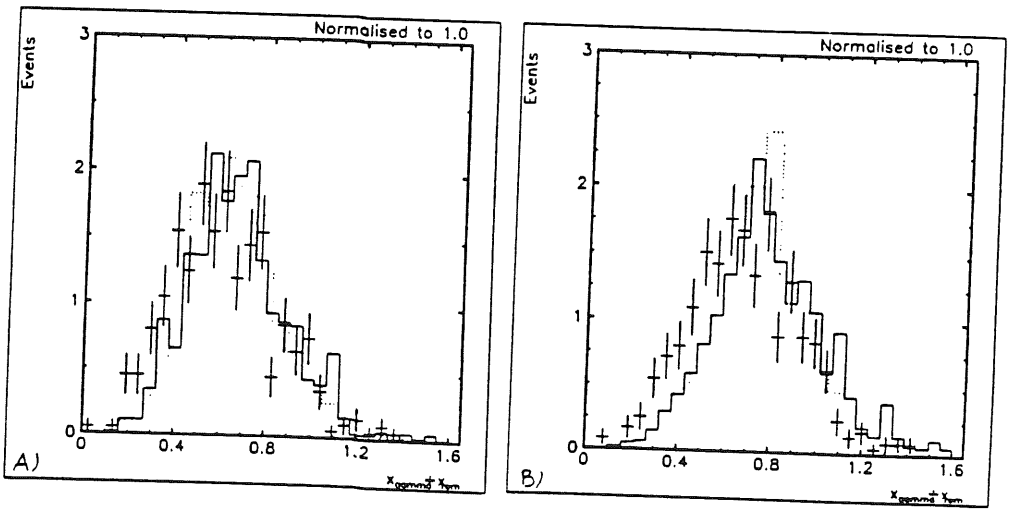

Figure 6.30: x_γ + $x_{remnant}$ checksum for a) D/M b) new algorithms. Points are data, solid histogram is GRV Monte Carlo prediction, dotted histogram is LACIII reweighted Monte Carlo prediction.

Relation to the Parton Level

Because of the difficulty of disentangling the remnant reconstruction and the jet reconstruction when examining the $x_\gamma+x_{rem}$ checksum, a study was made of how well the reconstructed entities represented the parton-level kinematics. In order for this to have any meaning, the Monte Carlo predictions must be in good agreement with the data. As described in preceding sections, the agreement between the Monte Carlo and the data was found to be far from perfect. However, it was concluded that the predictions were at least to the right order of magnitude and that the disagreements were connected with a discrepancy in the energy flow in the forward direction, $\eta>1.0$. The studies were therefore carried out, but a caveat must be made that they were made using an imperfect Monte Carlo and any conclusions drawn from them must be treated with caution.

A problem when comparing partons with reconstructed entities is how to relate the two. One way of doing this would be to go through and check all the mother-daughter relationships. However, this may introduce some problems as it is not known a priori which entity corresponds to which parton in the data. Therefore, the same method of mapping the found entities back to the parton level must be used based purely on the reconstructed information. In this study, the two jets with the highest E_T were assigned to the two partons that hard scattered. Any other jets in the event were neglected and the photon remnant was then reconstructed from the energy not contained in any of the jets. This was then assigned to the photon remnant at the parton level. In order to be consistent, the same mapping was used when comparing the reconstructed Monte Carlo events with the parton level. The only additional information used was that the two highest E_T jets were assigned to the individual hard scattered partons on the basis of closeness in $\eta-\phi$ space.

In order to check that the reconstructed values relate to the partonic values, correlation plots of reconstructed value versus generated value were made. Ideally, all the points should lie on the diagonal and would have $(value)_{rec} = (value)_{gen}$.

Figures 6.31(a)-(d) show the correlation plots in E, η, ϕ and p_T respectively for the hard scattered partons that were reconstructed as jets. The low cut-off observed in the reconstructed E

and p_T distributions is expected as the jets were required to have at least 5 GeV of transverse energy. It was concluded that the jet reconstruction was functioning well and that the reconstructed jet parameters related back well to the parameters of the original partons.

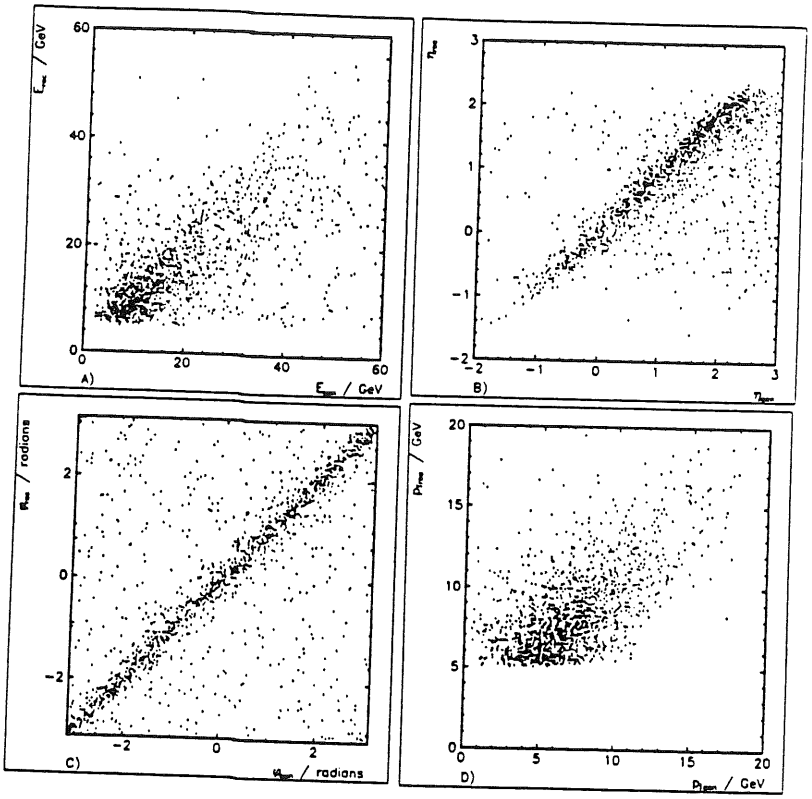

Figure 6.31: Reconstructed parameters versus generated parameters for jets in GRV Monte Carlo: a) E, b) η, c) ϕ, d) p_T.

Figures 6.32(a)-(d) show the correlation plots in E, η, ϕ and p_T respectively for the photon remnant parton and the photon remnant reconstructed by the D/M algorithm; figures 6.33(a)-(d) for the new algorithm. It was observed that the reconstructed energy was usually significantly lower than the generated energy. This observation supports the hypothesis that the shortfall in the x_γ+x_{rem} checksum is related to missing energy in the photon remnant reconstruction. No significant improvement in the energy reconstruction was observed in going to the new remnant algorithm. The values of p_T reconstructed by both algorithms was found to be un-correlated with the generated p_T.

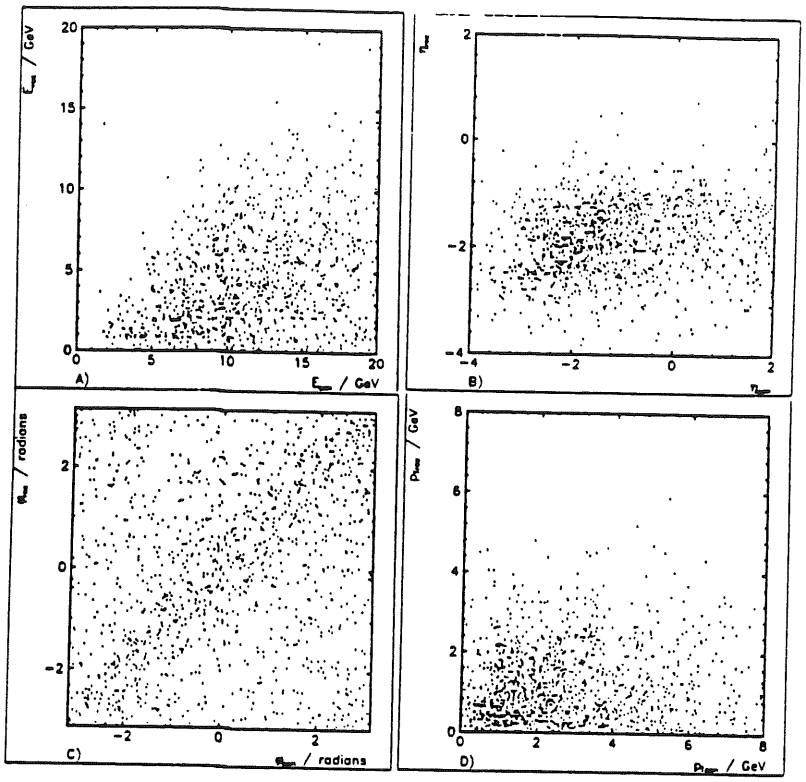

Figure 6.32: Reconstructed parameters versus generated parameters for photon remnant defined by D'Agostini/Monaldi algorithm in GRV Monte Carlo: a) E, b) η, c) ϕ, d) p_T.

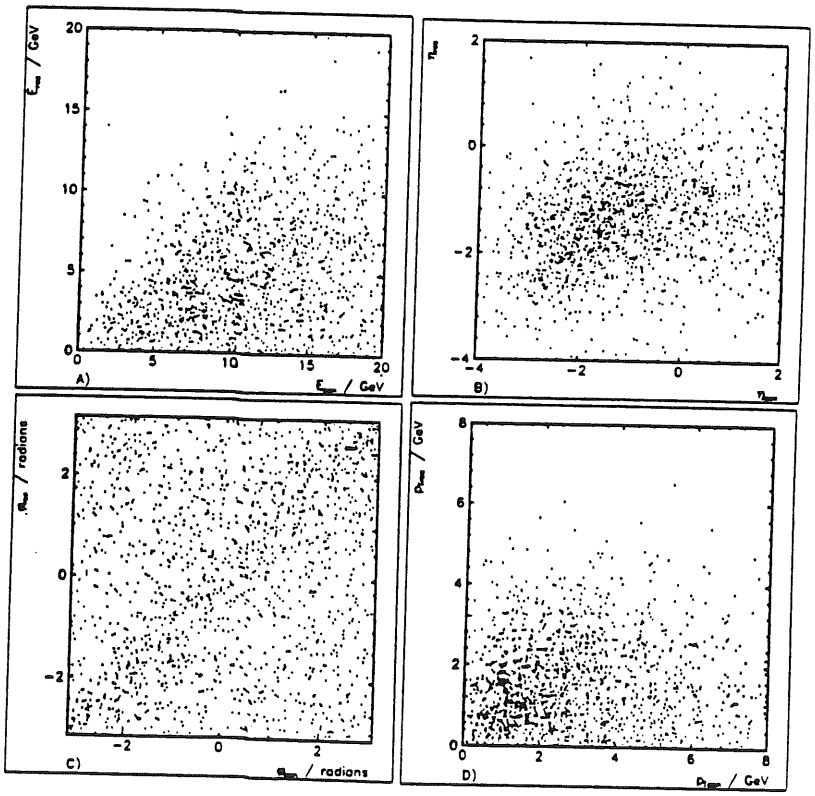

Figure 6.33: Reconstructed parameters versus generated parameters for photon remnant defined by new algorithm in GRV Monte Carlo: a) E, b) η, c) ϕ, d) p_T.

It was therefore concluded that the reconstructed photon remnant did not relate back well to the parton level and that no improvement was observed using the new algorithm. Three possible reasons for the poor performance were suggested. Firstly, the algorithm photon remnant signal might not be resolvable above the noise level in the calorimeters, a hypothesis not supported by the observation of peaks in the photon remnant profiles. Secondly, the poor hadronic energy measurement in the backwards direction mentioned in the x_γ+x_{rem} checksum section could be responsible. Lastly, the remnant could be picked up as a jet when it had E_T>5 GeV, as mentioned in the 'Photon Remnant Distributions' section. As the collimation of jets increases with increasing E_T, those remnants with E_T above threshold could also have been those which were sufficiently well collimated to be tagged by LUCELL. This would go some way to explaining why the observed p_T correlation was so bad: if the remnant had already been tagged as jet, the entity defined by the algorithms would not have been expected to relate to the parton level photon remnant.

In order to clarify which, if any, of the above suggestions was responsible for the poor performance of the remnant algorithm in relating back to the parton level, a set of 100 Monte Carlo events with total weight 84.21 were scanned with the reconstructed jet and remnant being displayed in addition to the partonic level information. The relatively small number of events gives an approximate error on the following percentages of ±10%.

In 92% of the weighted events, at least one jet corresponded to one of the hard scattered partons, the other 8% of events having no clear relationship between any of the partons and the reconstructed entities. In 49% of the events, a second jet corresponded well to the other parton. In 3% of the events, the second jet corresponded to the photon remnant parton and in 2% it was ambiguous whether the second jet or the remnant aligned better with the photon remnant parton. In the remaining 46% it was unclear to what the second jet corresponded. A third jet was found in 15% of events. For 3% of the events, the third jet clearly corresponded to the photon remnant parton and it was ambiguous whether the remnant or jet matched the remnant parton in 2% of events. In the remaining 10%, there was no visible relation between the third jet and a parton.

The remnant, defined in this instance using the new algorithm, corresponded to the

photon remnant parton in 52% of the events. In 3% of the events, the photon remnant algorithm had clearly picked up one of the hard scattered partons and in 4% it was ambiguous whether a jet or the remnant corresponded to the remnant parton. In the remaining 41% of the sample it was unclear to what the found photon remnant corresponded. The two jets and the photon remnant were all correctly identified in 44% of the events.

It was therefore concluded that the reconstruction was correctly assigning the partons in approximately 50% of the events. The photon remnant was tagged as a jet in about 10% of the events, and the remnant algorithm picked up a hard scattered parton rather than the remnant parton in only about 5% of the events.

It was therefore concluded that the detector and algorithm were both partially responsible for the poor correlation between the reconstructed and generated remnant, the result of poor hadronic calorimetry in the backwards direction and the inclusion of too many noisy cells. Future studies should examine how best to overcome these problems and how they influence the use of the photon remnant to discriminate between direct and resolved processes.

Example Event Pictures

Figure 6.34 shows a resolved photoproduction candidate as observed by H1. The jets found by LUCELL and the photon remnant found by the D/M algorithm are shown as red and blue lines respectively in figures 6.34(a) and (c). Figure 6.34(b) shows the energy deposition in the liquid argon and BEMC as a function of η and ϕ.

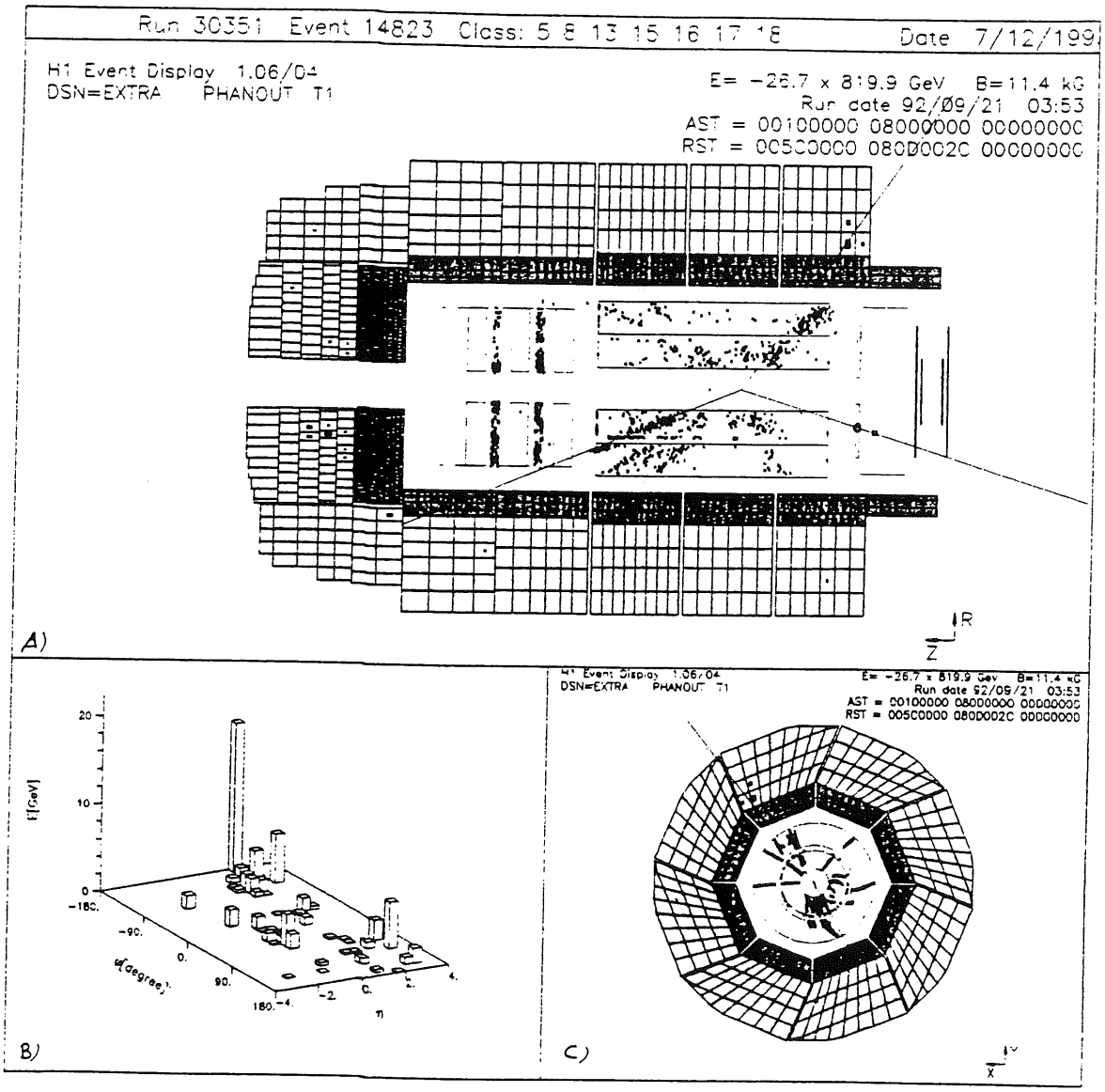

Figure 6.34: A resolved photoproduction candidate in the H1 detector a) *r-z* view, b) energy deposition vs. η and ϕ and c) *x-y* view. The two red lines indicate the found jet directions and the blue line the found photon remnant direction.

Figure 6.35 shows a direct photoproduction candidate as observed by H1. The jets found by LUCELL are shown as red in figures 6.35(a) and (c). No photon remnant was found for this event and there was little energy deposited in the backward region. Figure 6.35(b) shows the energy deposition in the liquid argon and BEMC as a function of η and ϕ. The large energy deposition in the forward part of the calorimeter comes from the proton remnant.

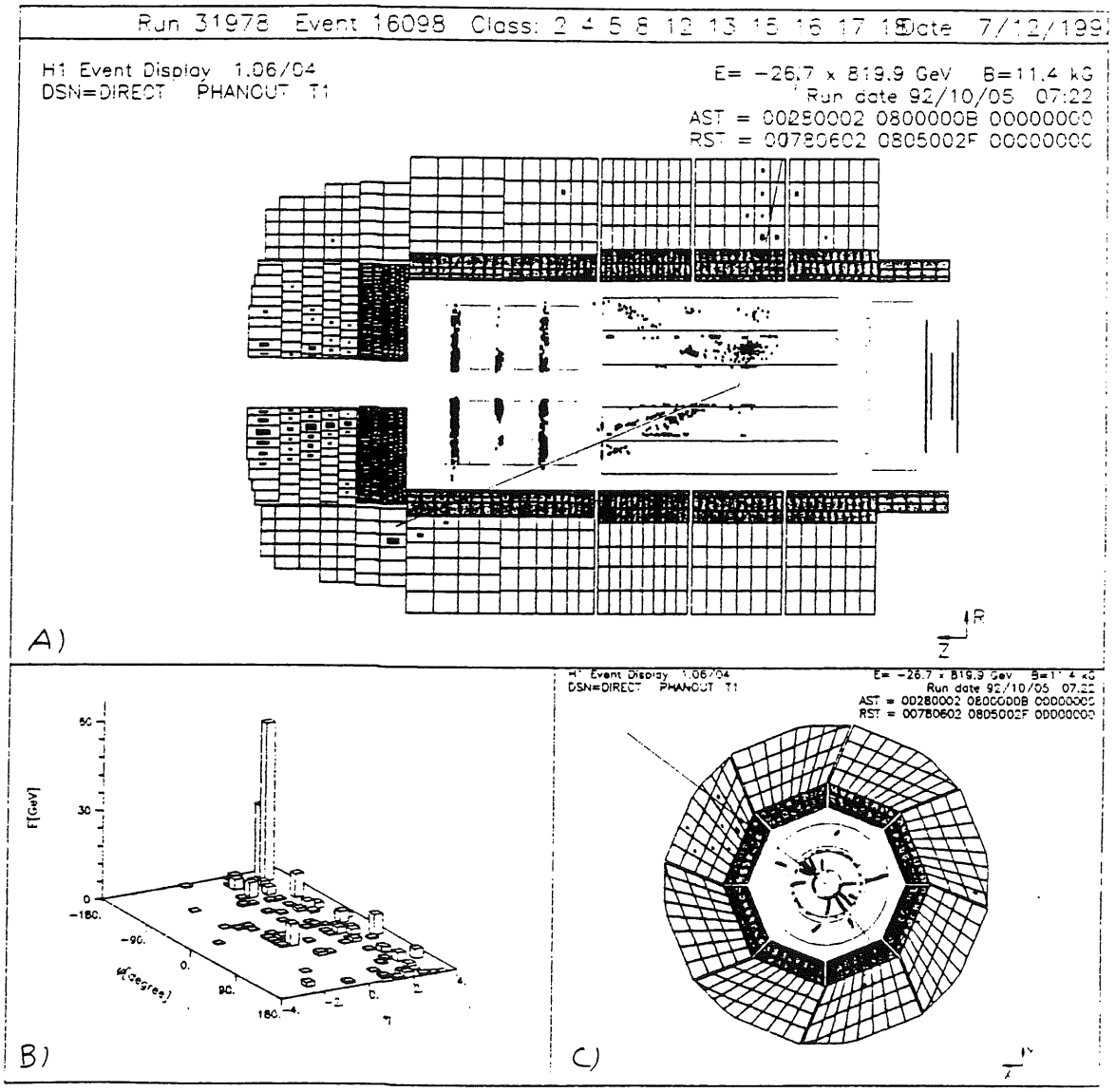

Figure 6.35: A direct photoproduction candidate in the H1 detector a) *r-z* view, b) energy deposition vs. η and ϕ and c) *x-y* view. The two red lines indicate the found jet directions.

Chapter 7: Conclusions and Future Work

Forward Muon Reconstruction

The forward muon reconstruction code, which is a part of the main H1REC program, has been described in detail. The performance of this code has been tested with a large number of simulated events with muon momenta in the range 5 - 250 GeV. The performance of the code on these single track events without noise gives the limit to what could be achieved in the real detector. The reconstruction performed well upon these tracks except that a systematic shift in the value of the reconstructed momentum was observed. This shift was as high as 10% for low values of momentum. The shift may be due to the approximate nature of the extrapolation used.

The momentum resolution achieved on this Monte Carlo data has been determined as $22.3\pm0.4\% + (0.057\pm0.005\%/\text{GeV})p$ without the phi chambers and $23.4\%\pm0.3\% + (0.049\%\pm0.004\%/\text{GeV})p$ with the phi chambers. The efficiency of track reconstruction was found to be 89%±1% over a wide range of momenta. The efficiency of reconstruction was found not to depend upon the position of the track within an octant and was not affected by the addition of the phi chambers.

The track θ angle was reconstructed with a resolution of 1.6×10^{-3} radians without the phi chambers and 1.1×10^{-3} radians with the phi chambers. The track angle ϕ was reconstructed with a resolution of 0.27 radians without the phi chambers and 2.7×10^{-3} radians with the phi chambers. The position of the track entry point was reconstructed with a resolution of 1 cm without the phi chambers and 0.17 cm with the phi chambers. The systematic variation of these quantities across an octant was understood by considering the relative mixture of drift and charge division co-ordinates used in the measurement.

It may therefore be concluded that the presence of the phi chambers improves the measurement of the ϕ angle, in agreement with expectation. With only the theta chambers installed, the precise drift measurement is only made in one direction. With the addition of the phi chambers, a precise determination is made in two perpendicular directions, resulting in a substantial improvement in the resolution of the track starting point in space.

The presence of the phi chambers has little effect on the momentum measurement. However, the Monte Carlo tracks used in this study were all radial and for this case the improvement was expected to be minimal. In the real data, where any muon coming from the centre of H1 will have passed through the instrumented iron, multiple scattering will have deflected the track from being exactly radial. In these circumstances, the presence of the phi chambers is expected to improve the momentum measurement. Further studies should quantify how the performance of the reconstruction varies as the tracks are deviated from radial.

In addition to making measurements of the five track parameters (p, θ, ϕ, x, y), the reconstruction code must supply an estimate of the errors on these quantities. Residual plots were used to show that the error analysis in the reconstruction code produced error estimates consistent with the observed spread in the reconstructed values.

Although the code has been shown to work well on Monte Carlo, there are still some studies that must be refined before a similar performance can be achieved on real data. Firstly, the detector must be aligned so that the positions of all the octants are well known. This will be done with a combination of beam halo muon tracks and physical survey of the detector. Secondly, the drift velocity and t_{zero} corrections must be determined, using beam halo tracks in the full detector and using cosmic ray test systems. Thirdly, studies must be made concerning how the drift velocity varies across a single drift cell and an isochrone map of the cell must be produced. This can be done using a special transparent test cell and an Ultraviolet laser, used to produce ionisation in the cell. Work is currently in progress in Manchester with such a set-up.

The information from all these studies must then be incorporated correctly into the reconstruction code and stringent performance tests must be made to ensure that the differences between the real detector and the simulation are correctly treated. Preliminary studies of all these problems have already been performed and further studies are currently in progress. It is hoped that the real detector will soon be delivering results in line with the design specifications.

Photoproduction At HERA

In Autumn 1992, H1 took 23.8±1.5 nb^{-1} of electron-proton data compared with a design goal of 200 pb^{-1} per year of running. The analysis possible on such a small data sample was necessarily limited. However, the total cross section for photoproduction at HERA was measured to be 159±7±20 μb in a previous publication [75], suggesting that meaningful studies could be made in this area. A decision was therefore made to trigger on photoproduction events where the scattered electron was detected in the electron tagger. Insisting that the electron be tagged allowed the four-momentum of the photon to be reconstructed using the electron information only but limited the accessible kinematic range to $Q^2<0.01$ GeV^2 and $0.2< y <0.8$.

H1 therefore collected photoproduction events with the ETAG*t0 trigger. These events were then passed through a set of cuts to reduce the contribution from random hits in the electron tagger in coincidence with proton beam induced interactions in the H1 detector. The events so selected were compared with theoretical predictions using the PYTHIA Monte Carlo program and the H1SIM detector simulation program. The photon structure function parameterisation used was that of Gluck, Reya and Vogt. The events were also re-weighted with the LACIII structure function parameterisation to compare the predictions of the two. The Monte Carlo events were passed through the same cuts as the data sample.

After the imposition of these cuts, 4354 events remained in the data sample. A selection of proton pilot bunch events was used to tune the cuts and it was estimated that only 11±2 such background events remained in the data after cuts. The Monte Carlo predictions were 5957 events using the GRV structure function and 10915 events using the LACIII structure function. It was therefore concluded that a significant number of photoproduction events were observed at HERA even with the small integrated luminosity collected in 1992. The number of events collected was broadly in line with theoretical predictions. Distributions of the energy of the tagged electron, y calculated by the Jacquet-Blondel method and the z position of the reconstructed vertex were examined and reasonable agreement between the data and the Monte Carlo predictions was observed.

Photoproduction events fall into two classes, shown in figures 7.1(a) and 7.1(b). In

direct events, figure 7.1(a), the whole photon interacts with a parton from the proton, producing two jets and a proton remnant in the final state. In resolved events, figure 7.1(b), some parton from the photon interacts with a parton from the proton, producing two jets, a proton remnant and a photon remnant.

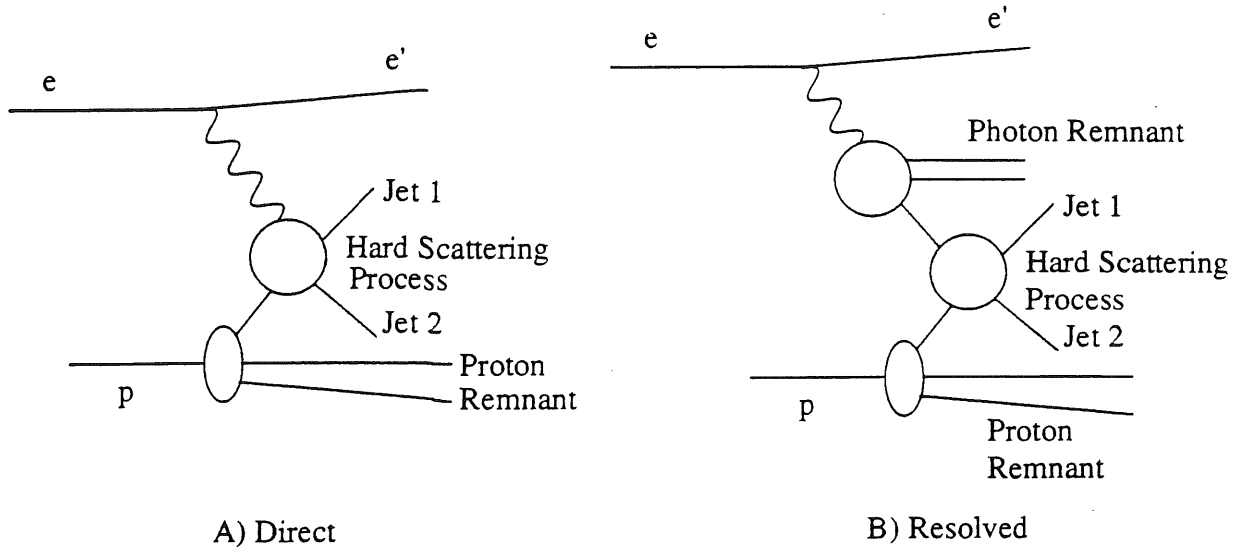

A) Direct B) Resolved

Figure 7.1: Photoproduction events at HERA. a) Direct, b) resolved.

The LUCELL jet finding algorithm was used in order to find jets in the events. The parameters used were an initiator transverse energy requirement of 0.2 GeV and a cone size of 1.0 unit in $\eta-\phi$ space. The cone was accepted as a jet if the transverse energy contained within it exceeded a threshold. A value of E_{Tmin}=5 GeV was chosen for this threshold. Normally, higher values are chosen (the H1 paper on jet rates in photoproduction used 7 GeV [64]) but with the small data sample available it was necessary to go down to 5 GeV in order to be able to tag two jet events. Scanning Monte Carlo events visually led to the conclusion that at least one reconstructed jet could clearly be related back to the parton in approximately 90% of events but that the second jet could only be related back clearly in half the events.

A total of 467 data events were left after requiring two jets, corresponding to 10.8% of the original sample. In the GRV Monte Carlo, only 277 events remained, corresponding to 4.7% of the original. When the Monte Carlo events were reweighted with the LACIII structure function, 728 events remained, corresponding to 6.7% of the original sample. It may therefore be

concluded that the number of events with two or more jets in the data was between the two Monte Carlo predictions. However, the fraction of events with at least two jets was found to be higher for the data than for either Monte Carlo prediction.

The distributions of these jets as a function of energy (E), pseudo-rapidity (η), phi (ϕ) and transverse momentum (p_T) were then examined. The data and Monte Carlo predictions were found to agree well in shape for E, ϕ and p_T. However, a discrepancy was found in the η distribution. In the forward region, $\eta>1$, significantly more jets were observed in the data than predicted by either Monte Carlo. A similar effect was observed using tracks reconstructed by the H1 central tracking detector.

The jet profiles, plots of transverse energy flow relative to the axis of the found jets, were then examined. It was observed that the jet energy was well contained within a cone of radius 1.0 in $\eta-\phi$ space. It was found that the observed shape agreed with the Monte Carlo prediction in ϕ, but that there was more energy in the forward jet tail in the data than predicted by the Monte Carlo. This effect has also been reported in [64].

It is currently suggested that the data and Monte Carlo predictions match well except in the forward region. It is therefore also suggested that there is some physical effect spraying particle into the forward region. This difference in energy flow is thought to account for the higher fraction of data events having two or more jets and for the discrepancies observed in the jet and charged track distributions. No firm conclusions could be drawn regarding the possibility of distinguishing between different parameterisations of the photon structure function because of this forward energy flow difference. Studies are in progress at DESY to understand and reproduce the forward energy flow using both the 1992 data and the new 1993 data, in which the forward tracker is fully operational and well reconstructed, which should greatly aid the investigation of this problem.

The value of x_γ, the fraction of the photon four-momentum taken by the interacting parton, was calculated using the reconstructed jet information. As a greater fraction jets were found in the forward region in the data, it was expected that a greater fraction of events would have a low value of x_γ than predicted by the Monte Carlo. It was observed that the data had a

much larger fraction of events in the region x_γ<0.3 but that above this the data and GRV Monte Carlo distributions matched well. The LACIII re-weighted Monte Carlo predicted significantly more events than were observed.

The Photon Remnant

As discussed above, two classes of photoproduction event were expected at HERA: direct and resolved. A previous Monte Carlo study by D'Agostini and Monaldi [74] had indicated that a separation between direct and resolved events may be performed by looking for the photon remnant, expected to be present in resolved events only as shown in figure 7.1. The algorithm used in their study examined the energy contained within a cone one unit in η behind the backwards-most jet. If this energy exceeded 3 GeV, the event was labelled as resolved.

In addition to searching for the presence of a photon remnant to distinguish between direct and resolved events, the properties of the photon remnant itself are of interest. In order to examine these properties, an algorithm was used to sum those particle believed to have originated from the photon remnant parton. Two such algorithms were presented, the first based on the cone used by D'Agostini and Monaldi, the second collecting all energy deposited behind the forward-most jet and at least 1.5 units away from the axis of any jet as well as the cone behind the backwards-most jet.

It was observed that 79±2% of events with two or more jets in the data had a photon remnant using the D'Agostini/Monaldi based algorithm. With the new algorithm this rose to 96±2%, but the new algorithm was thought to be very sensitive to the presence of noise or particles from jet pedestals. To reduce this sensitivity, a requirement was made that the found photon remnant should have an energy of at least 3 GeV. Imposing this requirement, 55±2% of data events remained when using the original algorithm, rising to 69±2% with the new algorithm.

The discriminating power of this requirement was examined using the Monte Carlo predictions. It was found that between 38% and 47% of the resolved events had a photon remnant defined by the original algorithm with at least 3 GeV whereas only 6% of direct events

had such a remnant. For the new algorithm, between 56% and 62% of the resolved events and 44% of the direct events had a remnant with an energy of at least 3 GeV.

It was therefore concluded that the D'Agostini/Monaldi algorithm was capable of good discrimination between direct and resolved events and that the new algorithm did not perform as well. The observation that over 50% of the data events had a remnant with a energy of at least 3 GeV in the D'Agostini/Monaldi cone led to the conclusion that the data events were mostly resolved rather than direct, in line with theoretical expectations.

The distributions of the photon remnants in E, η, ϕ and p_T were then examined with the remnant defined by both the algorithms described above. As the remnant was found to be predominantly in the backwards region, $\eta<0.0$, the difference in forward energy flow between data and Monte Carlo was not expected to cause problems. The distributions were found to be in agreement within errors. The E, η, ϕ and p_T distributions of the charged tracks within the remnant were examined and good agreement was found between data and Monte Carlo, confirming that the description of the photon remnant in PYTHIA is reasonable.

The transverse energy flows about the found remnant axis in η and ϕ were examined using both calorimeter cells and tracks. These energy flow profiles were found to be peaked around the remnant axis, confirming that the found photon remnant corresponded to a real concentration of energy. The shape of the observed profiles agreed with the Monte Carlo predictions within errors. It was observed that the peaks in the remnant energy flow were broader than 1.0 unit in $\eta-\phi$, suggesting that the remnant jets were not as well collimated as the hard scattered parton jets.

A measurement was made of x_{rem}, the fraction of the photon's four-momentum taken by the photon remnant and the value of the checksum $x_\gamma+x_{rem}$ was plotted. Contrary to expectation, the peak of this distribution lay significantly below 1.0 for data and Monte Carlo. Comparisons between the generated and reconstructed parameters of the partons in the Monte Carlo sample indicated that the hard scattered parton jets were being well reconstructed but that the remnant reconstruction was relatively poor. It was therefore concluded that the remnant reconstruction algorithms were missing some energy (the original algorithm more than the new) and that this

was mainly responsible for the shortfall in the x_γ+x_{rem} checksum.

Three hypotheses were advanced to account for the poor correlation between the reconstructed and generated parameters of the photon remnant. This first hypothesis was that the remnant, where present, had already been labelled as a jet and the remnant formed by the algorithms was therefore the sum of noise in the event. The peaks in the energy flow profiles and a visual scan of the Monte Carlo events did not support this hypothesis. Second, it was thought that noise in the calorimeters might have been swamping the photon remnant signal, giving a poor relation back to the parton level. The observation that the reconstructed energy was too low rather than too high in the Monte Carlo did not support this explanation. It was therefore suggested that the poor hadronic calorimetry in the backward region of H1 might have limited how well the remnant could be reconstructed. Further studies should therefore include the instrumented iron behind the BEMC as this may improve matters. An upgrade to the backward calorimetry of H1 is also planned.

Future studies should also be carried out using different algorithms to gather the photon remnant. The broad collection algorithms described in this report have been shown to be capable of identifying that a remnant is present but to be poor at reconstructing the parameters of this remnant. It is therefore suggested that studies be carried out using event decomposition techniques such as the JADE algorithm [76] and DECO [77] where all particles in the detector are assigned to jets by minimisation of some quantity such as the invariant mass between the jets. Such algorithms are useful as they use all particles in the event and also use make good use of both the direction and energy information reconstructed by the detector.

It is further suggested on the basis of the observed remnant energy flow profiles that a cone algorithm of the LUCELL type may be capable of identifying and reconstructing the photon remnant. Future studies could investigate how best to modify the LUCELL algorithm for this purpose in order to provide a complimentary alternative to the event decomposition method.

Finally, it is suggested that more detailed studies should be made on the 1993 (and future) data as this will allow a much greater understanding of photoproduction at HERA than has been possible with the initial 1992 data.

Appendix A: Reconstruction Of x_γ

The basic resolved photoproduction reaction is shown in figure A.1. Given that the incoming photon four-momentum is **q**, the incoming momentum of the parton from the photon is x_γ**q** (neglecting any primordial p_T of the parton). Similarly, if the proton has incoming four-momentum **p**, the parton from the proton has x_p**p**. The outgoing scattered partons have four-momenta **j** and **k**, the photon remnant **r** and the proton remnant **f**.

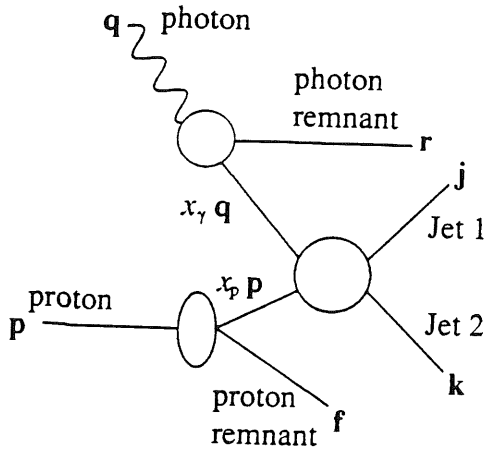

Figure A.1: Kinematics of a resolved photoproduction interaction.

Four-momentum conservation requires that

$$x_\gamma\ \mathbf{q} + x_p\ \mathbf{p} = \mathbf{j} + \mathbf{k}$$

If the assumption is made that the initial p_T is zero, the final p_T must also be zero. Two equations are then obtained, one for energy conservation

$$x_\gamma E_\gamma + x_p E_p = E_j + E_k$$

and one for conservation of the z-component of momentum

$$x_\gamma\, p_{z\gamma} + x_p\, p_{zp} = p_{zj} + p_{zk}$$

where E_i and p_{zi} are the energy and z-component of momentum of four-vector i. Substituting for x_p gives

$$x_\gamma E_\gamma + \frac{E_p}{p_{zp}}\left(p_{zj} + p_{zk} - x_\gamma\, p_{z\gamma}\right) = E_j + E_k$$

If the incoming particles are massless and have negligible p_T, $E_p = p_{zp}$ and $E_\gamma = -p_{z\gamma}$, which gives

$$x_\gamma = \frac{\left(E_j - p_{zj}\right) + \left(E_k - p_{zk}\right)}{2E_\gamma}$$

The transverse energy, E_T, of a massless particle may be re-written as

$$E_T = \sqrt{E^2 - p_z^2} = \sqrt{(E - p_z)(E + p_z)}$$

and by exponentiating rapidity, j, the following expression is obtained

$$\exp(-j) = \exp\left(-\frac{1}{2}\ln\left(\frac{E + p_z}{E - p_z}\right)\right) = \sqrt{\frac{E - p_z}{E + p_z}}$$

Hence,

$$E_T \exp(-j) = \sqrt{(E - p_z)(E + p_z)}\sqrt{\frac{E - p_z}{E + p_z}} = E - p_z$$

Substituting pseudo-rapidity, η, as an approximation to rapidity,

$$x_\gamma = \frac{E_{Tj}\exp(-\eta_j) + E_{Tk}\exp(-\eta_k)}{2E_\gamma}$$

An expression for x_γ may also be obtained by using the photon remnant four-vector **r**. Since

$$x_\gamma \mathbf{q} = \mathbf{q} - \mathbf{r}$$

multiplying throughout by the proton four-momentum, **p**, and re-arranging gives

$$x_\gamma = 1 - \frac{\mathbf{r} \cdot \mathbf{p}}{\mathbf{q} \cdot \mathbf{p}}$$

The fraction of the photon's four-momentum taken by the remnant, x_{rem} is therefore given by

$$x_{rem} = \frac{\mathbf{r} \cdot \mathbf{p}}{\mathbf{q} \cdot \mathbf{p}}$$

as the checksum

$$x_\gamma + x_{rem} = 1$$

must be true in order to conserve four-momentum.

References

[1] F. Abe et al. (CDF Collaboration) Phys. Rev. **D45** (1992) 3921.

[2] Higgs, P. W., Phys. Lett **12** (1964) 132 and Phys. Rev. **145** (1966) 1156.

[3] M. Breidenbach et al., Phys. Rev. Lett. **23** (1969) 935.

[4] Bjorken, J. D., Phys. Rev. **163** (1967) 1767.

[5] F. Halzen, A. Martin, *Quarks and Leptons*. John Wiley & Sons (1984).

[6] G. Altarelli and G. Parisi, Nucl. Phys. **B26** (1977) 298.

[7] M. Gluck, E. Reya and A. Vogt, Z. Phys **C53** (1992) 127.

[8] Zeus Collaboration, *Zeus Technical Proposal* (1986).

[9] a review may be found in T. Sloan, Proc. EPS Conf. on high-energy physics (Uppsala) ed. O. Botner (1987).

[10] M. Bourquin et al., Z. Phys **C21** (1983) 27.

[11] J. Ashman et al. (E.M.C.), Phys. Lett. **B206** (1988) 364.

[12] J. Ellis and M. Karliner, Phys. Lett. **B213** (1988) 73.

[13] C.F. Weizsacker, Z. Phys. **88** (1934) 612.
E.J. Williams, Phys. Rev. **45** (1934) 729.

[14] A.I. Lebedev, Proceedings of the HERA workshop (1992) Vol 1, 613.

[15] J. R. Smith, H1 note H1-12/92-259 (1992).

[16] I. Abt, J. R. Smith, H1 note H1-10/92-249 (1992).

[17] J. Storrow, J. Phys. **G19** (1993) 1641.

[18] R.J. Apsimon et al. (OMEGA Photon collaboration), Z.. Phys. C. **46** (1990) 35.

[19] J.J. Sakurai, Ann. Phys. **11** (1960) 1.

[20] J.J. Sakurai and D. Schildknecht, Phys. Lett. **B40** (1972) 121.

[21] M. Greco, Nucl. Phys. **B63** (1973) 398.

[22] D. W. Duke and J. F. Owens, Phys. Rev. **D26** (1982) 1600 erratum Phys. Rev. **D28** (1983) 1227.
P. Aurenche et al., Proceedings of the HERA workshop (1987) Vol 2, 561.

[23] Regge, T., Nuovo Cim. **14** (1959) 951.

[24] A. Donnachie, P. V. Landshoff, CERN-TH 635/91 (1992).

[25] H. Abramowicz, K. Charchula and A. Levy, Phys. Lett. **269** (1991) 458.

[26] L.E. Gordon and J. K. Storrow, Manchester preprint M/C. TH.91/29.

[27] M. Gluck, E. Reya and A. Vogt, Phys. Lett. **B222** (1989) 149.
M. Gluck, E. Reya and A. Vogt, Phys. Rev. **D45** (1992) 3986.

[28] M. Drees and K. Grassie, Z. Phys. C. **28** (1985) 451.

[29] G.A. Schuler and T. Sjostrand, CERN preprint TH.6796/93 (1993).

[30] H1 Collaboration, *The H1 detector at HERA* (1993), Internal report, to be submitted in part to Nucl. Inst. Meth.

[31] H1 Collaboration, *Technical Proposal for the H1 detector*. (1986).

[32] H. Drum et al. (JADE collaboration), Nucl. Inst. Meth. **A279** (1989) 217.

[33] R. Fernow, *Introduction to experimental particle physics*, Cambridge University Press (1986).

[34] I.E.E.E. Standard 1014, *The VMEbus specification.*

[35] G. Bernardi et al., H1 collaboration, *H1REC manual*, internal H1 report.

[36] D. Sankey et al., H1 collaboration, *H1QT manual*, internal H1 report.

[37] M. Brun et al., *CMZ - a source code management system.* Proc. Int. Conf. on Computing in High Energy Physics (1989).

[38] V. Blobel, *BOS and related packages*, Proc 14th Workshop of the INFN Eloisatron Project.

[39] Z. Feng et al., *H1 DDL rules*, internal H1 report.

[40] U. Berthon et al., *A data management tool package for H1*, H1 software note 8, DESY Hamburg (1990), unpublished.

[41] V. Blobel, *The F-package for input-output*, Proc. Int. Conf. on Computing in High Energy Physics (1992).

[42] L. Crigee et al., H1 collaboration, *The H1 database*, internal H1 report.

[43] S. Egli et al., H1 collaboration, *H1SIM manual*, internal H1 report.

[44] R. Brun et al., *GEANT long writeup*, CERN program library, W5103 (1989).

[45] S. Egli et al., H1 collaboration, *The H1FAST parameterised simulation program*, internal H1 report.

[46] M. Kuhlen, *The fast H1 detector Monte Carlo*, Proc. 26th Int. Conf on High Energy Physics (1992).

[47] I.S.O. standard 8805: *GKS graphics.*

[48] S. Levonian et al., H1 collaboration, *The H1 event display*, internal H1 report.

[49] M. Erdmann et al., H1 collaboration, *H1PHAN manual*, internal H1 report.

[50] J. P. Sutton, *The H1 Forward Muon Spectrometer at the HERA collider*, Ph.D. thesis, University of Manchester (1993).

[51] A. Mehta, *Investigation of the Drift Velocity of the Forward Muon Drift Chambers of the H1 detector*. Internal report, University of Manchester (1992).

[52] L. West and H. T. Phillips, *MTREC technical writeup*. internal H1 report (1993).

[53] J. Foster, *QTFMU, the forward muon Qt code*. Internal report, University of Manchester.

[54] C. Hilton, *Investigations concerning the Forward Muon Drift chambers of the H1 detector*. Internal report, University of Manchester (1991).

[55] S. Egli, *BOS modules in H1 software*. H1 software note 12 (1990), DESY, Hamburg.

[56] W. Lohmann et al., *Energy Loss of Muons in the energy range 1-10,000 GeV*, CERN 85-03 (1985).

[57] M. Aguilar-Benitez et al. (Particle Data Group), *Review of Particle Properties*, Phys. Rev. **D45** (1992) Part 2.

[58] W. T. Scott, Rev. Mod. Phys. **35** (1963) 231.

[59] R. J. Barlow, *Statistics*. John Wiley and Sons (1989).

[60] H. U. Bengtsson and T. Sjostrand, Comp. Phys. Comm. **46** (1987) 43.

[61] H. Plothow-Besch, PDFLIB User's Manual, CERN Program Library W5051 (1990).

[62] A. Martin et al., Durham Theory Preprint DTP/92-16 (1992).

[63] M. Erdmann, private communication.

[64] I. Abt et al., H1 collaboration, Phys. Lett. **B314** (1993) 436.

[65] F. Jaquet and A. Blondel, *An ep facility for Europe*, Proceedings, Hamburg (1979) ed. U. Amaldi.

[66] LUCELL is described in the JETSET manual, T. Sjostrand and M. Bengtsson, Comp. Phys. Comm. **43** (1987) 367.

[67] G. Knies, private communication.

[68] *Minutes of the H1 photoproduction working group* 9-Jul-1993 (1993), internal report.

[69] G. Knies, *Soft and Hard Photoproduction News from H1 at HERA*. H1 note 303, H1-07/93-303 (1993), internal report.

[70] *Minutes of the H1 photoproduction working group* 11-Jun-1993 (1993), internal report.

[71] T. Sjostrand, Comp. Phys. Comm. **39** (1986) 347.

[72] G. Marchesini et al., Comp. Phys. Comm. **67**(1992) 465.

[73] L. Lonnblad, *Ariadne 4.0*, DESY report 92-046 (1992), to be submitted to Comp. Phys. Comm.

[74] G. D'Agostini and D. Monaldi, Physics at HERA Vol. 1 (1992) 527 ed. W Buchmuller and G. Ingelman.

[75] T. Ahmed et al., H1 collaboration, Phys. Lett. **B299** (1993) 374.

[76] W. Bartel et al., JADE collaboration, Z. Phys. **C33** (1986) 23.
S. Bethke et al., JADE collaboration, Phys. Lett. **B213** (1988) 235.

[77] DECO is described in M. Erdmann et al., H1 collaboration, *H1PHAN manual*, internal H1 report.